

AD-A247 060



C

92
D

C

AEOSR-TR- 92 0084

2

**Final Technical Report to:
The Air Force Office of Scientific Research**

for the Project:

**"Intense Electron Beam Cyclotron Masers with
Microsecond Pulselengths"**

Grant No. AFOSR-88-0276

Submitted by:

**Ronald M. Gilgenbach
Professor and Director
Intense Energy Beam Interaction Laboratory
Nuclear Engineering Department
University of Michigan
Ann Arbor, MI 48109**



December 1991



92 3 03 040

92-05567



REPORT DOCUMENTATION PAGE

OMB No. 0704-0188

Public reporting burden for this collection of information is estimated to average 1 hour per response, including the time for reviewing instructions, searching existing data sources, gathering and maintaining the data needed, and completing and reviewing the collection of information. Send comments regarding this burden estimate or any other aspect of this collection of information, including suggestions for reducing this burden, to Washington Headquarters Services, Directorate for Information Operations and Reports, 1215 Jefferson Davis Highway, Suite 1204, Arlington, VA 22202-4302, and to the Office of Management and Budget, Paperwork Reduction Project (0704-0188), Washington, DC 20503.

1. AGENCY USE ONLY (Leave blank)	2. REPORT DATE 12-20-91	3. REPORT TYPE AND DATES COVERED Final: 8-1-88 to 11-30-91	
4. TITLE AND SUBTITLE Intense Electron Beam Cyclotron Masers with Microsecond Pulselengths		5. FUNDING NUMBERS AFOSR-88-0276	
6. AUTHOR(S) R. M. Gilgenbach			
7. PERFORMING ORGANIZATION NAME(S) AND ADDRESS(ES) Nuclear Engineering Department University of Michigan Ann Arbor, MI 48109-2104		8. PERFORMING ORGANIZATION REPORT NUMBER AFOSR-Final-12/91	
9. SPONSORING/MONITORING AGENCY NAME(S) AND ADDRESS(ES) Air Force Office of Scientific Research Bolling Air Force Base, Washington, DC 20332-6448 <i>Barner</i>		10. SPONSORING/MONITORING AGENCY REPORT NUMBER <i>2301/AS</i>	
11. SUPPLEMENTARY NOTES <i>NE</i>			
12a. DISTRIBUTION/AVAILABILITY STATEMENT Approved for public release; distribution is unlimited.		12b. DISTRIBUTION CODE	
13. ABSTRACT (Maximum 200 words) Results are reported for a three year research program with the goal of generating high power microwaves over long-pulselengths. Three types of cyclotron maser devices were developed and utilized in experiments on the Michigan Electron Long Beam Accelerator, (MELBA) at electron beam parameters of 0.6-0.9 MV, 0.05-2 kA, and 0.5-5 μ s: 1) The gyrotron backward-wave-oscillator, (gyro-BWO) produced the optimal combination of high power (1-8 MW) and long pulse (0.5-1.2 μ s) microwave generation. Due to these promising results, this gyro-BWO device was investigated most intensively during the final phase of this research program. 2) Bragg resonator cyclotron resonance masers were investigated with high quality, low current electron beams for high frequency microwave generation. These devices generated hundreds of kW for hundreds of ns, but it was found that microwaves originated from cyclotron harmonic generation on absolute instabilities. 3) Open cavity resonators of unslotted and slotted types generated microwave spikes (20-40 ns) in the X-band with peak power up to 15-25 MW. High peak microwave power (MW) was also generated in the K-band, most likely from the second cyclotron harmonic.			
14. SUBJECT TERMS high power microwaves, electron beams		15. NUMBER OF PAGES 90	
		16. PRICE CODE	
17. SECURITY CLASSIFICATION OF REPORT UNCLASSIFIED	18. SECURITY CLASSIFICATION OF THIS PAGE UNCLASSIFIED	19. SECURITY CLASSIFICATION OF ABSTRACT UNCLASSIFIED	20. LIMITATION OF ABSTRACT

Table of Contents

	<i>page</i>
1.0 Executive Summary.....	3
2.0 Experimental Progress During Grant Period.....	4
2.1 Introduction.....	4
2.2 Gyrotron backward-wave-oscillator Experiments.....	5
2.3 Bragg Resonator Cyclotron Maser Experiments.....	9
2.4 MELBA Masers A1 and A2.....	15
2.5 Electron Beam Generation and Diagnostics.....	19
3.0 References.....	20
Appendices:	
Appendix A) Titles and Abstracts of Ph.D. Dissertations Resulting from this Research	21
Appendix B) List of Publications Supported by This Grant.....	24
Appendix C) Copies of Publications Supported by This Grant.....	C1



Accession For	
NTIS GRA&I	<input checked="" type="checkbox"/>
DTIC TAB	<input type="checkbox"/>
Unannounced	<input type="checkbox"/>
Justification	
By _____	
Distribution/	
Availability Codes	
Dist	Avail and/or Special
A-1	

1.0 Executive Summary

Results are reported for a three year research program with the goal of generating high power microwaves over long-pulse lengths. Three types of cyclotron maser devices were developed and utilized in experiments on the Michigan Electron Long Beam Accelerator, (MELBA) at electron beam parameters of 0.6-0.9 MV, 0.05-2 kA, and 0.5-5 μ s:

- 1) The gyrotron backward-wave-oscillator, (gyro-BWO) produced the optimal combination of high power (1-8 MW) and long pulse (0.5-1.2 μ s) microwave generation. Due to these promising results, this gyro-BWO device was investigated most intensively during the final phase of this research program.
- 2) Bragg resonator cyclotron resonance masers were investigated with high quality, low current electron beams for high frequency microwave generation. These devices generated hundreds of kW for hundreds of ns, but it was found that microwaves originated from cyclotron harmonic generation on absolute instabilities.
- 3) Open cavity resonators of unslotted and slotted types generated microwave spikes (20-40 ns) in the X-band with peak power up to 15-25 MW. High peak microwave power (MW) was also generated in the K-band, most likely from the second cyclotron harmonic.

Electron beam diagnostics were also developed in order to analyze the operation of these cyclotron masers. A new diagnostic of electron beam $\alpha = v_{\perp}/v_{\parallel}$ was developed, based on Cerenkov emission and radiation darkening of a glass plate.

Two doctoral dissertations resulted from this research, by T.A. Spencer and J.J. Choi. This research also resulted in several papers for publication in refereed journals and numerous papers presented at conferences including: International Conference on Infrared and Millimeter Waves, IEEE Conference on Plasma Science, SPIE, and APS Division of Plasma Physics.

2.0 Experimental Progress During the Grant Period

2.1 Introduction

During the period of this grant three types of electron cyclotron maser devices were investigated as sources of high power, long-pulse microwaves utilizing MELBA (Michigan Electron Long Beam Accelerator):

- 1) The most recent MELBA experiments performed during the last year concerned the gyrotron-backward-wave-oscillator (Gyro-BWO) with a smooth tube and microwave output on the diode end. These experiments were the most promising in terms of both high power (1-8 MW) and long-pulse (0.5-1.2 μ s) microwave generation.
 - 2) Earlier experiments on MELBA Masers B1 and B2 utilized a high quality electron beam with low-Q (B1) and high-Q (B2) Bragg resonator cavities. The most extensive experiments were performed with the high Q-Bragg resonator, B-2. Microwave emission was compared for configurations with-versus-without Bragg resonators.
 - 3) The experiments during the first year on MELBA Masers A1 and A2 utilized a high current electron beam with unslotted (A1) versus slotted (A2) smooth tube cavities without Bragg resonators.
- The next sections describe the experiments performed on each of the three devices.

These experiments resulted in two doctoral dissertations:

- 1) T. A. Spencer, "High Current, Long-Pulse Gyrotron Backward Wave Oscillator Experiments", and
- 2) J. J. Choi, "Bragg Resonator Cyclotron Maser Experiments Driven by a Microsecond Intense Electron Beam Accelerator".

Both of these Ph. D. graduates are performing microwave research at DoD labs, Spencer is on IPA at Phillips Lab and Choi is a contractor at Naval Research Lab.

Abstracts for these dissertations are given in Appendix A.

2.2 Gyrotron-Backward-Wave-Oscillator Experiments

The most successful combination of microwave power and pulselength was generated by the gyrotron-backward-wave-oscillator shown in Figure 1. Because of the promising nature of the gyro-BWO results, we focused the latter phase of the research on this device. We discovered that the gyrotron backward wave oscillator has a number of advantages for long-pulse, high power microwave generation:

- 1) Insensitivity to e-beam velocity spread (this is important in intense e-beam devices which utilize cold cathodes),
- 2) Large voltage bandwidth for maintenance of resonance,
- 3) High growth rate which overwhelms competing mechanisms.

Figure 2 shows a 1.2 μ s microwave pulse, our longest intense beam microwave pulselength.¹ The tube power level in these initial experiments was in the range of 1-8 MW, and is as-yet unoptimized.

The experimental description is as follows. A velvet cathode was placed in a region of low magnetic field (~500-800 G) generated by large pancake coils. Two different anodes were utilized for this research. The first generated an annular beam by an a ring of small holes drilled in a graphite anode plate. This limited the e-beam current to several hundred amps, but gave a well-defined value of $\alpha = v_{\perp}/v_{\parallel}$ (~0.65). A second anode had a large hole to generate a solid beam with higher current 1-2 kA, but a very large spread in α (0.05-0.7). Most experiments were performed with a planar velvet cathode. However, a new configuration utilizing a profiled velvet cathode on the end of a hemispherically shaped cathode stalk gave the longest pulselength e-beams and microwaves. It is believed that the lack of edge enhancement of this cathode yielded the improved pulselength. A solenoid wound directly on the beam tube gave a magnetic field which could be adjusted independently of the diode field from 4.8 to 6.6. kGauss in the smooth tube interaction region.

Extensive frequency measurements have been made to verify that the emission was due to the gyrotron-backward-wave-oscillator mechanism as shown in Figure 3. The emission frequency in the gyro-BWO is Doppler downshifted to the range 4.5 to 6 GHz, as shown in the dispersion relation given in Figure 4. Note that the measured emission frequency is always less than the relativistic cyclotron frequency and increases with the magnetic field, proving that the interaction mechanism is the gyro-BWO.

A comparative study was made of the microwave output power as a function of the electron beam current and e-beam profile (hollow versus solid). The results of this study are presented in Figure 5. It can be seen that the solid beam gave higher power because of the higher current, but the efficiency was roughly the same for the two electron beam profiles.

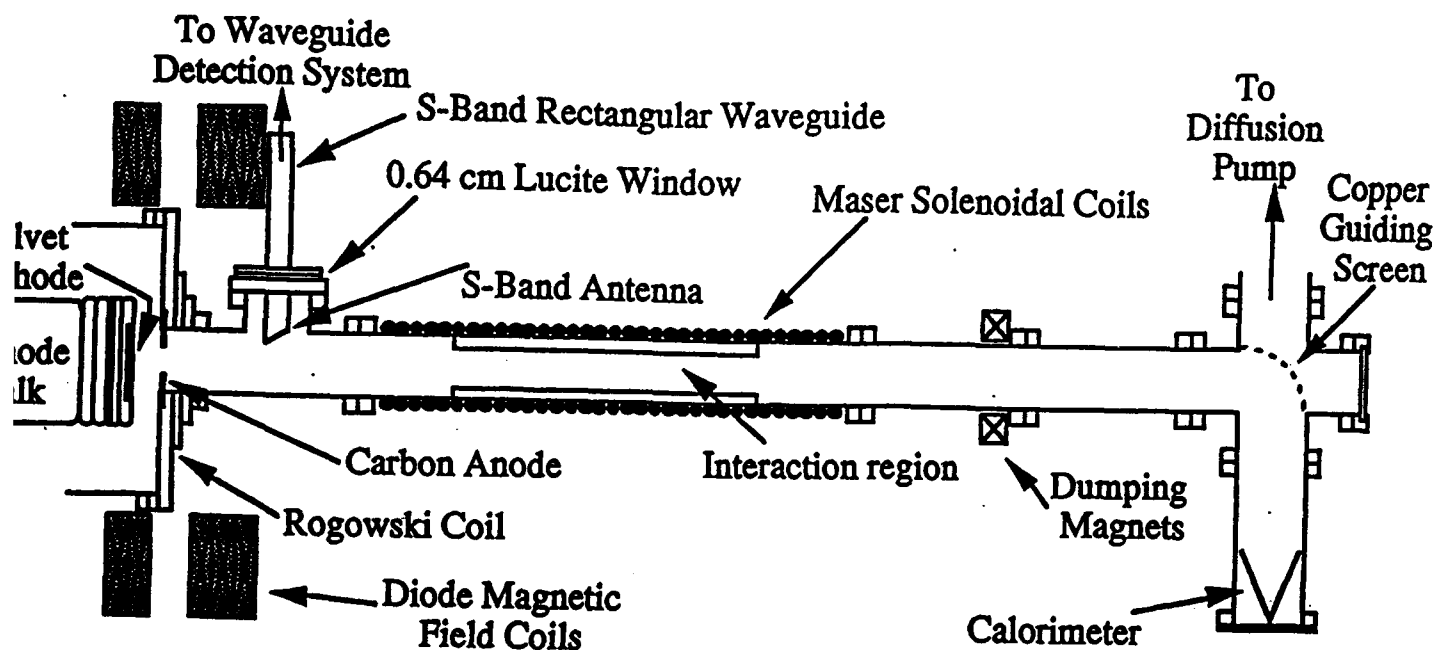


Figure 1. Experimental configuration of the initial gyro-BWO experiment at The University of Michigan

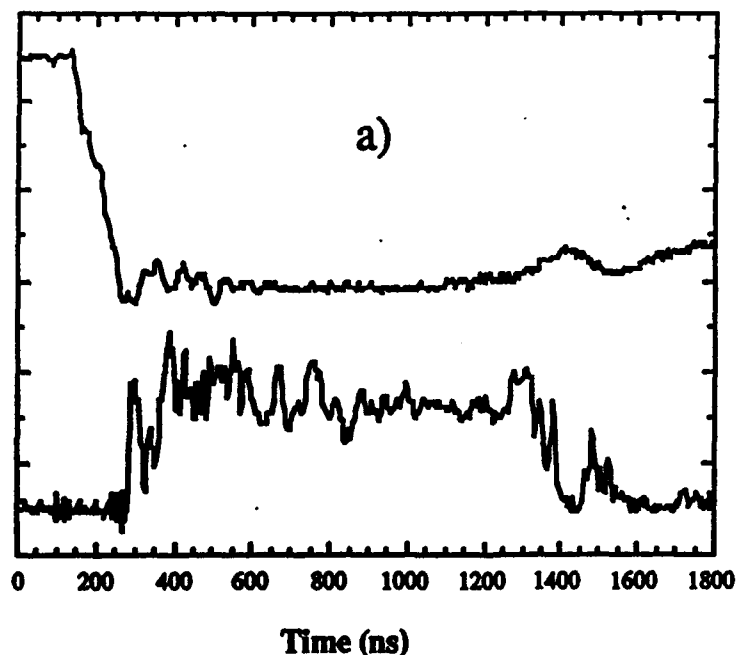


Figure 2. Long-pulse microwave emission from the initial gyro-BWO experiments at The University of Michigan. Top trace: beam voltage (310 kV/div); bottom trace: microwave signal ($3.2 \leq f \leq 6.6$ GHz). Peak extracted power ~120 kW; peak tube power 1.2 MW.

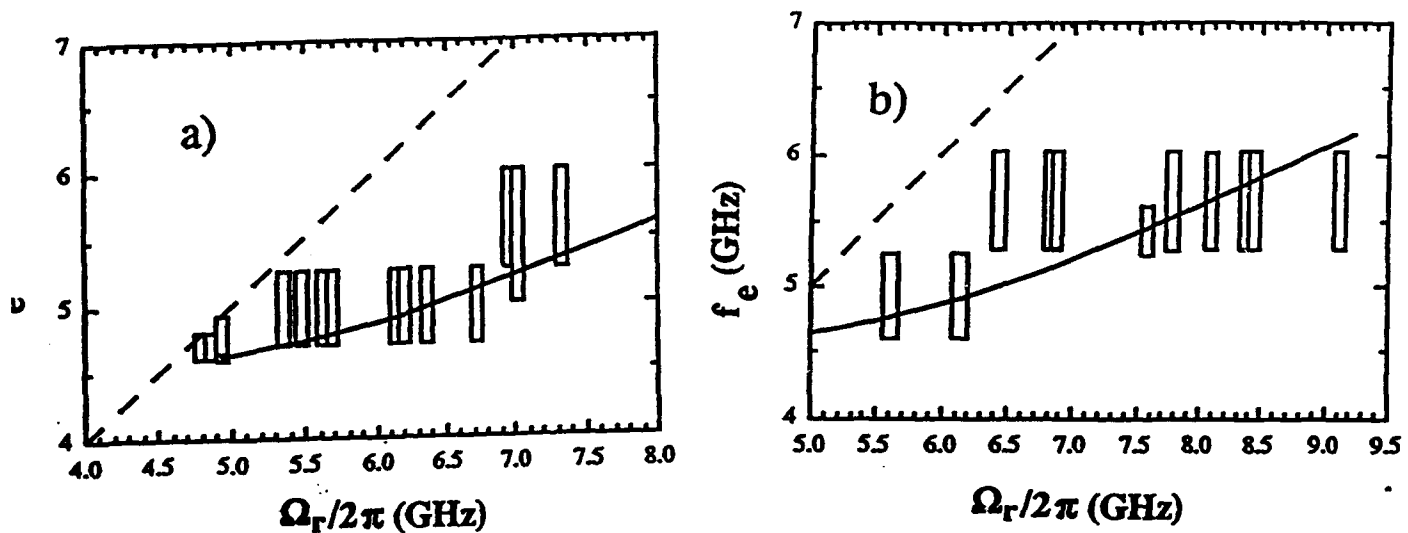


Figure 3. Gyro-BWO microwave emission frequency versus cyclotron frequency. Solid line is theoretical frequency; dashed line is $f_e = \Omega_c/2\pi$. a) solid beam data, b) annular beam data.

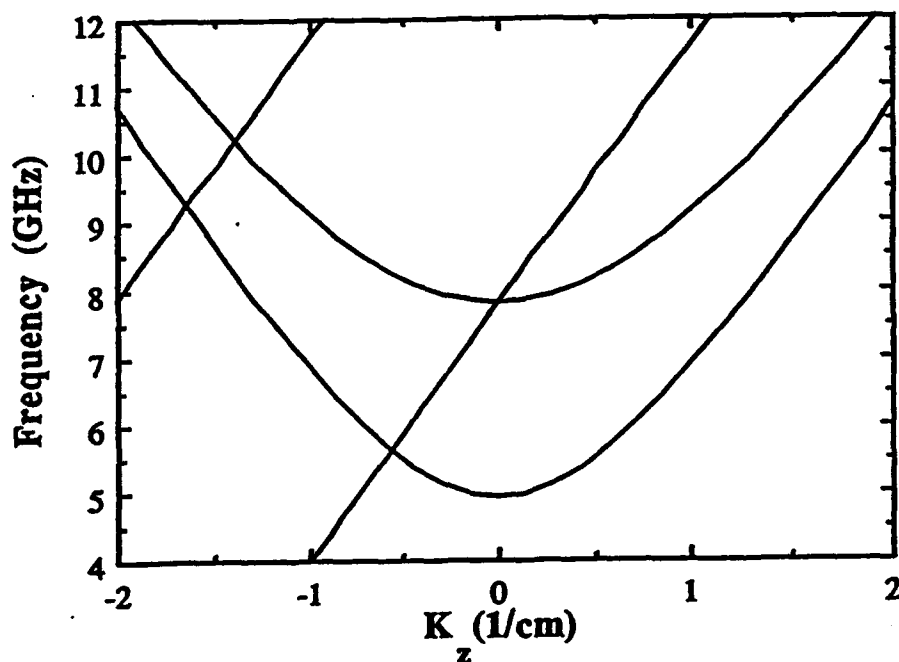


Figure 4. Dispersion relation for the gyrotron-backward-wave-oscillator.

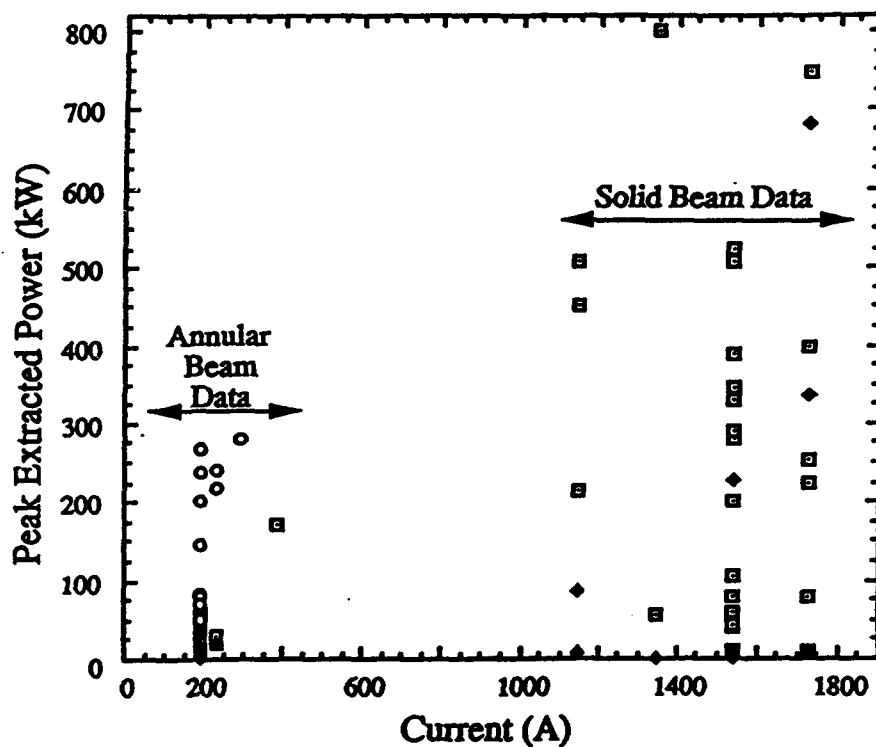


Figure 5). Microwave peak extracted power as a function of the beam current for the annular and solid electron beams. \square are the measured data points where $3.2 \leq f \leq 6.6$ GHz; \blacklozenge are the measured data points where $5.3 \leq f \leq 8$ GHz; and \circ are the measured data points obtained during the initial voltage overshoot where $3.2 \leq f \leq 6.6$ GHz.

2.3 Bragg Resonator Cyclotron Resonance Maser Experiments

Experiments were performed on a Bragg resonator with the original goal of obtaining cyclotron autoresonance maser (CARM) emission. The idea was that a Bragg resonator should provide high, selective feedback at a single frequency for each mode without increasing the low-frequency Q. Figure 6 shows the experimental configuration for these Bragg resonator experiments.

Two high-Q Bragg resonators have been built and utilized in high quality apertured e-beam CRM oscillator experiments. The first Bragg resonator (B1) was constructed with square corrugations and produced a Q of several thousand in the TE_{11} mode. The second Bragg resonator (B2) had sinusoidal corrugations and was designed to operate in the TE_{31} cavity mode. For resonator B-2, two symmetric, 15-period Bragg resonators were fabricated and placed on the ends of a 29.4 cm copper cavity section, with an estimated Q of about 4,700 in the TE_{31} mode at a frequency of 19 GHz.

A systematic study² was made of four cases in order to definitively identify gyrotron modes and absolute instabilities versus possible CARM modes:

- 1) Bragg resonator with ripples half-inward and large diameter smooth center section,
- 2) Large-diameter smooth tube with the same diameter as the above center section,
- 3) Bragg resonator with ripples fully outward and small diameter smooth center section, and
- 4) Small-diameter smooth tube with the same diameter as the case 3 center section.

The design mode of the device was the TE_{31} mode.

An apertured mask anode was developed which generated a high quality electron beam by means of 80 small holes drilled in a graphite anode plate. Cerenkov emission and radiation darkening on the glass plates gave estimates³ of the beam $\alpha = V_{\perp}/V_{\parallel}$ of about 0.55 and beam energy spread of $\Delta\gamma/\gamma = 7\%$; These measurements are described in further detail in section 2.5 and the article being published in the Review of Scientific Instruments (Appendix C).

The dispersion relations for the large number of possible competing modes are given in Figure 7. Detailed measurements were made of the frequency and mode patterns of the high power microwaves for Bragg resonators versus smooth tubes (Figure 8). Comparison of the microwave radiation properties for the above four cases gave the conclusion that the highest power radiation could be identified as parasitic oscillations of the following modes:

- a) TE_{21} absolute instability,
- b) TE_{11} gyro-BWO,
- c) Second (and possibly third) harmonic TE_{51} mode.

Table 1 summarizes these parasitic modes, which apparently suppressed the desired TE_{31} CARM mode. Absolute instability at the second cyclotron harmonic in the TE_{21} mode could also explain the high power levels

observed in our previous lower voltage CARM experiments.⁴ The MELBA Bragg resonator experiments are described in greater detail in Appendix C.

These experiments provided the first indications that the gyro-BWO was generating the highest powers and longest pulselengths of microwave radiation. Microwave mode patterns were measured by a diagnostic consisting of an array of fluorescent light tubes. Mode identification data (as in Figure 9), confirmed that the highest power and longest pulselengths were generated by the TE_{11} mode gyro-BWO. For this reason, the Bragg resonator configuration was discontinued and experiments were re-directed toward the gyro-BWO.

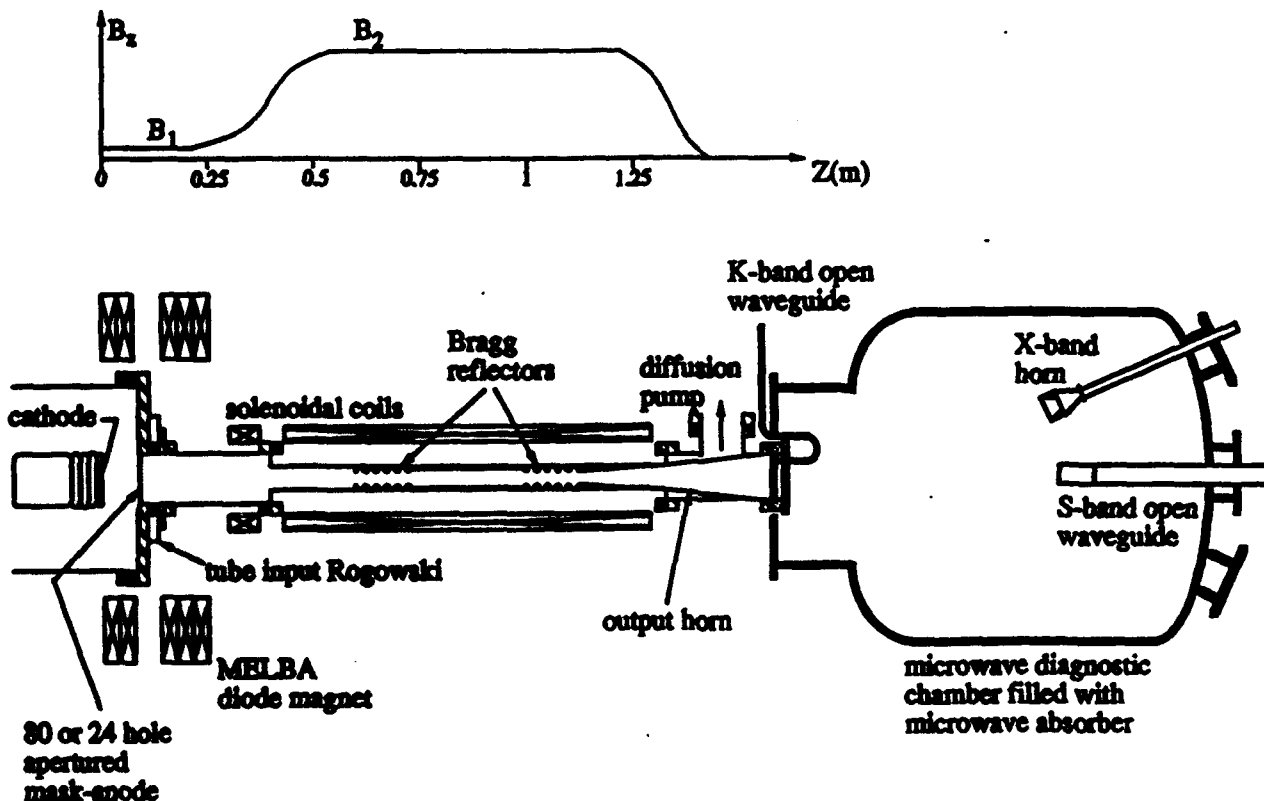
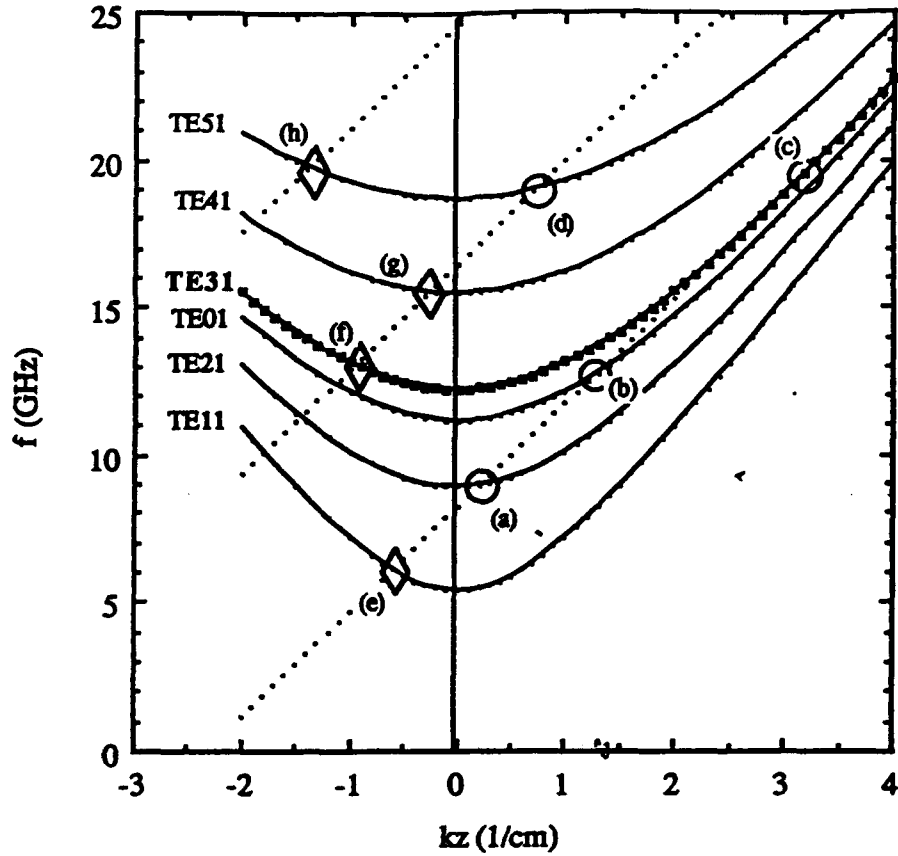


Figure 6. Experimental configuration for Bragg resonator cyclotron resonance maser experiments.



- (a) TE₂₁ gyrotron mode at fundamental
- (b) TE₀₁ gyrotron mode at fundamental
- (c) TE₃₁ CARM mode at fundamental
- (d) TE₅₁ gyrotron mode at second harmonic
- (e) TE₁₁ gyro-BWO mode at fundamental
- (f) TE₃₁ gyro-BWO mode at fundamental
- (g) TE₄₁ gyro-BWO mode at second harmonic
- (h) TE₅₁ gyro-BWO mode at third harmonic

Figure 7. Uncoupled CRM dispersion relations of TE waveguide modes and beam cyclotron modes ($s = 1, 2, 3$) for Bragg resonator with ripples fully outward (BRFO). The CRM parameters are: $V = 560$ kV, $B = 6.15$ kG, $\alpha = 0.63$, $r_w = 1.64$ cm.

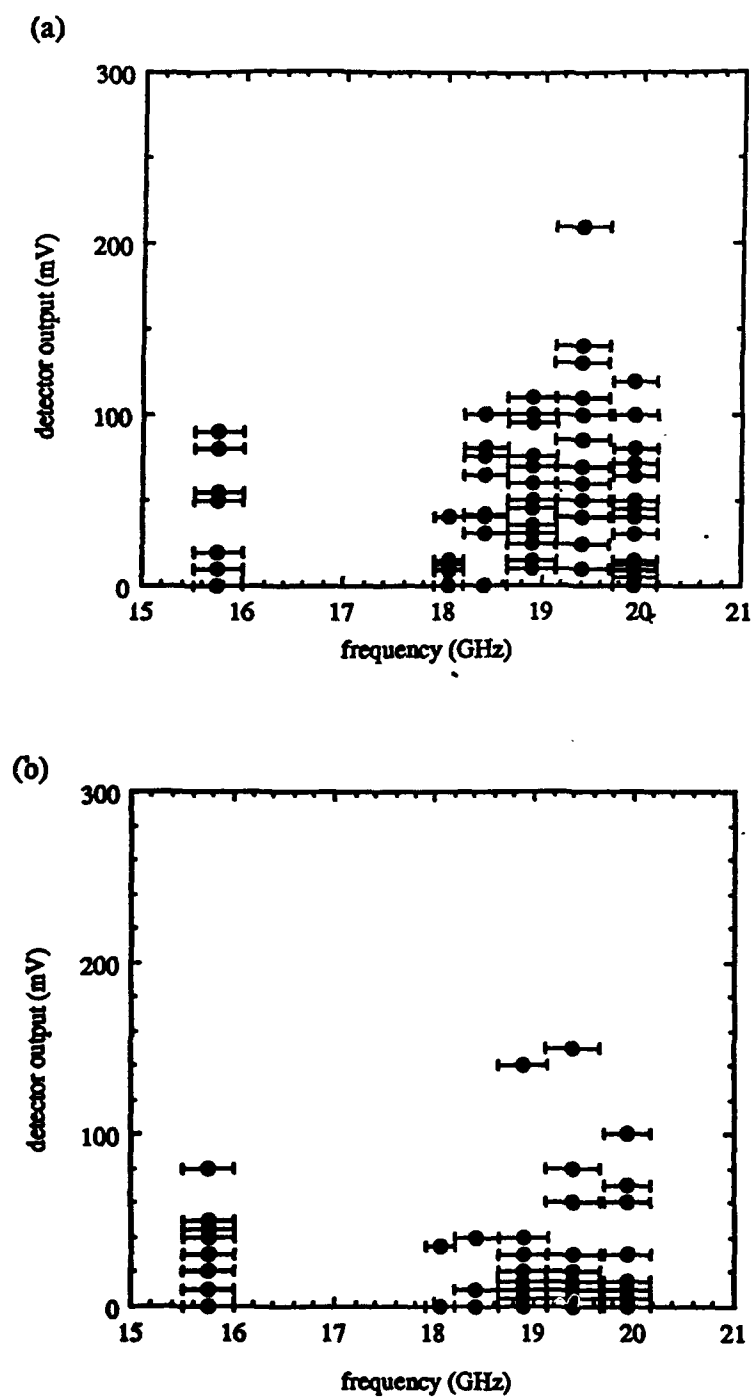


Figure 8. Data of frequency measurements for the case of (a) Bragg resonator BRFO and (b) small diameter ($r_w = 1.64$ cm) smooth tube without Bragg reflectors.

Table 1 SUMMARY OF MELBA MASER EXPERIMENTS

(high quality e-beam of 30 - 80 amps)

CONFIGURATION	freq(GHz)	power (MW)	η (%)	mode
Bragg resonator (ripples half inward, large diameter tube)	15.5-16	1.2	4	TE51 or TE61 second harmonic gyrotron
	2.1-6.6	> 8	> 15	TE11 gyro-BWO
Smooth tube (large diameter)	15.5-16	0.3	1	TE51 or TE61 second harmonic gyrotron
	2.1-6.6	1	2	TE11 gyro-BWO
Bragg resonator (ripples fully outward, small diameter tube)	18.7-19.2	> 0.2	> 0.7	possible TE31 CARM not confirmed
	19.2-19.7			
	6.6-10	0.05	0.2	TE21 absolute instability*
Smooth tube (small diameter)	2.1-6.6	< 0.001	< 0.01	TE11 gyro-BWO
	15.5-16 (mostly)	0.2	0.7	TE41 or TE51 @ 2 Ω c or TE51 gyro-BWO @ 3 Ω c
	6.6-10	0.05	0.2	TE21 absolute instability
	2.1-6.6	~ 1	6	TE11 gyro-BWO

* radiation pattern observed from fluorescent light tube diagnostic

M2431

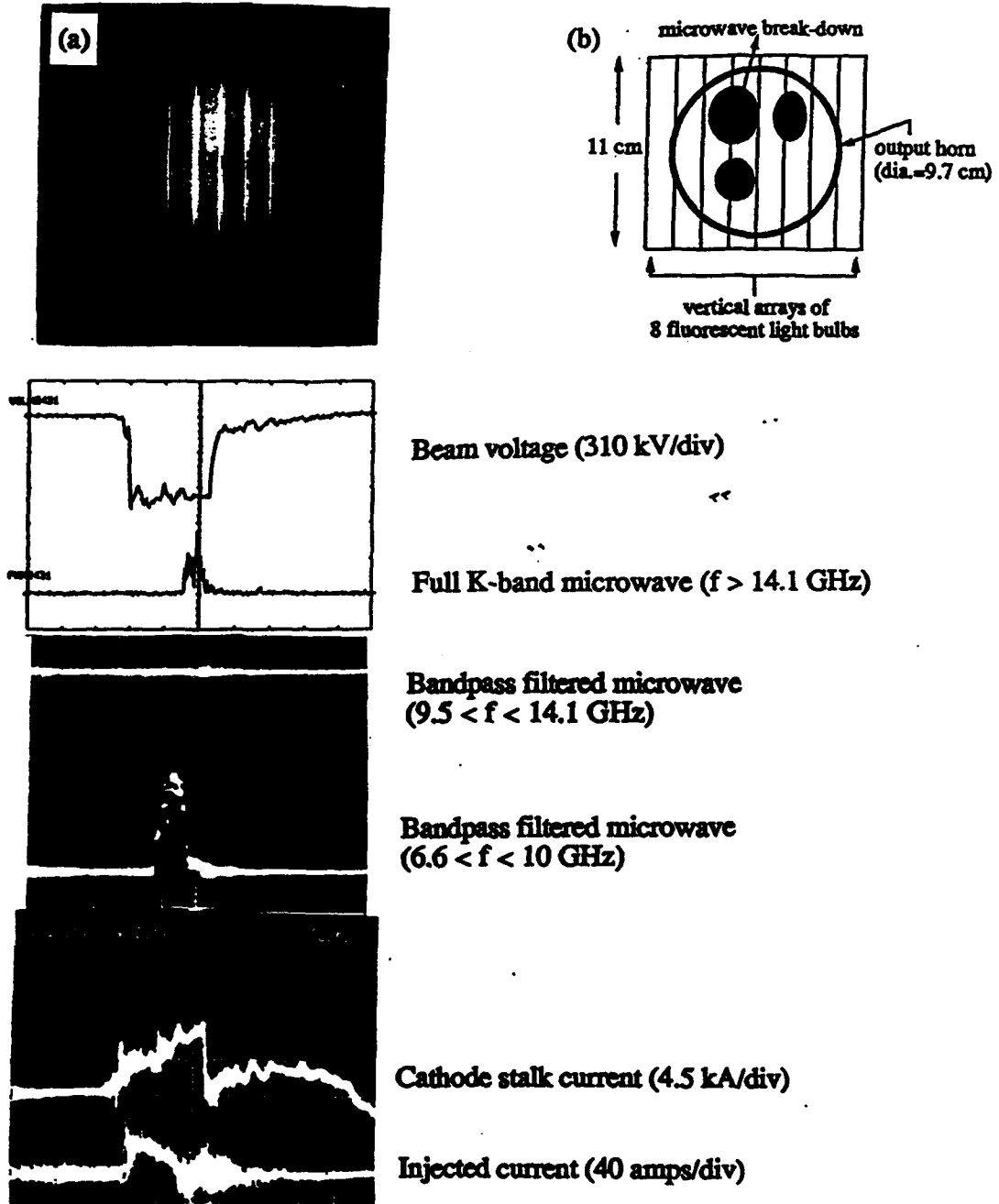


Figure 9 Experimental data (M2431) on fluorescent light tube diagnostic: (a) light emission from fluorescent light tubes (open shutter camera photo), (b) model of microwave breakdown on fluorescent light tubes. Diode magnetic field is 0.4 kG and cavity magnetic field is 6.25 kG. Sweep time is 200 ns/div.

2.4 MELBA Masers A1 and A2

Our initial experiments on MELBA Masers A1 and A2 investigated cyclotron maser emission from high current electron beams in unslotted cavities versus cavities slotted to suppress all non- TE_{0n} modes. The objective of these experiments was to run at close to grazing incidence with the fundamental cyclotron maser mode in the TE_{01} mode. As depicted in Figure 10, the planar velvet cathode was utilized with a large aperture in the graphite anode to extract the maximum e-beam current. The e-beam current extracted into the large diameter tube was about 6 kA, but only about 2 kA of this current passed through the smaller diameter cavity.

Typical microwave emission data from the unslotted cavity is presented in Figure 11. In this shot, the peak X-band power was in the range of 15-25 MW, but the duration of the microwave spike was only about 20-40 ns. The cause of the high power spiking behavior could have been mode jumping. In order to reduce mode competition from the large number of non-axisymmetric modes a slotted cavity was fabricated to select the TE_{01} mode. Experiments with the slotted cavity generated high K-band radiation (16-20 GHz) power spikes (up to MW); the unslotted cavity gave high X-band power, shown in Figure 12.

Another aspect of the early experiments concerned the fact that high current operation with a solid beam gave a relatively hot electron beam with large spread in beam alpha ($\alpha = V_{\perp}/V_{\parallel}$). The high current e-beam was therefore found to be unsuitable for single-mode, high efficiency, and high frequency operation. Therefore the apertured mask anodes were investigated, as described in section 2.5.

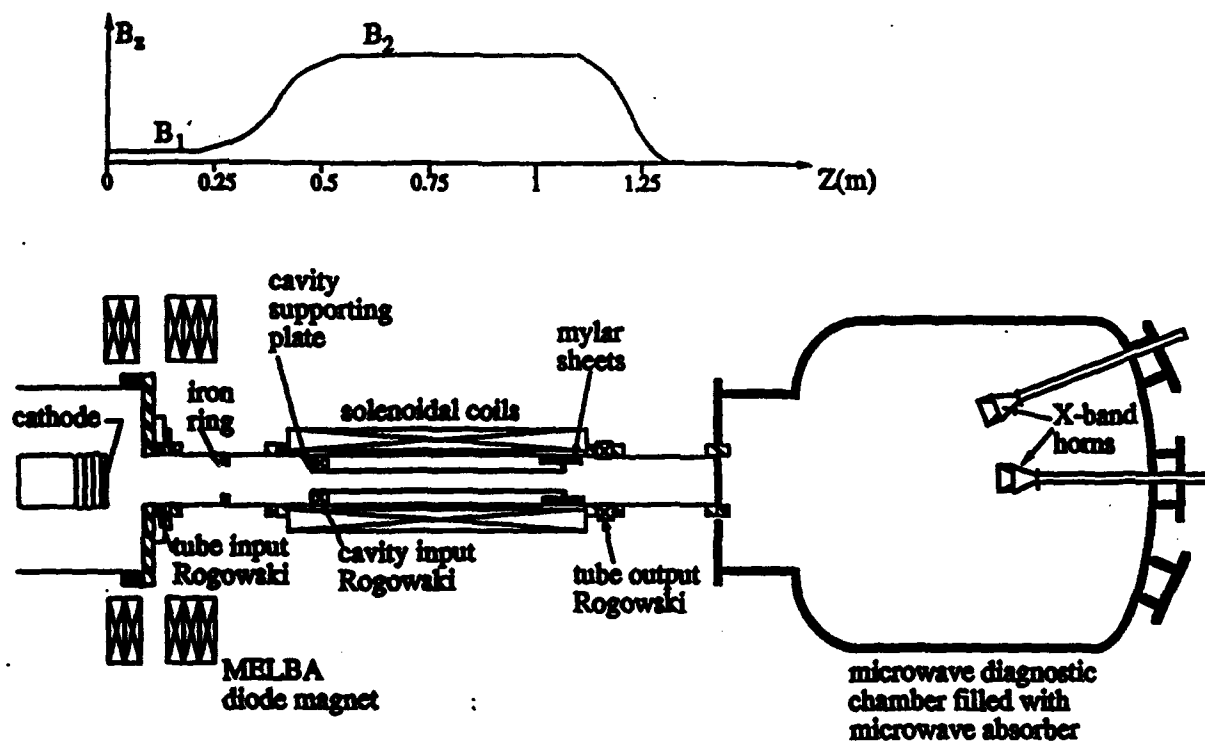
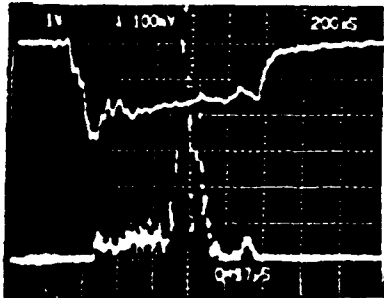


Figure 10. Experimental configuration for MELBA masers A1 and A2.

M1571 B=3.6 kG

200 ns/div

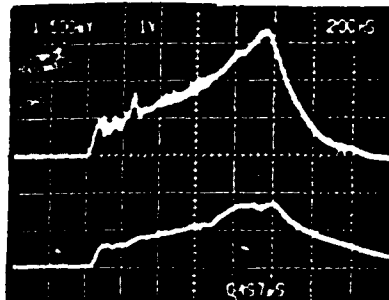


Top: Beam Voltage

(310 kV/div)

Bottom: X-band Microwaves

(6.6 GHz < f < 14.1 GHz)



Top: Tube Input Current

(1.9 kA/div)

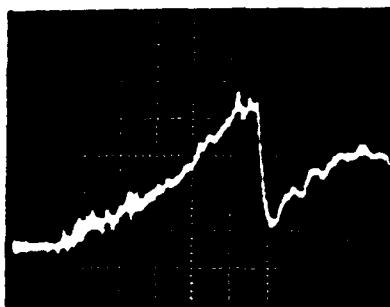
Bottom: Cavity Input Current

(1.2 kA/div)



Tube Output Current

(0.9 kA/div)



Cathode Stalk Current

(4.5 kA/div)

Figure 11. *Experimental data from MELBA maser A1 (unslotted cavity).*

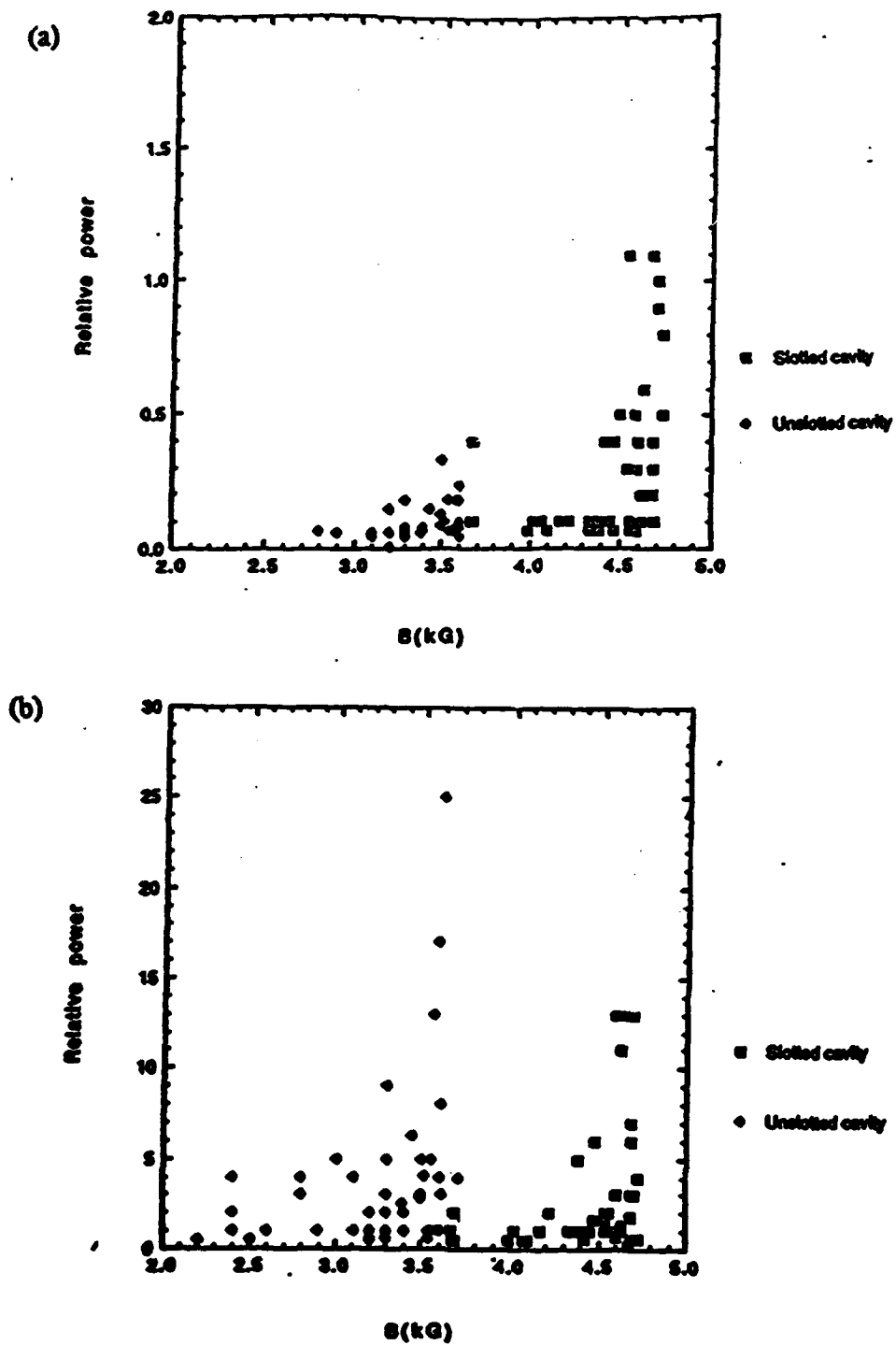


Figure 12. Microwave emission from maser A1 (unslotted cavity) versus maser A2 (slotted cavity). a) K-band peak power vs. B , b) X-band peak power vs. B .

2.5 Electron Beam Generation and Diagnostics

A high quality electron beam with low energy-spread is crucial for efficient cyclotron resonance maser oscillation. For masers operating on higher order cavity modes, it is desirable to utilize annular beams, near the wall of the Bragg resonator. To this end, we developed the apertured mask anode (AMA), in which an annular array of small (1.1 mm diameter) apertures are drilled in the (3 mm-thick) anode plate. About 1 ampere of low-emittance electron beam current flows through each aperture. For Bragg resonator CRM experiments, 80 apertures were used to generate an 80 A annular beam.

The electron beam alpha and velocity spread were measured by a Cerenkov plate technique³. In Cerenkov plate electron beam characterization studies, only 8 anode apertures were used. Adiabatic compression by a factor of ten in the magnetic field increases the beam alpha (V_{\perp}/V_{\parallel}), such that the Larmor radius is large enough to be measured by Cerenkov light emission (on a gated-microchannel plate camera) and by radiation darkening on the glass, (see Appendix C). We have found that the measured e-beam Larmor radius for the MELBA Maser B2 corresponds to a beam alpha of 0.55; Busch's theorem can be used to calculate the beam alpha for other values of the diode and solenoidal field. These experimental data are in good agreement with results of the Stanford Electron Optics (Hermannsfeldt) code. The thickness of the radiation darkened rings can be used to measure axial beam energy spread ($\Delta\gamma_z/\gamma_z$), which is estimated to be in the range of less than about 7%. The MELBA Maser diode has also been modeled on the MAGIC code, permitting calculation of electron beam energy spread. This can be used to predict energy spread in the microwave cavity region.

References

- 1) T. A. Spencer, R. M. Gilgenbach, and J. J. Choi, "Gyrotron Backward Wave Oscillator Experiments Utilizing a High Current, High Voltage, Microsecond Electron Accelerator", submitted to Applied Physics Letters
- 2) J. J. Choi, R. M. Gilgenbach, and T. A. Spencer, "Mode Competition in Bragg Resonator Cyclotron Resonance Maser Experiments Driven by a Microsecond Intense Electron Beam Accelerator", Accepted for Publication in International Journal of Electronics, 7th Special Issue on Gyrotrons, 1992
- 3) J.J. Choi, R.M. Gilgenbach, T.A. Spencer, P.R. Menge, and C.H. Ching, "Measurements of Relativistic Electron Beam Perpendicular-to- Parallel Velocity Ratio by Cerenkov Emission and Radiation Darkening on a Glass Plate", Review of Scientific Instruments, in press for February 1992
- 4) J.G. Wang, R.M. Gilgenbach, et al, "Frequency Tunable, High Power Microwave Emission from Cyclotron Autoresonance Maser Oscillation and Gyrotron Interactions", IEEE Trans. Pl. Sci., 17 906 (1989)

Appendix A

Ph.D. Dissertations Resulting from this Research

- 1) T. A. Spencer (supported on Air Force Laboratory Graduate Fellowship), "High Current, Long-Pulse Gyrotron Backward Wave Oscillator Experiments", defended in May 1991
- 2) J. J. Choi, (supported by AFOSR) "Bragg Resonator Cyclotron Maser Experiments Driven by a Microsecond Intense Electron Beam Accelerator", defended in April 1991

Abstracts for these dissertations are given below.

HIGH CURRENT, LONG-PULSE GYROTRON-BACKWARD-WAVE OSCILLATOR EXPERIMENTS

by
Thomas Allen Spencer

Chairman: Ronald M. Gilgenbach

Experiments have been conducted on cyclotron resonance maser interactions to generate high power microwaves employing a long-pulse electron beam accelerator, MELBA (Michigan Electron Long Beam Accelerator), with electron beam parameters of: $V = 0.6 - 0.9$ MV; Current = 1-50 kA; and pulselength = 0.5 - 1.5 μ s. To generate high power and long-pulse microwaves, the interaction cavity and magnetic field were designed to excite the TE_{11} fundamental mode gyrotron backward wave. Two types of electron beam are employed. One is an annular electron beam of $\sim 150 - 250$ amps which is extracted through an apertured-mask anode (24 five mm holes). The other is a solid electron beam of 1 - 2 kA which is extracted through a two inch diameter aperture. An S-Band, Vlasov-type antenna (with an efficiency of $\sim 10\%$) is used to detect the backward wave power at the diode end of the interaction cavity. A series of high pass waveguide, low pass coaxial and cylindrical cavity frequency filters are employed to show the existence of the gyro-backward-wave, as well as show the magnetic tunability of the gyrotron-backward-wave. In the solid beam case (1 - 2 kA), about 300 - 800 kW of extracted microwave power was detected in the waveguide detection system, implying that approximately 3 - 8 MW (efficiency $\sim 1 - 2\%$) of power is generated from the gyro-BWO device. The pulselengths for the solid beam case were from 300 - 600 ns (essentially the total flat-top voltage pulselength) over a frequency range of 4.5 - 6 GHz. The annular beam generated approximately 10 - 80 kW extracted microwave power for voltages of 600

- 650 kV (device efficiency of $\sim 0.1 - 1\%$) and about 100 - 300 kW of extracted microwave power (device efficiency of 1 - 2%) for voltages of 850 - 900 kV. Pulselengths for the 600 - 650 kV interaction were from 100 - 600 ns for a frequency range of 4.5 - 6 GHz, and pulselengths for the 850 - 900 kV interaction were from 40 - 100 ns (which corresponds to the initial overshoot of the voltage pulse) for a frequency range 4.5 - 6 GHz.

ABSTRACT

BRAGG RESONATOR CYCLOTRON RESONANCE MASER EXPERIMENTS DRIVEN BY A MICROSECOND, INTENSE ELECTRON BEAM ACCELERATOR

by

Jin Joo Choi

Chair: Prof. Ronald M. Gilgenbach

The cyclotron resonance maser (CRM) has proven to be attractive for many high power microwave applications such as fusion plasma heating, radar/communications, and high gradient RF accelerators. Most of the previous CRM experiments with MV electron beams have been conducted with short ($< 0.1 \mu\text{sec}$) pulses. The present work contains the first comprehensive experimental study on mode competition in a high-Q Bragg resonator CRM employing a microsecond, relativistic electron beam.

We have designed and fabricated a high-Q sinusoidal Bragg resonator designed to excite high frequency CARM oscillation of the TE_{31} cylindrical cavity mode at 18.9 GHz. The measured reflectivity of the TE_{31} mode is consistent with the prediction of uncoupled single mode theory.

A high quality annular electron beam with low velocity spread and energy spread

is produced through an apertured mask-anode. The apertured electron beam has been characterized by the use of glass plate diagnostics. The measured beam velocity ratio, v_1/v_0 , was shown to be in agreement with computer simulation results and the theoretical predictions.

Experiments have been performed for 4 cases: (1) Bragg resonator with ripples half-inward, (2) large diameter smooth tube without Bragg resonator, (3) Bragg resonator with ripples fully-outward, and (4) small diameter smooth tube without Bragg resonator.

The Bragg resonator with ripples half-inward generated high power microwave radiation from TE_{11} gyro-BWO interactions, TE_{21} absolute instability, and high harmonic gyrotron modes. Considerably less power from the TE_{11} gyro-BWO was observed for the Bragg resonator with ripples fully-outward. The microwave emission from the TE_{21} absolute instability in the Bragg resonator with ripples fully-outward was successfully suppressed by lowering the cavity magnetic field.

These three undesired oscillations, (TE_{21} absolute instability, TE_{11} gyro-BWO, TE_{51} second and third harmonic), were the most serious competing modes in the present Bragg resonator CRM experiments, apparently suppressing the TE_{31} CARM oscillation.

For the Bragg resonator with ripples half-inward, we have performed gyrotron experiments with a high current electron beam. In these experiments, we have observed mode competition between the TE_{21} absolute instability and the TE_{11} gyro-BWO interaction by the use of frequency measurements and gas breakdown diagnostics.

Appendix B

Publications Supported by This Grant

- 1) T. A. Spencer, R. M. Gilgenbach, and J. J. Choi, "Gyrotron Backward Wave Oscillator experiments utilizing a High Current, High Voltage, Microsecond Electron Accelerator", submitted to Applied Physics Letters
- 2) J. J. Choi, R. M. Gilgenbach, and T. A. Spencer, "Mode Competition in Bragg Resonator Cyclotron Resonance Maser Experiments Driven by a Microsecond Intense Electron Beam Accelerator", Accepted for Publication in International Journal of Electronics, 7th Special Issue on Gyrotrons, 1992
- 3) J.J. Choi, R.M. Gilgenbach, T.A. Spencer, P.R. Menge, and C.H. Ching, "Measurements of Relativistic Electron Beam Perpendicular-to- Parallel Velocity Ratio by Cerenkov Emission and Radiation Darkening on a Glass Plate", Review of Scientific Instruments, in press for February 1992
- 4) J.G. Wang, R.M. Gilgenbach, et al, "Frequency Tunable, High Power Microwave Emission from Cyclotron Autoresonance Maser Oscillation and Gyrotron Interactions", IEEE Trans. Pl. Sci., 17 906 (1989)

Appendix C) Copies of Publications Supported by This Grant

submitted to Applied Physics Letters

Gyrotron-backward-wave-oscillator experiments utilizing a high current, high voltage, microsecond electron accelerator

Thomas A. Spencer, Ronald M. Gilgenbach, and Jin J. Choi*

*Intense Energy Beam Interaction Laboratory, Nuclear Engineering Department,
University of Michigan, Ann Arbor, Michigan 48109-2104*

We report the first gyrotron backward-wave-oscillator experiments to produce high power (tube power of $\sim 1 - 8$ MW), long-pulse ($0.3 - 1.2 \mu\text{s}$) microwaves at high currents ($0.1 - 2$ kA) and high voltages ($650 - 750$ kV). Experiments were performed in the TE_{11} fundamental backward-wave mode, with efficiencies of $\sim 1 - 2\%$. Mode competition was observed which is believed to originate from the TE_{21} absolute instability.

Electron cyclotron resonance masers (ECMs) have the potential of producing high power microwaves for many applications such as fusion plasma heating¹, bulk material heating², and radar. Gyrotron backward wave oscillators (gyro-BWOs) make excellent high power devices due to the relative insensitivity to beam velocity spread and beam voltage fluctuations when compared to other electron cyclotron resonance devices like the gyro-TWT^{3,4}, gyrotron⁵, and CARM⁶. This insensitivity to beam velocity spread and voltage fluctuation allows the use of a low quality electron beam generated from explosive emission cathodes used in accelerators which produce gigawatts of e-beam power. Gyro-BWOs have the advantage of being fast-wave devices and employing a simple hollow tube. This leads to the possibility of enhanced power handling capabilities, since a periodic structure is not necessary as in conventional backward-wave-oscillator devices. Previous and recent gyro-BWO experiments have concentrated on low current (< 10 amps) and moderate voltage (< 100 kV) e-beams, and have obtained 1 -10 kW of output power with efficiencies of up to 15%⁷⁻⁹.

In this letter, we report the first gyro-BWO experiments employing a high voltage (600 - 750 kV), high current (150 - 2000 A), long-pulse (0.5 - 4 μ s) electron beam

The experimental configuration is shown in Figure 1. The electron beam produced by MELBA (Michigan Electron Long Beam Accelerator)¹⁰ is emitted from a cotton velvet cathode surface in a uniform magnetic field. The e-beam is extracted through a carbon anode, and then adiabatically compressed by the maser solenoidal coils as it propagates towards the interaction region. Experiments utilized either of two anodes. The first anode gave an annular e-beam of 150 - 300 amps extracted through 24 holes of 5 mm in diameter drilled on a circle of 2.52 cm radius on a carbon plate. A second type of anode generated a solid e-beam of 1 - 2 kA extracted through a 5.1 cm diameter hole. The maser solenoidal magnetic field and the smooth interaction tube are designed to excite the TE₁₁ fundamental mode backward-wave. The maser solenoidal coils, which generate a magnetic field of 3 - 7 kG, and the diode magnetic field coils, with a magnetic field range of 0.4 - 0.9 kG, are independently pulsed to allow control over the e-beam velocity ratio, $\alpha = v_{\perp}/v_{\parallel}$. The interaction tube has a radius of 1.93 cm, which sets a TE₁₁ mode cutoff frequency of 4.55 GHz, and a length of 50.5 cm. After exiting the interaction region, the e-beam

is deflected into the wall of the drift tube by a pair of permanent magnets. The backward wave generated in the interaction region is extracted at the diode end of the experiment by a modified S-Band rectangular waveguide antenna, which is cut at a 30° angle relative to the broad wall and collects about 9% - 11% of the tube power. After extraction, the microwave signal travels through a 0.64 cm lucite window and through a waveguide detection system that consists of several different bands of rectangular waveguide and coaxial low pass filters to determine the frequency range of the interaction (G-band, $f_{co} = 3.15$ GHz; J-band, $f_{co} = 4.30$ GHz; and H-band, $f_{co} = 5.27$ GHz). The signals are detected by coaxial diode detectors and displayed on fast oscilloscopes. A calorimeter is located at the downstream end of the experiment to measure the reflected backward wave energy for comparison to that detected in the waveguide detection system located at the diode end. A copper guiding screen is used to direct the microwaves onto the calorimeter, which is placed 90 degrees off-axis so that the e-beam will not strike the calorimeter.

The uncoupled dispersion relation¹¹ for an electron beam interacting with a waveguide can be obtained by simultaneously solving the waveguide vacuum modes

$$\omega^2 - \omega_{co}^2 - k_z^2 c^2 = 0 \quad (1)$$

and the beam cyclotron modes,

$$\omega - k_z v_{z0} - s\Omega_r = 0 \quad (2)$$

where ω_{co} is the cavity cutoff frequency, k_z is the axial wavenumber, c is the speed of light, v_{z0} is the axial velocity of the beam, s is the harmonic number ($s = 1$ is the fundamental mode), and Ω_r is the relativistic cyclotron resonance frequency, $\Omega_r = eB/\gamma m$ where e is the electron charge, B is the magnetic field, γ is the relativistic factor, and m is the mass of the electron.

Figure 2 shows an uncoupled, e-beam-filled cavity dispersion relation that illustrates the TE_{11} fundamental cyclotron mode ($s=1$) and second harmonic ($s=2$) backward-wave intersections, as well as the TE_{21} mode intersections for typical parameters used in the experiments: $V_{beam} = 750$ kV; $I_{beam} = 2$ kA, $\alpha = 0.65$; B-field = 6.3 kG.

Figure 3 depicts typical data obtained for the solid and annular e-beams. The top traces of Figures 3(a), 3(b) and 3(c) show accelerator voltage pulses. The bottom trace of Figure 3(a), and

the center traces of 3(b) and 3(c) show microwave data signals detected in the frequency range of $3.2 \leq f \leq 6.6$ GHz. The bottom traces of Figures 3(b) and 3(c) show microwave data signals detected in the frequency range of $5.3 \leq f \leq 8$ GHz. The center and bottom traces of Figures 3(b) and 3(c) are on approximately the same scale. Figure 3(a) depicts the signals obtained for the solid beam ($I_{\text{beam}} \sim 1.5$ kA) at a magnetic field of 4.8 kG, and demonstrates the microwave signal exists almost solely in the range of $3.2 \leq f \leq 5.3$ GHz. The peak of the emission signal corresponds to ~ 120 kW of extracted power, or ~ 1.2 MW of tube power. Figure 3(a) also shows that the emission signal remains within the frequency band throughout the flattop of the voltage pulse, ~ 1.2 μ s in duration.

As the magnetic field is increased, the microwave signal is detected in both frequency ranges, as demonstrated in Figure 3(b) ($B = 6.6$ kG), which shows the microwave data signal lies within $5.3 \leq f \leq 6$ GHz. The peak of the microwave emission corresponds to ~ 550 kW of extracted power (about 5.5 MW of tube power). Based on the data given by Figures 3(a) and 3(b), and the dispersion relations, the emission signals were determined to be the TE_{11} fundamental mode gyrotron backward-wave interaction. The last peak of the microwave data signal in the bottom trace of Figure 3(b) has a frequency range of $6.6 \leq f \leq 8$ GHz, and could be the TE_{21} fundamental mode absolute instability (as shown in Figure 2) competing with the fundamental TE_{11} gyrotron backward-wave interaction. Also observed (but not shown) in the solid beam experiments was short-pulsed, spiky emission believed to originate from the TE_{11} second harmonic gyrotron backward-wave, with the extracted power approximately 10 kW, less than a tenth of that seen for the fundamental TE_{11} mode. Figure 3(c) shows typical microwave signals for the annular beam ($I_{\text{beam}} \sim 200$ amps, $B = 5.0$ kG) which demonstrate long-pulse microwaves of ~ 630 ns in the frequency range of $3.2 \leq f \leq 5.3$ GHz. The emission signal peak corresponds to ~ 80 kW of extracted microwave power (~ 0.8 MW of tube power), about one-tenth of that observed with the solid beam.

Proof that the interaction is the TE_{11} fundamental backward-wave interaction is demonstrated in two ways. The first is that the emission frequency is shown to be less than that of the cyclotron resonance frequency ($\Omega_e/2\pi$) for both the solid and annular e-beams, as shown in Figure 4. The

solid line in Figure 4(a) gives the theoretical frequency for an uncoupled e-beam-filled cavity dispersion relation with $\alpha = 0.65$, and $I_{\text{beam}} = 1.5$ kA. The solid line in Figure 4(b) gives the theoretical frequency with $\alpha = 0.65$ and $I_{\text{beam}} = 300$ amps. The dashed line in Figures 4(a) and 4(b) is the emission frequency equal to the cyclotron resonance frequency ($f_c = \Omega_r/2\pi$). Note that all the measured frequencies lie below this line and thus the interaction is the backward wave. For the annular beam, the value of α has been determined from both Cerenkov and radiation darkening of a glass plate¹², and from the EGUN code¹³. For the solid e-beam, the spread in alpha is large, from 0.05 - 0.7. The second way to demonstrate the existence of the backward wave is that the frequency of interaction increases as the magnetic field increases, as shown in Figures 3(a), 3(b) and 4.

Figure 5 shows a summary of the annular and solid beam data. The solid beam provided the highest extracted powers (300 - 800 kW), typically five to ten times higher than that of the annular beam (10 - 80 kW) with similar e-beam and magnetic field parameters. The solid e-beam is expected to couple more strongly to the TE_{11} mode which has a peak of the electric field on-axis. For the annular beam, higher extracted powers (depicted by open circular data points in Fig. 5) were obtained for higher electron beam voltages (850 - 950 kV) corresponding to the initial overshoot of the voltage pulse. This increased energy with the annular beam is due to the electrons having more perpendicular energy at higher beam voltages to amplify the electromagnetic waves. Based on the value of I_{beam} for the solid and annular e-beams, the efficiencies are determined to be approximately the same (about 1 - 2% overall device efficiency), demonstrating the gyro-BWO is insensitive to the e-beam energy spread. The relatively low efficiency may be due to the low α and space-charge limiting effects, or reabsorption of microwave power in the tube region. Saturation effects at high currents have been previously observed in Russian gyrotron experiments.¹⁴

In summary, the gyro-BWO has been shown to produce high power (tube power of $\sim 1 - 8$ MW), long-pulse (0.3 - 1.2 μs) microwaves at high currents (0.1 - 2 kA) and high voltages (650 - 750 kV) in the TE_{11} fundamental backward-wave mode, with efficiencies of about 1 - 2%. Also

observed was possible mode competition from the TE_{21} absolute instability, and short-pulse emission believed to originate from the TE_{11} second harmonic backward-wave interaction.

This research was supported by the Air Force Office of Scientific Research and the Air Force Phillips Laboratory. Thomas Spencer was supported by an Air Force Laboratory Graduate Fellowship. We thank P. R. Menge and C. H. Ching for experimental assistance.

*Present address: Science Applications Inc., McLean, VA.

References

- ¹R. M. Gilgenbach, et al., Phys. Rev. Lett. 44, 647 (1980)
- ²J. H. Booske, Private Communication
- ³Y. Y. Lau, K. R. Chu, L. R. Barnett, and V. L. Granatstein, Int. J. Infr. and Millimeter Waves, 2, 373 (1981)
- ⁴S. H. Gold, et al., J. Appl. Phys., 69, 6696 (1991)
- ⁵J. L. Hirshfield, *Infrared and Millimeter Waves Vol. I* (Academic Press, New York, 1979)
- ⁶G. Bekefi, A. DiRienzo, C. Leibovitch, and B. G. Danly, Appl. Phys. Lett. 54, 1302 (1989)
- ⁷S. Y. Park, V. L. Granatstein, and R. K. Parker, Int. J. Electron., 57, 1109 (1984)
- ⁸S. Y. Park, et al., IEEE Trans. Plasma Sci., PS-18, 321 (1990)
- ⁹P. Muggli, M. Q. Tran, and T. M. Tran, Phys. Fluids B, 3, 1315 (1991)
- ¹⁰R. M. Gilgenbach, et al., Proceedings of the Fifth IEEE Pulsed Power Conference (1985)
- ¹¹A. W. Fliflet, Int. J. Electron., 61, 1049 (1986)
- ¹²J. J. Choi, R. M. Gilgenbach, T. A. Spencer, P. Menge, and C. H. Ching, to be published in Rev. Sci. Inst., Feb 1992
- ¹³W. Hermannsfeldt, SLAC Report 226, 1979
- ¹⁴N. S. Ginzberg, V. I. Kremmentsov, M. I. Petelin, P. S. Strelkov, and A. K. Shkvarunets, Sov. Phys. Tech. Phys., 24, 218 (1979)

Figure Captions

Figure 1) Experimental Configuration

Figure 2) The uncoupled, e-beam-filled cavity dispersion relations illustrating the fundamental ($s=1$) and second ($s=2$) harmonic intersections between the TE_{11} and TE_{21} cavity and e-beam modes. The parameters are: $V_{\text{beam}} = 750$ kV; $I_{\text{beam}} = 2$ kA, $\alpha = 0.5$; B-field = 6.3 kG.

Figure 3) Experimental data signals. (a) top trace: Voltage (310 kV/div); bottom trace: microwave signal, $3.2 \leq f \leq 6.6$ GHz, peak extracted power ~ 120 kW. (b) and (c) top trace: Voltage (310 kV/div); center trace: microwave signal, $3.2 \leq f \leq 6.6$ GHz; bottom trace: microwave signal, $5.3 \leq f \leq 8$ GHz. The center trace in (b) has a signal peak corresponding to ~ 550 kW of extracted power, while the center trace in (c) has a signal peak of ~ 80 kW of extracted power. (a) and (b) are data from the solid e-beam experiments, and (c) is data from the annular e-beam experiments.

Figure 4) The measured emission frequency as a function of the relativistic cyclotron frequency. The dashed line is the $f_e = \Omega_r/2\pi$ line. (a) is the solid beam data, where the solid line is the theoretical frequency for an uncoupled e-beam-filled dispersion relation for $\alpha = 0.65$, and $I_{\text{beam}} = 1.5$ kA. (b) is the annular beam data, where the solid line is the theoretical frequency for $\alpha = 0.65$ and $I_{\text{beam}} = 300$ A.

Figure 5). Microwave peak extracted power as a function of the beam current for the annular and solid electron beams. \square are the measured data points where $3.2 \leq f \leq 6.6$ GHz; \blacklozenge are the measured data points where $5.3 \leq f \leq 8$ GHz; and \circ are the measured data points obtained during the initial voltage overshoot where $3.2 \leq f \leq 6.6$ GHz.

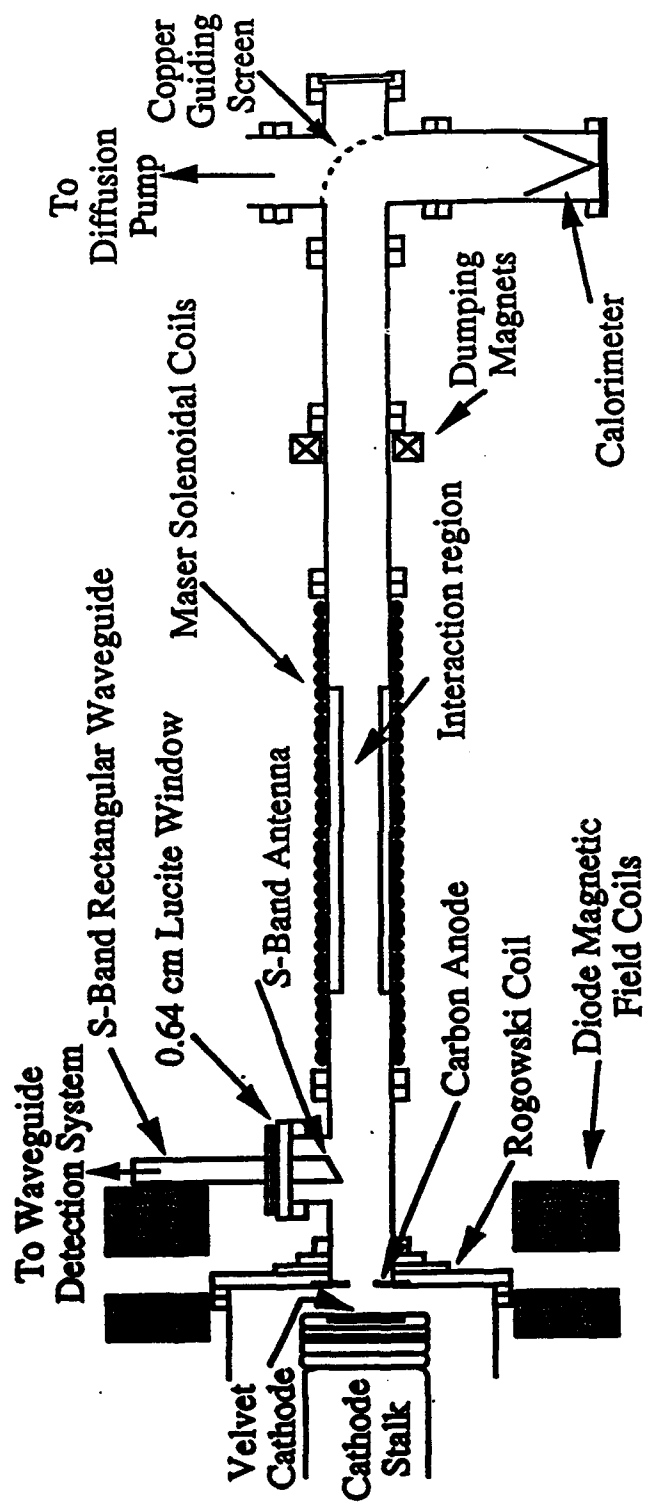


Figure 1) Experimental Configuration

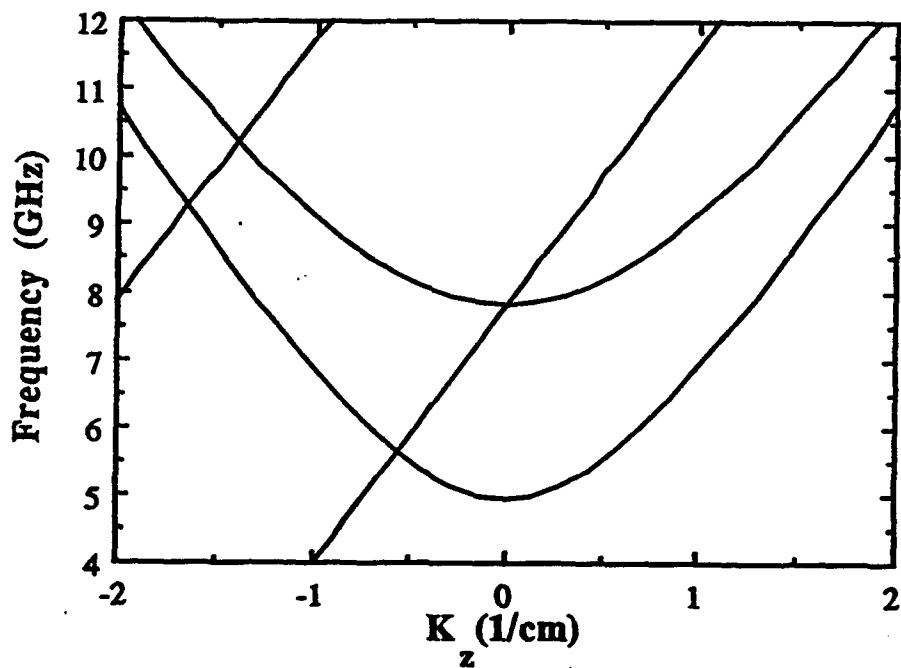


Figure 2) The uncoupled, e-beam-filled cavity dispersion relations illustrating the fundamental ($s=1$) and second ($s=2$) harmonic intersections between the TE_{11} and TE_{21} cavity and e-beam modes. The parameters are: $V_{beam} = 750$ kV; $I_{beam} = 2$ kA, $\alpha = 0.5$; B-field = 6.3 kG.

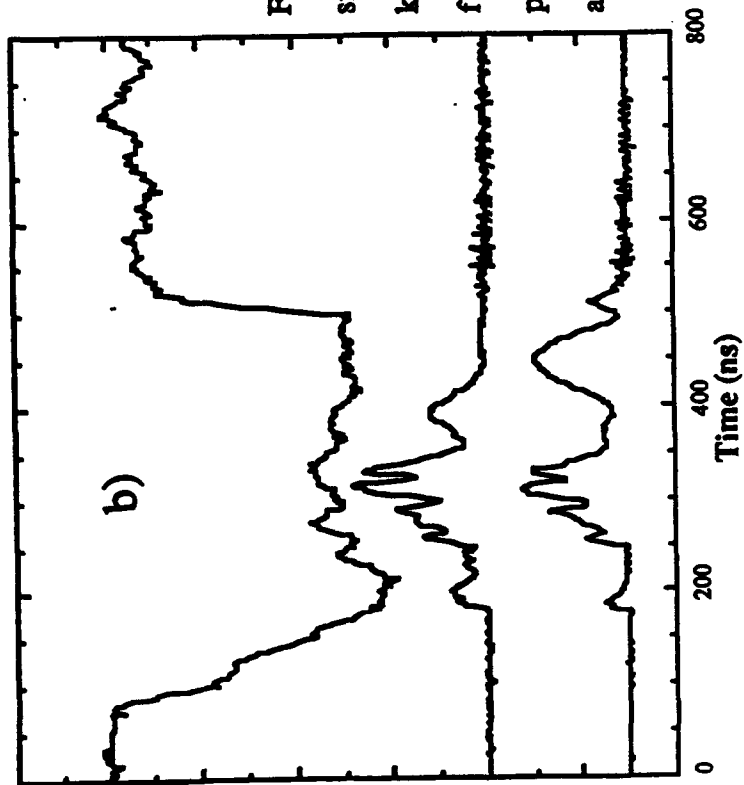
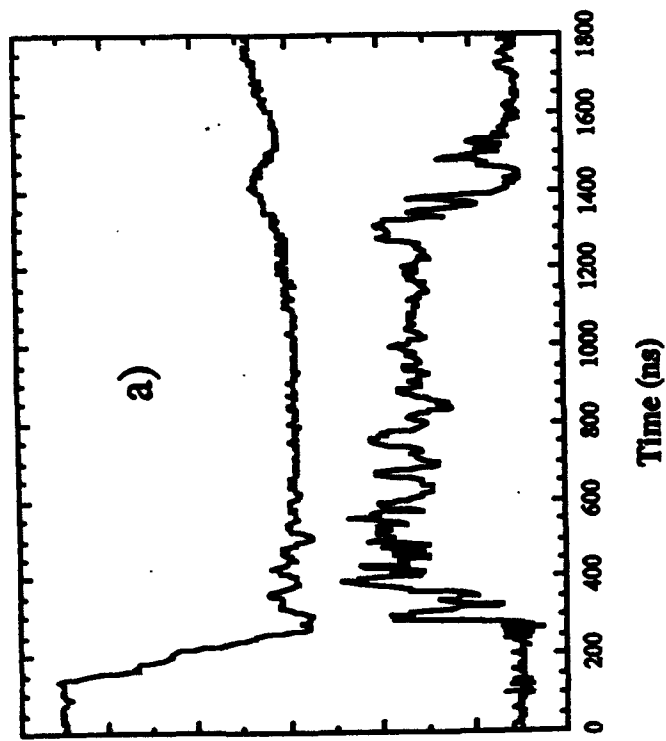


Figure 3) Experimental data signals. (a) top trace: Voltage (310 kV/div); bottom trace: microwave signal, $3.2 \leq f \leq 6.6$ GHz, peak extracted power ~ 120 kW. (b) and (c) top trace: Voltage (310 kV/div); center trace: microwave signal, $3.2 \leq f \leq 6.6$ GHz; bottom trace: microwave signal, $5.3 \leq f \leq 8$ GHz. The center trace in (b) has a signal peak corresponding to ~ 550 kW of extracted power, while the center trace in (c) has a signal peak of ~ 80 kW of extracted power. (a) and (b) are data from the solid e-beam experiments, and (c) is data from the annular e-beam experiments.

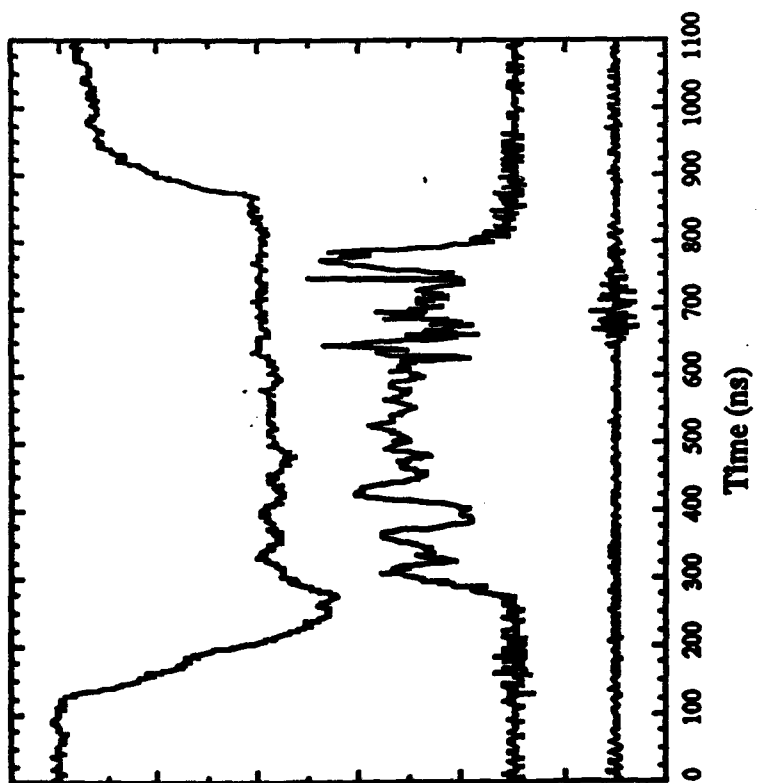


Figure 3c

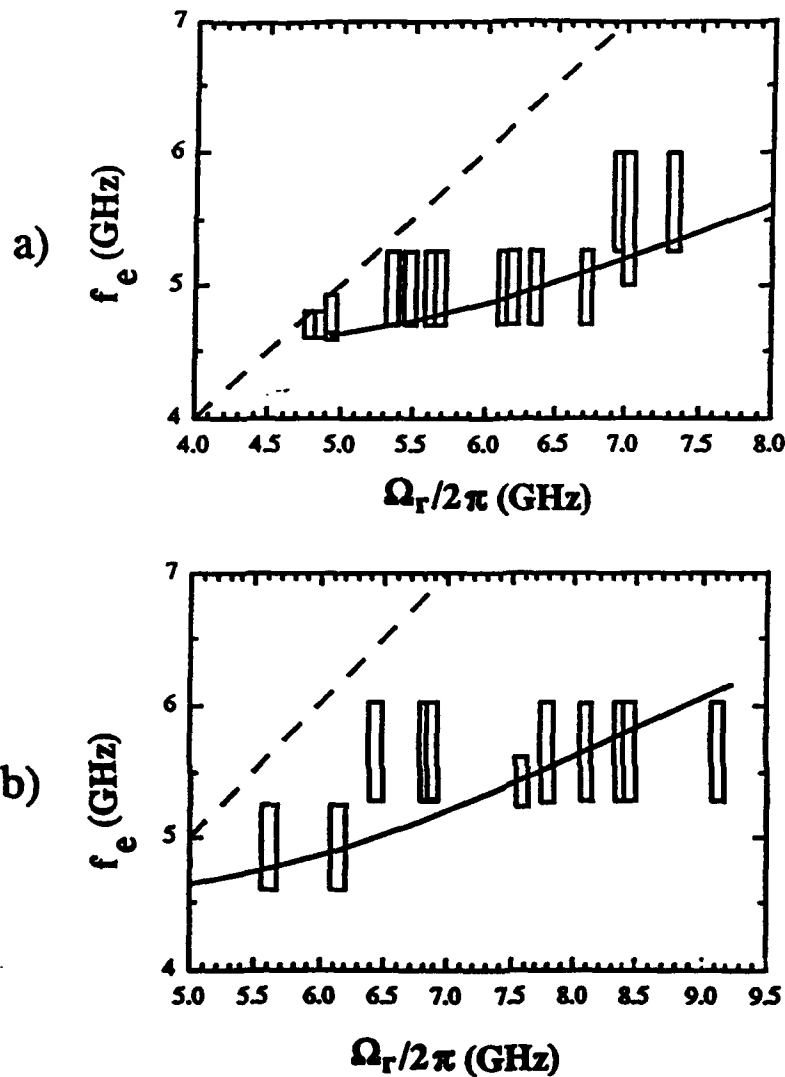


Figure 4) The measured emission frequency as a function of the relativistic cyclotron frequency. The dashed line is the $f_e = \Omega_r/2\pi$ line. (a) is the solid beam data, where the solid line is the theoretical frequency for an uncoupled e-beam-filled dispersion relation for $\alpha = 0.65$, and $I_{\text{beam}} = 1.5$ kA. (b) is the annular beam data, where the solid line is the theoretical frequency for $\alpha = 0.65$ and $I_{\text{beam}} = 300$ A.

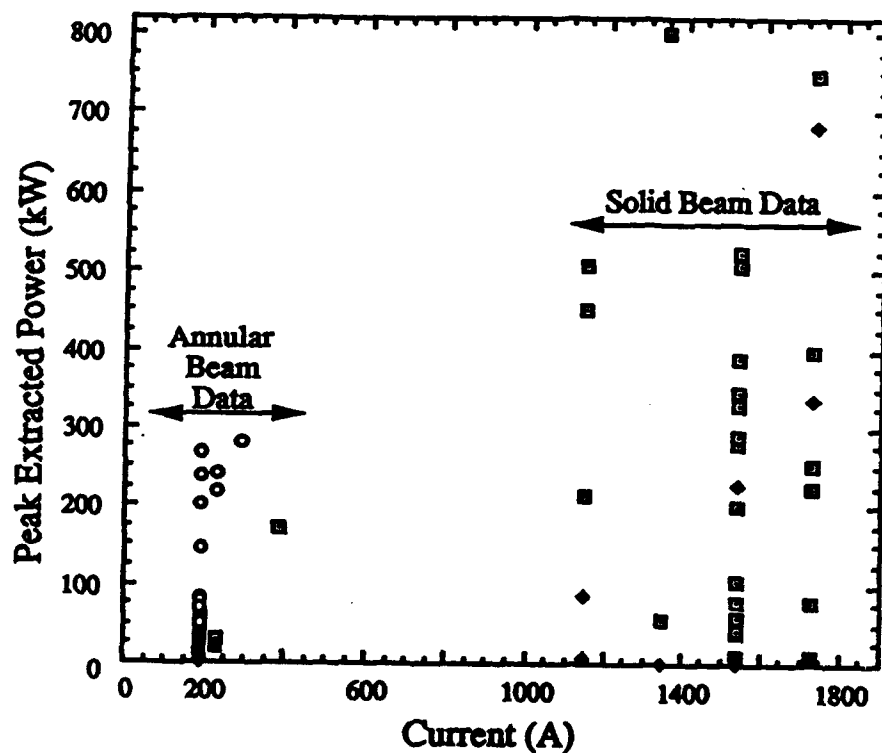


Figure 5). Microwave peak extracted power as a function of the beam current for the annular and solid electron beams. \square are the measured data points where $3.2 \leq f \leq 6.6$ GHz; \blacklozenge are the measured data points where $5.3 \leq f \leq 8$ GHz; and \circ are the measured data points obtained during the initial voltage overshoot where $3.2 \leq f \leq 6.6$ GHz.

Measurement of long-pulse relativistic electron beam perpendicular-to-parallel velocity ratio by Cerenkov emission and radiation darkening on a glass plate

J. J. Choi, R. M. Gilgenbach, T. A. Spencer, P. Menge and C. H. Ching
Intense Energy Beam Interaction Laboratory, Nuclear Engineering Department,
The University of Michigan, Ann Arbor, Michigan 48109-2104

(Received 18 January 1991; accepted for publication 29 October 1991)

We report measurements of the ratio of the perpendicular velocity to the parallel velocity, $\alpha = v_\perp/v_\parallel$, of a relativistic electron beam gyrating in a magnetic field by the use of (1) Cerenkov emission from a glass plate, detected by a gated microchannel plate image intensifier camera, and (2) electron-beam-induced radiation darkening pattern on the same glass plate. The measurements are based on a direct determination of the Larmor radius of an electron beam of known energy. Experiments were performed on a long-pulse electron beam accelerator with ϵ -beam diode parameters: $V_D = 0.6\text{--}0.9$ MV, pulse length = $0.5\text{--}1$ μ s, $I_D = 1\text{--}10$ kA. The experimental value of α agrees with simulation results from particle trajectory codes as well as theoretical predictions from Busch's theorem and adiabatic theory.

I. INTRODUCTION

Relativistic electron beams produced by cold field emission cathodes are important in a number of research areas, such as high-power microwave generation by electron cyclotron resonance masers (CRM),¹ gas laser pumping,² and fusion plasma heating.³ In a CRM, the resonance condition between the ϵ beam and the waveguide mode in a cavity is sensitive to the ratio of the perpendicular velocity to the parallel velocity, $\alpha = v_\perp/v_\parallel$, of the ϵ beam gyrating in an external magnetic field, because the radiated microwave frequency is $\omega = \Omega_e/\gamma + k_\parallel v_\parallel$, where v_\parallel is the axial velocity, Ω_e/γ is relativistic cyclotron frequency, and k_\parallel is the axial wave number of the beam cyclotron mode. Thus, the beam velocity ratio α , ranging from 0.2 to 2 in CRM devices, and its spread are important parameters to accurately measure in such devices.

The transverse electron momentum and its spread have been previously diagnosed by the use of the x-ray radiation pattern.⁴ Cerenkov plates have been utilized elsewhere for emittance measurements.⁵

We describe here a new technique of determining the beam velocity ratio by the use of Cerenkov emission from a glass plate diagnostic with a gated microchannel plate image intensifier camera. The electron beam induced radiation darkening also provides good estimation of the α .

II. THEORY

When an intense beam of electrons moves through a dielectric material, such as a glass plate, at a speed (v) exceeding that of light in the substance, Cerenkov radiation is emitted in a cone of half angle θ , with $\cos \theta = 1/\beta n$, where n is the index of refraction of the dielectric material, β is v/c , and c is the light velocity in free space. The beam for a CRM has a certain pitch angle (typically $10^\circ\text{--}60^\circ$) when entering the glass convertor, so that the Cerenkov cone is tilted as depicted in Fig. 1(a). As the ϵ beam loses its kinetic energy in the medium, the cone angle becomes smaller. Unlike fluorescence or luminescence,⁶ Cerenkov

radiation requires that the beam energy exceed a threshold in order to generate light. The threshold ϵ -beam energy is given as $E_{th} = m_0 c^2 [(1 - n^{-2})^{-1/2} - 1]$, where m_0 is the rest mass. For glass ($n = 1.45$), the cone angle is about 40° for $\beta = 0.9$ and E_{th} is about 190 keV which is well below the typical electron beam energies obtained from most pulsed power ϵ -beam accelerators.

In high current CRMs, the electron beam is produced from an explosive field emission cold cathode in a field immersed diode. The beam is adiabatically compressed as it propagates from the cathode to the interaction region along an increasing externally applied magnetic field, as shown in Fig. 2. During compression, the ϵ beam conserves its canonical angular momentum in an axisymmetric system (Busch's theorem):

$$P_\theta = (m\Omega_e/2)(r_L^2 - r_0^2), \quad (1)$$

where $\Omega_e = eB/m$ is the nonrelativistic cyclotron frequency, r_L is the Larmor radius, and r_0 is the beam guiding center radius. One can relate the Larmor radius of an ϵ beam in the interaction region to the beam radius and the applied magnetic field as

$$r_{L2} = \sqrt{r_2^2 + (B_1/B_2)(r_{L1}^2 - r_1^2)}, \quad (2)$$

where $r_{L1}(r_{L2})$ is the Larmor radius in the diode (in the interaction region), r_1 is the beam radius at the cathode, r_2 is the beam guiding center in the interaction region, and B_1 and B_2 are the external magnetic fields at the cathode and interaction region, respectively. If we know the injected beam energy $\gamma = [1 - (\beta_1^2 + \beta_\perp^2)]^{-1/2}$ and the Larmor radius $r_L = \beta_1 \gamma c / \Omega_e$, where $\beta_1 = v_\parallel/c$ and $\beta_\perp = v_\perp/c$, we can express the beam velocity ratio as

$$\alpha = \frac{\beta_\perp}{\beta_1} = \left(\frac{(\gamma^2 - 1)c^2}{\Omega_e^2 r_L^2} - 1 \right)^{-1/2}, \quad (3)$$

where a monoenergetic electron beam was assumed during the adiabatic compression.

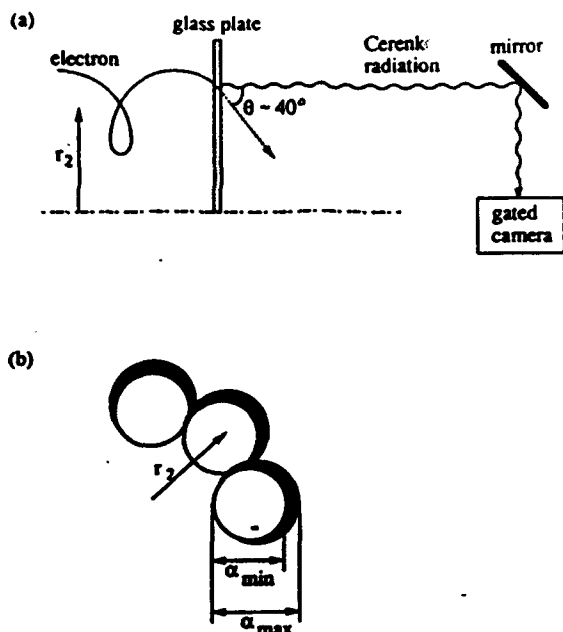


FIG. 1. (a) Schematic of Cerenkov light emission; (b) schematic of electron-beam-induced radiation darkening left on the glass plate.

When the electron beam is adiabatically compressed, the magnetic moment $\mu = mv_1^2/2B$ is invariant. This allows us to write the beam velocity ratio in the interaction region, α_2 in terms of α_1 :

$$\alpha_2 = \left(\frac{1 + \alpha_1^2 B_1}{\alpha_1^2 B_2} - 1 \right)^{-1/2} \quad (4)$$

The spread of axial momentum P_1 and transverse momentum P_2 , is related to the spread of α through

$$\frac{|\Delta P_1|}{P_1} = \frac{|\Delta \alpha|}{\alpha} \frac{\alpha^2}{1 + \alpha^2}$$

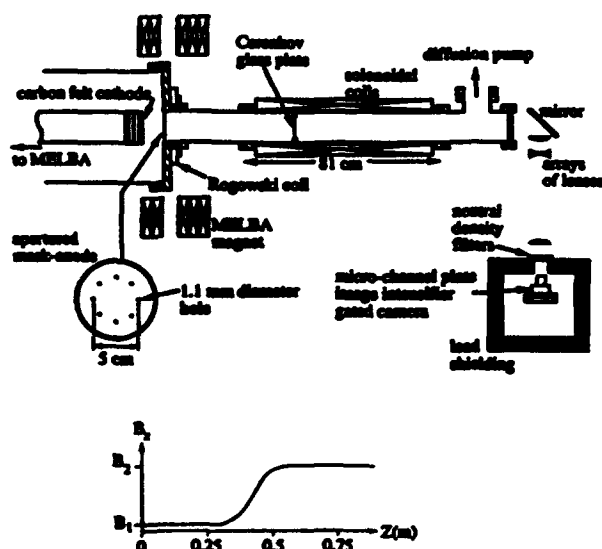


FIG. 2. Upper: experimental configuration for measurements. The Cerenkov glass plate is placed 50 cm away from the mask anode; lower: magnetic fields pulsed from two capacitor banks.

and

$$\frac{|\Delta P_1|}{P_1} = \frac{|\Delta \alpha|}{\alpha} \frac{1}{1 + \alpha^2}$$

because $\Delta P_1 = -\Delta P_2/\alpha$. By taking the derivative of $\gamma_1 = (1 - \beta_1^2)^{-1/2}$, one can derive the axial energy spread as

$$\frac{|\Delta \gamma_1|}{\gamma_1} = \frac{|\Delta P_1|}{P_1} \frac{\beta_1^2}{1 - \beta_1^2}, \quad (6)$$

where ΔP_1 or $\Delta \alpha$ can be estimated from the spread of the Larmor radius. In deriving the equations of the momentum/energy spreads, a monoenergetic electron beam is assumed, or $d\gamma/\gamma = 0$. It should be pointed out that the expression derived for the momentum/energy is only approximate because of the lack of perfectly constant experimental beam energy. However, as will be shown in the section of experimental results, since the beam voltage is very flat, Eqs. (5) and (6) are reasonably appropriate. The diode current does not change rapidly enough that inductive effects on γ need to be considered.

As described in the following section, the beam velocity ratio α can be determined from a direct measurement of the Larmor radius and compared with simulation results from an electrostatic particle trajectory code⁸ and the MAGIC electromagnetic PIC code.⁹

III. EXPERIMENTAL CONFIGURATION

A sketch of the experimental configuration is shown in Fig. 2. A pulsed high-power electron beam was produced by the Michigan Electron Long Beam Accelerator (MELBA)¹⁰ with e -beam parameters $V_D = 0.6-0.9$ MV, pulse length = $0.5-1 \mu s$, $I_D = 1-10$ kA. Cathode voltage is measured using a balanced, water/copper-sulphate resistive divider. The planar cathode is made from carbon felt and has a 7.6 cm diameter with an aluminum shield which covers the edge of the carbon felt cathode. The anode-cathode gap is 6.9 cm. The entire surface of the aluminum cathode except the beam carbon felt emitting area is covered with three coats of glyptal, an electrically insulating enamel. This glyptal coating helps prevent undesired electron field emission from the aluminum. To select a high-quality electron beam from a large area solid beam, we have designed an apertured mask anode (Fig. 2), consisting of eight holes (hole diameter = 0.11 cm) in a 0.32-cm-thick graphite anode plate (POCO graphite, DFP-2). The apertures are equally spaced in a ring of radius 2.52 cm from the center of the anode plate. The ring radius, equal to 2.52 cm, is optimized for the cavity mode and α required for CRM operation. The apertures, which have a diameter of 0.11 cm (which is one-third of the plate thickness), permit only the electron beam with $\alpha < 0.33$ to pass through the anode. Each hole allows about 1 A of electron beam to pass through, measured by a Rogowski coil placed in the flange directly after the mask anode. Current density is estimated at ~ 100 A/cm² which is about the same as that reported by Samlin.¹¹ The magnetic field coils in the diode and uniform region are independently pulsed from two different capacitor banks, with the profile shown in

Fig. 2. It should be pointed out that the electron beam with eight beamlets is not axisymmetric and thus the canonical angular momentum in Eq. (1), P_θ , is not strictly conserved. Therefore, the comparison between our measurements and the Busch's theorem is only approximate.

The Cerenkov convertor is made of slide cover glass (from Kodak, typically Schott type B-270) with a thickness of 0.13 cm. Patterson *et al.*¹² and Downey *et al.*¹³ have shown that glass is an excellent dielectric material as a Cerenkov convertor. A glass plate is chosen because it has several advantages: (1) the glass has an excellent time response to light emission (fast rise time and fast decay time) and a good correlation of light output to electron current density,¹¹ which are important for use with a time-resolved gated camera; (2) electron-beam-induced color change in the glass (radiation darkening) indicates the time-integrated beam pattern; and (3) a glass plate is low cost (slide cover glass) and easy to fashion. To prevent exposure due to the diode plasma light, the side of the glass plate facing the diode was coated with Aerodag, a colloidal carbon spray, until it became opaque. In addition, the carbon coating prevents charge buildup on the glass surface.

The glass plate is located in the uniform field region where the perpendicular velocity of the e beam is maximized by adiabatic compression. The Cerenkov radiation generated is directed by a 90° turning mirror, focused through an array of lenses, and then recorded on a microchannel plate (MCP) camera.¹⁴ The MCP camera is a modified Hasselblad single-lens reflex camera with a microchannel plate, proximity focused on a Polaroid film back with an 80 mm lens. To obtain a time-resolved picture, the light is shuttered by gating the microchannel plate image intensifier by a 40 ns pulse. The timing of the MCP gate is set to sample the Cerenkov light during the flat-top portion of voltage pulse. Neutral density (ND) light attenuation filters (typically, ND = 3–3.1) are placed in front of the MCP camera to avoid overexposure of the photocathode. A lead bunker shields the MCP camera from x rays generated by the e beam.

IV. EXPERIMENTAL RESULTS AND DISCUSSION

Figure 3 represents data from a glass plate exposed to a single shot, 680 kV, 8 A, eight aperture electron beam for over 0.6 μ s pulse length. The externally pulsed magnetic fields are 0.5 kG in the cathode region and 5 kG in the uniform region. The image of the MCP camera shows nearly all beamlets clearly [Fig. 3(a)], indicating a fairly uniform current distribution. As shown in Fig. 3(b), electron-beam-induced radiation darkening was observed in the area subject to the electron beam trajectories. Since the radiation darkening was observed with well-defined color change (brown), we did not have to use a densitometer. The time-integrated beam pattern is a direct measure of the beam Larmor radius in an external magnetic field. Because the MELBA beam voltage is almost flat over 0.6 μ s pulse length, this integrated radiation darkening is a good diagnostic to examine the beam behavior throughout the whole voltage pulse. The reproducibility of such a clear radiation darkening image was excellent as long as the beam voltage

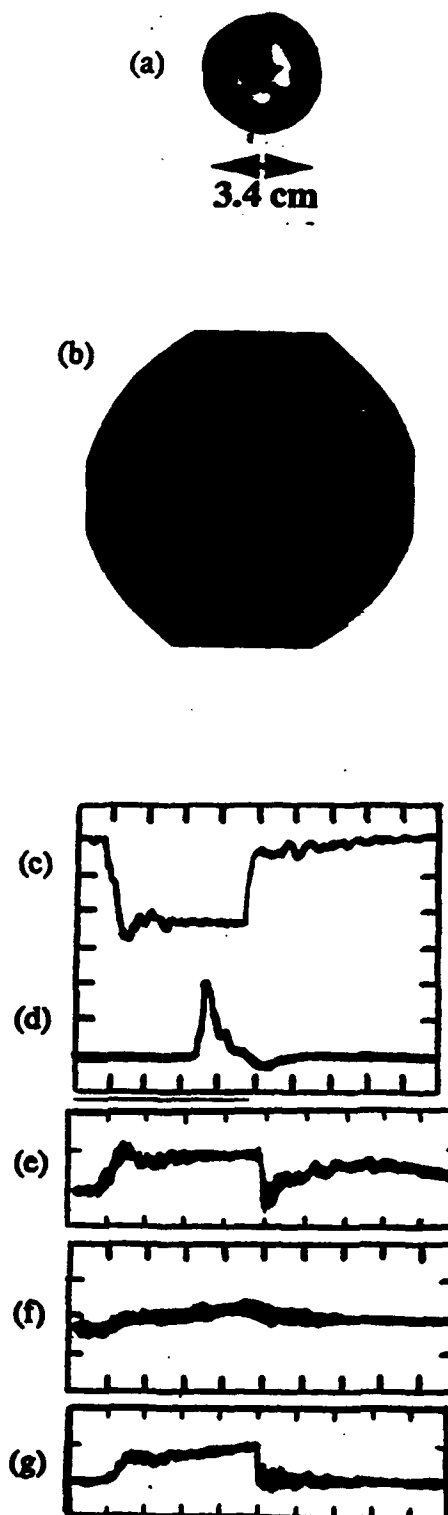


FIG. 3. (a) MCP camera photograph of Cerenkov light, (b) radiation darkening on Cerenkov glass plate, (c) MELBA beam voltage (310 kV/div), (d) gate of MCP camera, (e) cathode stalk current (4.5 kA/div), (f) apertured beam current (40 A/div), and (g) anode current (3.5 kA/div). The magnetic fields are $B_1 = 0.5$ kG and $B_2 = 5$ kG.

was flat over the whole pulse length. The optical density of the pattern was uniform for all eight beamlets. It was observed that the radiation darkening left on the glass faded at room temperature after several months.

Based on the direct visual measurement of the Larmor radius of 0.35 cm from the center of the radiation darkened rings on the glass plate, we determined the beam velocity ratio, α of 0.56 where the beam kinetic energy was 680 kV ($\gamma = 2.33$) during the flat top of the voltage pulse. To compare the data with the theoretical prediction, we measured the beam guiding center radii, $r_1 = 2.52$ cm and $r_2 = 0.9$ cm. The beam velocity ratio directly after the apertured mask anode, $\alpha_1 = 0.16$, was obtained from the computer simulation by MAGIC electromagnetic PIC code.⁹ The emission threshold electric field was assumed to be 20 kV/cm on the fabric emitting surface and 700 kV/cm on the glyptal-coated cathode stalk. A uniform electron emission on the 7.6-cm-diam cathode was assumed. Using Eq. (2) we obtained $r_{L2} = 0.4$ cm, which is consistent with the measured Larmor radius. In addition, the adiabatic theory, as shown in Eq. (4), predicted $\alpha_2 = 0.58$, which is in good agreement with the measured $\alpha_2 = 0.56$. One can interpret the thickness of the radiation darkened rings [Fig. 3(b)] as a spread of the guiding center location because of the "finite" size of the holes and the e -beam perpendicular energy spread. The measured thickness of ~ 1 mm from the radiation darkening allows an estimate of the upper bound in the spread of a Larmor radius of ± 0.5 mm, corresponding to a beam velocity ratio spread of ± 0.05 . The calculated momentum and energy spread from Eqs. (5) and (6) are $\Delta P_{\perp}/P_{\perp} < 4\%$, $\Delta P_{\parallel}/P_{\parallel} < 14\%$, and $\Delta \gamma/\gamma < 7\%$, respectively, indicating that a high-quality e beam with low velocity spread and low axial energy spread is extracted from the apertured mask anode. Note that for a beam with $\alpha < 1$, most of the beam velocity spread comes from the transverse momentum spread, whereas for a beam with $\alpha > 1$, the beam velocity spread is mostly from the axial momentum spread. This is the intrinsic characteristic of an adiabatic magnetic compression of the electron beam, which is seen in Eq. (5).

The Stanford EGUN code⁸ is used for comparison with our α measurement. Figure 4(a) shows the r - z trajectory predicted by the code for a single 680 kV beam from the apertured mask anode which propagates into a grounded cylindrical drift tube in the downstream uniform magnetic field, 5 kG, with the diode magnetic field, $B_1 = 0.5$ kG. Uniform cathode emission was turned on in the code in the region of the fabric cathode. Figure 4(b) shows the predicted α for different diode magnetic fields when B_2 is fixed at 5 kG and B_1 is adjusted from 0.3 to 0.9 kG. When $B_1 = 0.5$ kG, the code predicts the beam velocity ratio, $\alpha_2 = 0.66$, which is in reasonable agreement with the measured $\alpha_2 = 0.56 \pm 0.05$. In addition, the beam guiding center radius after compression is found to be 0.9 cm, which agrees with the measured guiding center, $r_2 = 0.82 \pm 0.25$ cm. Although the EGUN code assumes an axisymmetric system, the comparison between the measurements and code results shows reasonably good agreement. The values of α obtained in the present experiments are consistent with values obtained from frequency measurements of backward wave cyclotron maser microwave emission.

Increasing the magnification factor of the optical lens

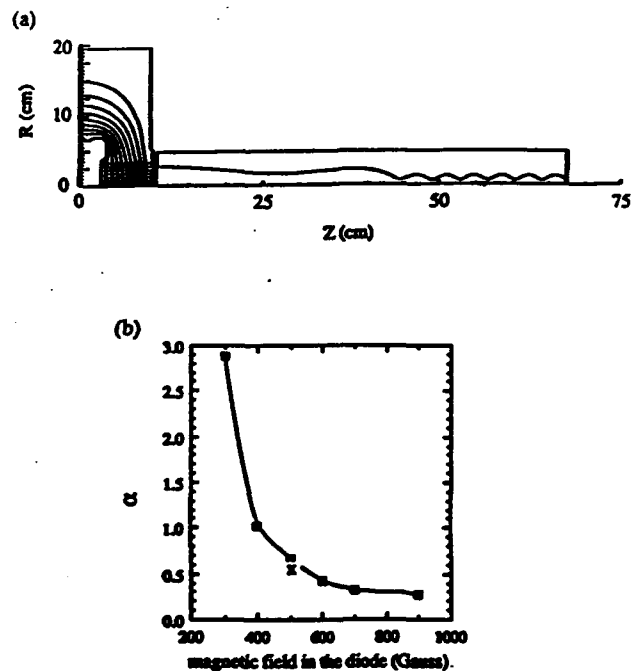


FIG. 4. (a) Electron trajectory plot from Hermansfeldt code (680 kV, $B_1 = 0.5$ kG, $B_2 = 5$ kG); (b) plot of computed beam velocity ratio (\square) vs magnetic field in the cathode region. The experimentally measured α (denoted by \times) is plotted for $B_1 = 0.5$ kG.

array made it possible to see a large image of a Larmor orbit (see Fig. 5). In this shot, we applied the magnetic field of $B_1 = 0.7$ kG and $B_2 = 5$ kG. The beam guiding center radius agreed well with the one directly measured from the radiation darkening although each Larmor orbit from the MCP photograph shows a brightly filled circle, rather than an annular ring. We noticed that the radiation darkening produced a much better image of the Larmor orbit than the MCP photograph. This is because the Cerenkov light emission broadens with a large angular spread as the electrons randomly scatter in the glass convertor. A glass much thinner than an electron range may produce a better time resolved image. Another difficulty in the time-resolved measurements is that the electron-beam-induced radiation darkening reduces the temporal Cerenkov emission by absorption in the glass during the pulse. However, the Cerenkov emission was intense enough so that neutral-density attenuators were still required. It should be noted that there were some other difficulties in gathering data from the MCP camera, such as image focusing on the thin glass convertor, image resolution of the MCP photocathode and adjusting light intensity by the use of neutral density light attenuation filters. Thus we mainly relied on the



FIG. 5. Magnified Larmor orbits from MCP camera photograph. The magnetic fields are $B_1 = 0.7$ kG and $B_2 = 5$ kG.

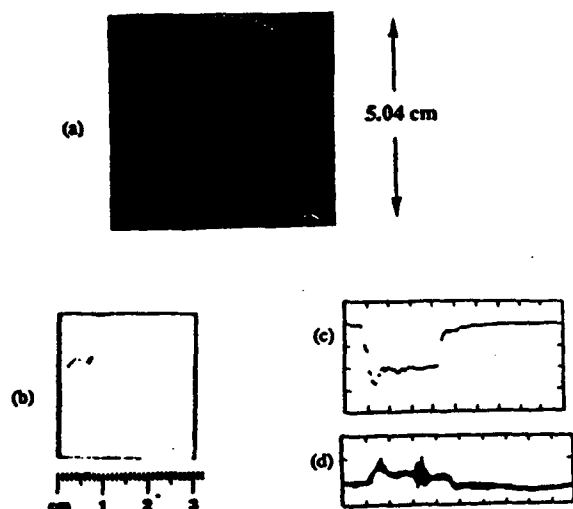


FIG. 6. (a) Apertured mask anode with 80 holes, (b) radiation darkening pattern, (c) beam voltage, and (d) apertured beam current (40 A/div).

radiation darkening pattern in the glass plate, especially when examining the spread of the beam energy and momentum.

Based on the results obtained from the 8-hole apertured mask anode, we fabricated an 80-hole apertured mask anode with the same diameter and hole position from the anode center [see Fig. 6(a)]. A single shot with a 620 kV and 30–50 A electron beam with pulsed magnetic fields $B_1 = 0.5$ kG and $B_2 = 4.7$ kG produced a radiation darkening pattern, as is shown in Fig. 6(b). The observed beam guiding center and Larmor radius are 0.85 cm and 0.35 cm, respectively. Thus the beam velocity ratio is determined to be 0.56. This second apertured mask anode with

known α has been used to perform high-power CRM microwave experiments.¹⁵

ACKNOWLEDGMENTS

This research was supported in part by the Air Force Office of Scientific Research, Air Force Phillips Laboratory, and Los Alamos National Laboratory. We gratefully acknowledge useful discussions with Dr. R. Bosch.

- ¹S. H. Gold, A. W. Fliflet, W. M. Manheimer *et al.*, *Phys. Fluids* 30, 2226 (1987); G. Bekefi, X. DiRienzo, C. Leibovitch, and B. G. Danly, *Appl. Phys. Lett.* 54, 1302 (1989).
- ²L. A. Rosocha and K. B. Riepe, *Fusion Tech.* 11, 576 (1987).
- ³R. M. Gilgenbach, M. E. Read, K. E. Hackett *et al.*, *Phys. Rev. Lett.* 44, 647 (1980); R. M. Gilgenbach, M. E. Read, K. E. Hackett *et al.*, *Nucl. Fusion* 21, 319 (1981).
- ⁴S. Talmadge, T. C. Marshall, and S. P. Schlesinger, *Phys. Fluids* 20, 974 (1977).
- ⁵G. Bekefi, F. Hartemann, and D. A. Kirkpatrick, *J. Appl. Phys.* 62, 1564 (1987).
- ⁶V. I. Kremensov, P. S. Strelkov, and A. G. Shkvarunets, *Sov. Phys. Tech. Phys.* 25, xx (1980).
- ⁷C. Kyler and K. R. Chu, *Naval Research Lab. Memorandum Report* 4401, 1981.
- ⁸W. B. Herrmannsfeldt, SLAC-226, November, 1979.
- ⁹B. Goplen, L. Ludeking, J. McDonald, G. Warren, and R. Worl, *MAGIC User's Manual* (Mission Research Corporation, Newington, 1989).
- ¹⁰R. M. Gilgenbach, L. D. Horton, R. F. Lucey, S. Bidwell, M. Cuneo, J. Miller, and L. Smutek, *Proc. 5th IEEE Pulsed Power Conference*, June 10–12, 1985, p. 126.
- ¹¹G. E. Samlin, *J. Appl. Phys.* 62, 2169 (1987).
- ¹²E. L. Patterson, R. A. Hamil, and G. E. Samlin, *J. Appl. Phys.* 54, 515 (1983).
- ¹³S. W. Downey, L. A. Buita, R. L. Carlson, S. J. Czuchlewski, and D. C. Moir, *J. Appl. Phys.* 60, 3460 (1986).
- ¹⁴S. Hanver, R. E. Pechacek, J. R. Greig, D. P. Murphy, and M. Raleigh, *Naval Research Lab. Memorandum Report* 5702, 1985.
- ¹⁵J. J. Choi, R. M. Gilgenbach, and T. A. Spencer, *Proc. of 15th International Conference on Infrared & MM Waves*, SPIE 1514, 143 (1990).

Article accepted for publication in
International Journal of Electronics,
7th Special Issue on Gyrotrons

**Mode competition in Bragg resonator cyclotron resonance maser
experiments driven by a microsecond, intense electron beam accelerator**

J. J. Choi*, R. M. Gilgenbach, and T. A. Spencer

Intense Electron Beam Laboratory, Department of Nuclear Engineering, University of
Michigan, Ann Arbor, MI 48109

Abstract

We report an experimental study on mode competition in an high-Q Bragg resonator cyclotron resonance maser (CRM) employing a microsecond, relativistic electron beam. The high quality annular electron beam of 20 - 80 amps was produced through an apertured mask-anode. The high-Q Bragg resonator was designed to excite the TE_{31} mode CARM oscillation at 18.9 GHz. Two configurations of Bragg resonators were used; with ripples half-inward and with ripples fully-outward with respect to a smooth tubular center section. Bragg resonator microwave emission was compared to radiation emitted when the electron beam interacted with smooth tubes with the same diameter as the Bragg resonator center sections. In the present Bragg resonator CRM experiments, three parasitic oscillations were the most serious competing modes, apparently suppressing the TE_{31} CARM oscillation: TE_{21} absolute instability, TE_{11} gyro-BWO, second and third harmonic TE_{51} mode. When a high current annular beam of 150 - 200 amps was injected in the Bragg resonator, we observed the TE_{21} absolute instability at $B \geq 6.9$ kG, and a TE_{11} gyro-BWO interaction at $B \leq 5.2$ kG. Experimental evidence on the modes of the absolute instabilities were provided by gas breakdown patterns in fluorescent light tubes and frequency measurements.

* present address: Science Applications International Corp., McLean, VA 22102

1. Introduction

The cyclotron resonance maser (CRM) has proven to be attractive for many high power microwave applications such as fusion plasma heating (Gilgenbach et al. 1980), radar/communications, and high gradient RF accelerators (Granatstein 1987). The CRM radiation mechanism depends on the relativistic mass effect of electron cyclotron motion and the azimuthal bunching of gyrating electron beams in a static magnetic field. In the CRM resonance where a beam cyclotron mode, $\omega = s \Omega_e / \gamma + k_{\parallel} v_{\parallel}$, is synchronized in phase with an electromagnetic waveguide mode in a cavity, $\omega^2 = \omega_{co}^2 + (k_{\perp} c)^2$, there are, in general, two resonance points; the downshifted interaction and the Doppler upshifted interaction. Here, Ω_e / γ is the relativistic cyclotron frequency, s is the harmonic number, v_{\parallel} is the electron axial velocity, k_{\parallel} is the axial wavenumber, ω_{co} is the wave cutoff frequency, and c is the speed of light. The gyrotron is operated at the near grazing incidence and has been proven to be an efficient radiation source (Granatstein 1987). The operation of the cyclotron autoresonance maser (CARM) (Fliflet 1986) relies on a dominant Doppler upshifted interaction. During the beam and electromagnetic wave interaction in the CARM, the electron energy loss is balanced with a change of electron axial momentum and thus the detuning of the CRM resonance is automatically reduced. Because of the large Doppler upshifted conversion, the CARM radiation frequency is far above the waveguide cutoff frequencies and far higher than the gyrotron radiation frequency for the same magnetic field. One of the major differences of the CARM from the gyrotron devices is that the CARM radiation originates from axial bunching as well as azimuthal bunching and thus the radiation conversion efficiency is expected to be high. However, since the CARM interaction occurs when the wave phase velocity is close to the speed of light the radiation conversion efficiency is sensitive to beam velocity/energy spreads.

The CARM device has been an attractive alternative to gyrotrons since the first theoretical work (Bratman et al. 1981) was published and, in the following year,

experimental results (Botvinnik et al. 1982 a and 1982 b) were reported. The first CARM experiment (Bekefi et al. 1989) in the US, a 35 GHz CARM amplifier at MIT, produced 10 MW (3 % efficiency) from a 1.5 MeV, 260 A electron beam with energy spread of less than 2 %. However, for CARM operation as an oscillator, selective high frequency external feedback is required in order to start cavity mode oscillation; otherwise, a higher beam current would be required for startup of the CARM oscillation than that required for the gyrotron. A series of periodic corrugations of the waveguide surface provides reflection of the wave when the corrugation period is such that the radiation reflected from each of the corrugations is in coherent phase. With an appropriate choice of corrugation periods, the rippled section becomes highly reflective and is known as a Bragg resonator (McCowan et al. 1988). Bragg resonator CARM experiments are underway at several laboratories in the US (Danly 1990 and Chong et al. 1991).

Most of the previous CRM experiments with MV electron beams have been conducted with short ($< 0.1 \mu\text{sec}$) pulses. The present work contains the first comprehensive experimental study on mode competition in an high-Q Bragg resonator CRM employing a microsecond, relativistic (relativistic factor, $\gamma = 2.37$) electron beam.

2. Experimental configuration

The experimental configuration is depicted in Figure 1. The experiments on Bragg resonator CRMs have been performed on the Michigan Electron Long Beam Accelerator (MELBA) (Gilgenbach et al. 1985) with e-beam parameters: $V_{\text{peak}} = 0.8 - 0.9 \text{ MeV}$, diode currents of 1 - 50 kA and pulselength between $0.5 \mu\text{sec}$ and $4 \mu\text{sec}$. The planar cathode is made from carbon felt or velveteen and has a 7.6 cm diameter with an aluminum shield which covers the edge of the fabric cathode. The anode-cathode gap is 6.9 cm. The entire surface of the aluminum cathode and cathode stalk except the beam emitting area is covered with three coats of glyptal (Glyptal 1201-A Red Insulating Enamel, manufactured by Glyptal Inc., Chelsea, MA), an electrically insulating enamel.

This glyptal coating helps prevent the aluminum from undesired electron field emission. Cathode stalk current is measured by a B dot loop, anode current is measured using current transformers (Pearson Electronics 110A, manufactured by Pearson Electronics Inc., Palo Alto, CA) on four low-inductance current return paths, and transported beam current is measured by a Rogowski coil placed in the flange directly after the anode. Large pulsed magnetic field coils were utilized to magnetize the diode region to 0.4 - 1 kG. Cavity magnetic field coils were wound on the beam tube and can be pulsed up to 11 kG. The diode and cavity magnetic fields were driven by separate capacitor banks to control the adiabatic compression of the beam.

Apertured mask-anodes have been developed to produce a high quality annular electron beam of 20 - 80 amps with low velocity/energy spread. The low-emittance apertured mask-anode consists of 80 holes (hole diameter = 0.11 cm) in a 0.32 cm thick graphite plate, equally spaced in a ring of radius 2.52 cm from the center of the anode plate (see Figure 2(a)). The aperture size, which is one third of the plate thickness, is chosen so that each hole allows about 1 ampere of electron beam current to pass through the anode.

One of the major advantages of the apertured mask-anode is that we can control the e-beam current by the number of the apertures or the size of the apertures without changing any diode conditions. In the second set of high-Q Bragg resonator experiments, the growth of gyrotron radiation was examined by increasing the electron beam current and beam energy spread in the interaction region. An apertured mask-anode with 24 holes (diameter = 0.45 cm) was fabricated to inject an e-beam current of 150 - 200 amps into the high-Q Bragg resonator. As shown in Figure 2(b), the ring radius of the 24 holes is 2.52 cm, which is the same as that of the 80 hole apertured mask-anode, so that the beam velocity ratio remains unchanged. Although the beam quality is degraded due to the large spread of e-beam energy and momentum, gyrotron performance is not as sensitive to the beam temperature as the CARM because the resonance condition for the gyrotron occurs near the cutoff frequencies of TE waveguide modes.

The high-Q sinusoidal Bragg resonator was designed and constructed to excite the high frequency CARM oscillation of the TE_{31} cylindrical cavity mode at 18.9 GHz. The Bragg reflector consists of a sinusoidal corrugation of period 0.95 cm and amplitude ± 0.16 cm machined in an aluminum tube. Two 15-period Bragg reflectors were fabricated for upstream and downstream locations, separated by a 29.4 cm straight copper section. Bragg resonator parameters are summarized in Table 1. Cold test measurements were performed using an HP-8510 Vector Network Analyzer to characterize the Bragg resonator. Figure 3 depicts a configuration of the Bragg resonator cold test setup. A TE_{31} mode convertor was made of a cylindrical tube wrapped by a rectangular waveguide with three equally spaced coupling holes. The spacing of the three coupling holes was set to be $n\lambda_g = \pi D$ where n is the azimuthal mode number of the TE_{31} mode (in this case, $n = 3$), λ_g is the guided wavelength in the rectangular waveguide, and D is the diameter of the cylindrical tube. By measuring reflectivities of the upstream and downstream Bragg reflectors, the diffraction Q of the TE_{31} Bragg mode was determined to be $Q_{\text{diff}} = k^2 L / (k_H (1 - R_1 R_2)) = 16,600$ where k is the wave number, L is the cavity length, and R_1 and R_2 are the upstream and downstream reflectivities respectively. Reflectivity measurements of a single Bragg reflector show good agreement compared with the prediction from uncoupled single mode theory (McCowan et al. 1988) for the TE_{11} , TM_{01} , TE_{31} Bragg resonant modes as shown in Table 2. The Q measurement by transmitted power was found to be equivalent to measuring Q by reflected power using a TE_{31} mode convertor (Sucher 1963). Using two identical TE_{31} mode convertors, we measured a total Q of 4700 at 18.93 cm where the total Q is the ratio of the resonant frequency to the frequency difference of half power frequencies, as a conventional method of Q measurements (Fliflet et al. 1981 and Denisov et al. 1983). The total Q was measured by injecting power through the mode convertor in the side of the straight section cavity and by sampling the output power from the other mode convertor in the other side of the straight section cavity. From $1/Q_{\text{total}} = 1/Q_{\text{diff}} + 1/Q_{\text{ohmic}}$, the ohmic Q of the

Bragg resonator is determined to be 6600. The ohmic Q was confirmed by a direct measurement where the open ends of the upstream and downstream Bragg reflectors were closed with copper plates in order to measure the power dissipation through the ohmic loss only.

Using the 80 hole apertured mask-anode, experiments were performed with 2 different configurations of Bragg resonators (see Figure 4) for comparison with smooth tubes:

1) Bragg resonator with ripples half inward (BRHI);

The 1.93 cm radius of the straight section cavity placed in between the two identical Bragg reflectors is chosen such that all the ripples are half inward with respect to the inner surface of the straight section cavity.

2) To compare with the Bragg resonator BRHI results, we replaced the whole interaction region by a 58.5 cm long smooth tube without Bragg resonator. The radius of the smooth tube is 1.93 cm, which is the same as that of the straight section cavity in the Bragg resonator BRHI.

3) Bragg resonator with ripples fully outward (BRFO);

These experiments utilized the same two Bragg reflectors as those of the Bragg resonator BRHI. However, in this case, the radius of the straight section cavity, 1.64 cm, was smaller than that of Bragg resonator BRHI, so that all the ripples are now fully outward.

4) In order to compare with Bragg resonator BRFO results, the Bragg resonator BRFO was replaced by a 58.5 cm long smooth copper tube with radius of 1.64 cm.

A 2° tapered conical horn was attached to the downstream Bragg reflector to reduce output mode conversion. At the output window, one or two K-band (WR-42, cutoff frequency = 14.05 GHz) open waveguides were positioned to scan the high frequency ($f > 14.05$ GHz) field pattern of either $|E_r|^2$ or $|E_\phi|^2$. Microwave emission was launched into a stainless steel tank lined with microwave absorber, in which S-band

(WR-284, cutoff frequency = 2.1 GHz) open waveguide and an X-band standard gain horn were mounted on-axis and off-axis (polar angle = 15°) respectively at the distance of 72 cm (which satisfies $R \geq 2D^2/\lambda$ where D is the diameter of the output window and λ is the radiation wavelength) from the output window for far-field measurements of low frequency radiation. The sampled microwaves were guided through a 20 meter long S-band waveguide or either of two 15 meter long X-band (WR-90, cutoff frequency = 6.6 GHz) waveguides to the Faraday cage.

Commercially available lowpass filters were used to make wide-range bandpass filter channels together with standard rectangular waveguides. A series of cylindrical cavity resonators (Choi 1991 a) were used to diagnose narrow bandpass radiation frequencies especially near cavity mode cutoff frequencies. These cavities had the benefit of adjusting one filter over a wide range of resonant frequencies by the use of a tuning screw mounted on the cavity.

The total radiated power from the cavity was measured from the waveguide directional couplers, variable/fixed attenuators and diode detectors. All the microwave measurement components were absolutely calibrated in the fundamental mode bands. We have calibrated the power fraction transmitted from the radiating output window to the receiving horns in the microwave diagnostic chamber using a microwave sweep source. Microwave power attenuation in the X-band and S-band waveguide connecting the microwave diagnostic chamber to the Faraday cage was also included.

Microwave breakdown experiments with fluorescent light tubes were performed for mode identification. Eight tubes (GE-F4T5/CW) were vertically positioned at 5 cm away from the lucite vacuum window. An open shutter camera with polaroid film back (Polaroid, Type 57, ASA 3000) was mounted on the side port of the microwave diagnostic chamber with a large mirror set at 45° to reflect the fluorescent tube image into the camera. A black plastic cover was placed between the vacuum window and the fluorescent light tubes in order to block any light other than the microwave breakdown in

the fluorescent light tubes. Cold tests were performed using a commercial magnetron (EPSCO, 5 kW, 0.3 - 50 μ sec) to determine a breakdown threshold in the fluorescent light tubes. Photographs were taken with the same film and the same setup as the experiments. However, the photographs revealed no breakdown. This could be due to the relatively low power of the calibration source not generating as bright a plasma in the tube.

3. Electron beam characterization

For the measurement of the beam velocity ratio, $\alpha = v_{\perp}/v_{\parallel}$, we fabricated an 8-hole apertured mask-anode with the same hole size and major radius as the 80 hole apertured mask-anode. A glass plate diagnostic (Choi et al. 1991 b) was utilized to determine the beam velocity ratio α by single-shot radiation darkening of the glass and by Cerenkov emission detected with a gated microchannel plate (MCP) image intensifier camera. Because of image resolution limitations of the MCP photocathode, the radiation darkening pattern on the glass was mainly used in determining electron beam velocity ratios and velocity/energy spreads.

Figure 5 shows data of the electron beam characterization. The Cerenkov glass plate was exposed to a single pulse of a 680 kV, 8 amp electron beam. Notice that the beam voltage is almost flat over the whole 0.6 μ sec pulselength. The image of the microchannel plate (MCP) image intensifier camera (which was exposed for 40 nsec) showed almost all beamlets clearly, indicating a uniform current distribution. Electron beam induced radiation darkening of the glass was measured in the area subject to the electron beam orbits. Since this time integrated beam pattern is a direct measure of the beam Larmor radius (0.35 cm) for a fully phase-mixed beam, we determined the beam velocity ratio, $\alpha = 0.56$. In addition, from the measured thickness (~ 1 mm) of the beam orbits, the velocity/energy spreads were estimated to be $\Delta v_{\parallel}/v_{\parallel} \sim 4\%$ and $\Delta \gamma/\gamma \sim 7\%$,

indicating that a high quality e-beam with low velocity spread and low axial energy spread was extracted from the apertured mask-anode with 0.11 cm diameter holes.

4. Experimental results

4.1. High-Q Bragg resonator CRM experiments with high quality electron beam

4.1.1. *Bragg resonator with ripples half inward (BRHI)*

Figure 6 shows the uncoupled dispersion relations of the original design to excite the TE₃₁ CARM mode. The measured beam velocity ratio, $\alpha = 0.5 \pm 0.05$, was achieved by pulsing the diode magnetic field to ~ 0.7 kG and the cavity magnetic field to ~ 5 kG. This device was designed for the beam cyclotron mode to be at grazing incidence with the TE₃₁ Bragg mode. The choice of the cavity magnetic field of 5 kG was made in order to avoid a TE₂₁ absolute instability with the beam current of 20 - 80 amps (the critical current for this absolute instability (Davies et al. 1990) was calculated to be 60 amps).

For the cavity magnetic field of 4.6 - 5.7 kG, the Bragg resonator BRHI generated a high frequency ($f > 14.05$ GHz) peak power of about 1 MW; with the smooth tube without the Bragg reflectors, the peak power was reduced to about 0.3 MW. Overall, the Bragg resonator produced more microwave power by ~ 6 dB than the smooth tube at the cavity magnetic field of 4.6 to 5.7 kG. From the frequency measurement, we found that most of the high power microwave emission in the high frequency band ($f > 14.05$ GHz) was not in the 18.7 - 19.2 GHz band which includes the TE₃₁ Bragg mode, but originated from the second or third harmonic gyrotron interaction near the TE₅₁ cutoff frequency.

With the Bragg resonator operated at the cavity magnetic field of 4.6 - 5.7 kG and the diode magnetic field of 0.7 kG, we have observed efficient, megawatt level microwave emission in the 2.1 - 6.6 GHz band during the voltage flat-top (typically, ~ 680 kV). Figure 7 shows a scan of peak power in the 2.1 - 6.6 GHz band (which includes the TE₁₁ gyrotron backward wave oscillation, gyro-BWO (Park et al. 1990)) as a function of cavity magnetic fields for the case of Bragg resonator BRHI and smooth tube without Bragg

reflectors. Clearly, the Bragg resonator BRHI produces more peak power in the 2.1 - 6.6 GHz band by > 10 dB than the smooth tube without Bragg reflectors. Apparently, the Bragg resonator BRHI gives some external feedback into the gyro-BWO interaction due to the impedance mismatch from the ripples half-inward even in the region of non-Bragg resonance conditions. It is interesting to notice that the microwave signal in the 2.1 - 6.6 GHz band which includes the TE₁₁ gyro-BWO completely disappeared at the cavity magnetic field above 6.2 kG. To see the dependence of microwave emission on the beam velocity ratio, α , we changed the diode magnetic field ranging from 0.4 kG to 0.8 kG while the cavity magnetic field was kept at 6.35 - 6.53 kG. No high power emission was detected in the 2.1 - 6.6 GHz band during the voltage flat-top.

In the second experiment operating with the cavity magnetic field of ~ 6.4 kG in order to avoid the mode competition with the TE₁₁ gyro-BWO, the beam velocity ratio, α , should be adjusted because we want to keep the beam-wave phase synchronism at the Bragg resonance condition, $k_{||} = \pi/L_c = 3.3 \text{ cm}^{-1}$ where L_c is the corrugation period of the Bragg reflector. The required $\alpha = 0.69 - 0.79$ is achieved by lowering the diode magnetic field to 0.4 kG and increasing the magnetic compression ratio to 16. In this high cavity magnetic field, however, harmonic gyrotron interactions near cutoff frequencies remain as a source of mode competition with the TE₃₁ Bragg mode in our Bragg resonator BRHI.

Waveforms of the voltage and microwave emission are presented in Figure 8 for the case of the Bragg resonator (BRHI) and the smooth tube without Bragg reflectors. For the case of the Bragg resonator with ripples half-inward, the peak power in the 18.7 - 19.2 GHz band is only a small fraction (~ 15 dB) of the power in the high frequency band ($f > 14.05$ GHz) where the cavity magnetic field and diode magnetic field are 6.4 kG and 0.4 kG respectively. This indicates that most of the power in the high frequency band ($f > 14.05$ GHz) is in modes other than the TE₃₁ CARM mode. Frequency measurement, using a series of cavity resonator bandpass filters, identifies the highest power in the $f >$

14.05 GHz band to be from the second harmonic gyrotron interaction near a TE_{51} waveguide cutoff.

For the case of the smooth tube without Bragg reflectors, all of the power (~ 0.3 MW) in the high frequency band ($f > 14.05$ GHz) appears in the 18.7 - 19.2 GHz band: these data are directly compared with the Bragg resonator case in Figure 8. To identify the radiation mode we repeated the experiment to measure the near-field radiation pattern of on-axis and off-axis $|E_r|^2$ on the output window. Radial position of the off-axis K-band open waveguide was positioned at $r = 0.78 r_g$ where r_g is the radius of the output window, 4.85cm. Experimental evidence of the second harmonic TE_{61} gyrotron mode is provided by higher off-axis power of the $|E_r|^2$ -component by 23 dB than on-axis power. High power microwave radiation from harmonic gyrotron oscillations near cutoff frequencies of the higher order modes is explained by theoretical predictions: (1) the gyrotron starting current is low due to the high diffraction Q at the frequency near the TE_{61} cutoff, and (2) the gyrotron interaction is relatively insensitive to the beam temperature. Second harmonic emission (TE_{21}) may also explain the high power, high frequency radiation previously attributed to the CARM in the paper by Wang et al. (1989).

4.1.2. *Bragg resonator with ripples fully outward (BRFO)*

Figure 9 shows the coupling strength (Palmer 1987) of TE waveguide modes in a corrugation surface versus the resonant frequencies of Bragg modes. A mode, such as the TE_{01} , which has a zero azimuthal mode number and a maximum electric field far away from the corrugated surface, cannot couple strongly with the Bragg reflector. The low coupling strength of the TE_{01} mode is associated with low Q, resulting in high starting current. Therefore, the TE_{01} mode is not expected to be a competing mode in our TE_{31} CARM operation, although the Bragg resonant frequency of the TE_{01} mode is very close to that of the TE_{31} . On the other hand, the TE_{41} Bragg mode appears to be a competing mode because of even higher coupling strength with corrugations than the TE_{31} design

mode. However, noticing that there is a relatively large frequency separation of about 1.7 GHz between the TE_{31} and TE_{41} modes, we can avoid mode overlapping by finely adjusting the beam cyclotron line with a low axial velocity spread.

Compared with the case of Bragg resonator BRH1, the beam-wave coupling strength (Gold et al. 1985) in the straight section cavity of the TE_{31} mode for BRFO is expected to be high because the reduction of the straight section cavity radius makes the measured beam guiding center, $r_0 \sim 0.9$ cm, relatively close to the peak of the TE_{31} electric field strength. The coupling strength with the beam position in the straight section cavity is depicted in Figure 10. Notice that the TE_{21} mode has high coupling with the e-beam and is expected to exhibit strong mode competition.

Figure 11 presents waveforms for the Bragg resonator case (ripples fully-outward). As shown in Figure 11, most of the power in the high frequency band ($f > 14.05$ GHz) appears to be in the 18.7 - 19.2 GHz band (which includes the TE_{31} Bragg resonant frequency) or 19.2 - 19.7 GHz band. However, the 18.7- 19.2 GHz and 19.2 - 19.7 GHz bandpass filtered channels also include other high harmonic interactions such as the second harmonic TE_{51} gyrotron interaction and the third harmonic TE_{51} absolute instability interaction. We cannot rule out the possibility of such harmonic CRM interactions, particularly when an instability is absolutely unstable. The starting currents (Bratman et al. 1981 and Fliflet 1986) of the TE_{31} CARM and the TE_{51} ($s = 2$) gyrotron mode are 2 amps and 6 amps, which are below the injected beam current. The temporal growth rates (Davies et al. 1990) of TE_{31} ($s = 1$) CARM, TE_{51} ($s = 2$), TE_{51} ($s = 3$) are calculated to be $0.26 \times 10^9 \text{ sec}^{-1}$, $0.25 \times 10^9 \text{ sec}^{-1}$, and $0.3 \times 10^9 \text{ sec}^{-1}$ respectively. The growth rate of the third harmonic TE_{51} gyro-BWO is the highest among the three CRM interactions. Theory (Davies et al. 1990) predicts that the second harmonic TE_{51} gyrotron interaction is not an absolute instability for our beam parameters. Based on the theoretical investigation of growth rates and starting currents, it is concluded that the microwave

emission in the 18.7 - 19.2 GHz or 19.2 - 19.7 GHz band from the Bragg resonator BRFO is from the third harmonic TE_{51} absolute instability rather than the CARM.

In order to compare with the Bragg resonator BRFO, we placed a 58.5 cm long smooth tube without Bragg resonator in our interaction circuit. The overall power (~ 0.2 MW) for the case of the Bragg resonator BRFO is usually higher than that for the smooth tube case without Bragg reflectors. The difference between the Bragg resonator BRFO and the smooth tube without Bragg reflectors lies in the observed frequency; for the case of the smooth tube, the high frequency band ($f > 14.05$ GHz) microwave emission is mostly in the 15.5 - 16 GHz frequency band rather than in the 18.7 - 19.2 GHz band or 19.2 - 19.7 GHz band. The frequency band of 15.5 - 16 GHz includes the second harmonic TE_{41} absolute instability.

In the Ka-band (WR-28, cutoff frequency = 21.1 GHz) highpass waveguide channel, no microwave emission was detected for the cases of both the Bragg resonator BRFO and the small diameter smooth tube without Bragg reflectors, suggesting that there is no major instability in high order TE_{nm} ($n \geq 4$) Bragg modes with high harmonics. In addition, the experimental results confirm that there is no significant growth of CRM instabilities in high ($s \geq 4$) harmonic gyrotron interactions.

Figure 12 shows a scan of peak microwave power in the 2.1 - 6.6 GHz band versus cavity magnetic field for the case of the Bragg resonator BRFO and the smooth tube without Bragg reflectors. For the cavity magnetic field ranging from 6.1 kG to 6.35 kG, the small diameter ($r_w = 1.64$ cm) smooth tube without Bragg reflectors produced microwave emission in the 2.1 - 6.6 GHz band with peak power of ~ 1 MW, which is believed to originate from the TE_{11} gyro-BWO interaction. For the Bragg resonator BRFO, however, we did not observe high power microwave emission in the 2.1 - 6.6 GHz band. This could be explained by the fact that the Bragg resonator configuration with ripples fully-outward provides no low frequency feedback into the interaction region,

in contrast to the Bragg resonator with ripples half-inward. Thus, the TE_{11} gyro-BWO is not a major competing mode in the Bragg resonator BRFO experiments.

We have detected microwave emission in the 6.6 - 10 GHz frequency band at the cavity magnetic field of $B \geq 5.92$ kG, which includes the fundamental TE_{21} downshifted interaction. Theory (Davies et al. 1990) predicts that the critical current of the onset of the TE_{21} absolute instability is 3 amps at 8.9 GHz where $V = 560$ kV, $\alpha = 0.63$, $B = 6.15$ kG are assumed, suggesting that the TE_{21} downshifted interaction is the absolute instability in this case. In addition, this mode has the lowest gyrotron starting current (Bratman et al. 1981 and Fliflet 1986) of 1 amp among all CRM interactions between TE waveguide modes and harmonic ($s = 1, 2, 3$) beam modes. A hollow breakdown pattern in the fluorescent light tubes is shown in Figure 13. The breakdown pattern is clearly hollow (the breakdown ring radius is about half of the output horn radius), and thus it is concluded that the output mode is definitely not a TE_{11} gyro-BWO, but a TE_{21} absolute instability. In addition, in the frequency measurement, we have observed microwaves in the 6.6 - 10 GHz bandpass filter which includes the TE_{21} absolute instability. We ruled out the TE_{31} CARM and high harmonic gyrotron modes such as a second harmonic TE_{51} or third harmonic TE_{51} in interpreting the breakdown pattern because the maximum electric field was not observed near the edge of the output window.

Microwave emission data versus cavity magnetic fields are shown in Figure 14. Note that there is a sharp microwave cutoff at $B \sim 5.8 - 5.9$ kG at which exists the onset for absolute instability. Calculated critical currents of absolute instability (Davies et al. 1990) versus cavity magnetic field for $\alpha = 0.5, 0.6$, and 0.7 are shown in Figure 15. With the e-beam current of 20 - 30 amps, the experimental regime of the absolute instability agrees fairly well with the prediction. It should be noticed that, by lowering the cavity magnetic field below 5.8 kG, we could successfully suppress the TE_{21} absolute instability, which is believed to be the strongest competing mode in the present Bragg resonator BRFO experiment.

4.2. High-Q Bragg resonator (BRHI) CRM experiments with a high current electron beam

In order to test the effect of Bragg resonators on high frequency gyrotron modes at high power levels, a series of experiments were performed with a high current electron beam with large energy spread extracted by a 24-hole apertured mask anode. For the case of this 24 hole apertured mask-anode, the peak power in the high frequency band ($f > 14.05$ GHz) is increased by more than 6 dB, compared with the power measured from the 80 hole apertured mask-anode. This power increase is attributed to the 6 - 7 times higher beam current (150 - 200 amps) than the beam current of about 30 amps produced from the 80 hole apertured mask-anode. Small signal theory (Fliflet 1986) predicts that the spatial growth rate, $k_{||}$, is proportional to the one-third power of beam current, $I^{1/3}$. Since, in the linear growth regime, the wave power grows as $P = P_{in} \exp(2k_{||}L)$ where P_{in} is the initial power built in the cavity from RF noise and L is the cavity interaction length, the power increase due to the increased beam current is expected to be $\Gamma(\text{dB}) = 10 \log (P_2/P_1) \cong 10 \log \{ \exp(2(k_{||2} - k_{||1})L) \}$ where the subscripts 1 and 2 are for the cases of the beam current of 30 amps and the increased beam current of 150 - 200 amps respectively, and we assume that the initial RF power for the case of the 30 amp beam is equal to that for the case of the 150 - 200 amp beam. With the beam and cavity parameters ($\gamma = 2.37$, $\alpha = 0.5$, $B = 6$ kG, $L = 29.6$ cm) the power increase was calculated to be 7.7 dB. This power scaling agrees with the experimental observation within the 3 dB uncertainty of power measurements. From frequency measurement in the 15.5 - 16 GHz bandpass filter at about 5 kG, most of the power in the high frequency band ($f > 14.05$ GHz) is believed to originate from the second harmonic TE_{51} gyrotron mode. This observation is consistent with the earlier experiments with the 80 hole apertured mask-anode.

In the 6.6 - 10 GHz band (total attenuation is 74 dB), we have observed high power (1 - 5 MW) microwave emission, which originated from the TE_{21} absolute

instability. Figure 16(a) shows a scan of peak power in the 6.6 - 10 GHz band versus cavity magnetic field for diode magnetic field of 0.7 kG.

We have also observed microwave emission in the 2.1 - 6.6 GHz band which includes the TE_{11} gyro-BWO interaction. Figure 16(b) shows a scan of peak power in the 2.1 - 6.6 GHz band as a function of cavity magnetic field. The radiation power in this band did not increase significantly, compared with the power obtained from the 80 hole apertured mask-anode. It is very interesting to notice, as shown in Figure 16(a) and 16(b), that when there was microwave emission in the 2.1 - 6.6 GHz band, the microwave emission in the 6.6 - 10 GHz was suppressed, showing mode competition between the TE_{21} absolute instability and the TE_{11} gyro-BWO interaction at the cavity magnetic field of ~ 5.15 kG.

A fluorescent light bulb diagnostic was employed in order to identify the output mode. Figure 17 shows open shutter camera photos of the gas breakdown pattern in the fluorescent light tubes as a function of cavity magnetic field. Hollow patterns have been observed for the cavity magnetic field greater than 6.9 kG. The ring radius was about half of the output horn radius and thus the radiation was confirmed to be the TE_{21} mode, as expected from the theoretical prediction of the TE_{21} absolute instability and the frequency measurements.

Figure 18 shows an explicit illustration of the regimes in which the TE_{21} absolute instability overwhelms the TE_{11} gyro-BWO. The gas breakdown pattern changed to a solid pattern when we lowered the cavity magnetic field to 5.2 kG. As shown in Figure 17(d), the breakdown pattern appears to be a mixed pattern of the hollow and solid patterns, indicating that both TE_{21} absolute instability and TE_{11} gyro-BWO were excited. Further decrease of the cavity magnetic field produced a single solid pattern (see Figure 17(e)). At the same time, the frequency was measured in the 4.3 - 6.6 GHz band. This confirms that the radiation is the TE_{11} mode, originating from the TE_{11} gyro-BWO interaction. The identification of the TE_{11} radiation mode is consistent with the earlier

experiments with the 80 hole apertured mask-anode where we observed high power microwave emission in the 2.1 - 6.6 GHz band.

5. Summary and conclusions

Experiments have been performed to characterize the cyclotron maser interactions of a long-pulse electron beam interaction in a Bragg resonator designed for excitation of the TE_{31} CARM modes. Experiments were performed for four cases:

- 1) Bragg resonator with ripples half-inward and a large diameter smooth center section, (BRHI),
- 2) Smooth tube of large diameter without the Bragg reflectors,
- 3) Bragg resonator with ripples fully-outward with small diameter smooth center section, (BRFO), and
- 4) Smooth tube of small diameter without Bragg reflectors.

Two major parasitic oscillations have been observed in conducting the Bragg resonator with ripples half-inward (BRHI) CRM experiments with the high quality e-beam of 20 - 80 amps: the first harmonic TE_{11} gyro-BWO and second harmonic gyrotron interactions near cutoffs of higher order TE modes. We successfully suppressed the TE_{11} gyro-BWO by increasing the cavity magnetic field to 6.4 kG. However, high harmonic gyrotron interactions remain a serious parasitic oscillation and dominate over the TE_{31} Bragg CARM mode. It is believed that the inward protrusion of the ripples acts as an iris inside the straight section cavity and thus the diffraction Q becomes higher for those undesired modes, resulting in low starting current.

The Bragg resonator with ripples fully-outward (BRFO) produced microwave emission of which most of the power in the high frequency band ($f > 14.05$ GHz) was measured in the 18.7 - 19.7 GHz band (including the third harmonic TE_{51} gyro-BWO frequency). For the case of the small diameter smooth tube without Bragg resonator, the power in the high frequency band ($f > 14.05$ GHz) was not significantly higher than for

the case of the Bragg resonator BRFO, but the measured frequency was observed mostly in the 15.5 - 16 GHz band (which includes the second harmonic TE_{41} gyrotron interaction). Considerably less power from the TE_{11} gyro-BWO was observed for the Bragg resonator BRFO than for the small diameter smooth tube case. The gas breakdown patterns obtained by the use of fluorescent light tubes showed only the hollow pattern with the radius half of the output horn radius, suggesting that the TE_{21} ($s = 1$) mode is dominant. The microwave emission from the TE_{21} absolute instability in the Bragg resonator BRFO was successfully suppressed by lowering the cavity magnetic field whereas the third harmonic TE_{51} gyro-BWO interaction remained a competing mode. Two undesired oscillations, (TE_{21} ($s = 1$) absolute instability, and TE_{51} ($s = 3$) gyro-BWO), were the most serious competing modes in the present Bragg resonator BRFO experiments, apparently suppressing the TE_{31} CARM oscillation.

In the Bragg resonator (ripples half-inward), gyrotron experiments with a high current electron beam of 150 - 200 amps, we have observed mode competition between the TE_{21} ($s = 1$) absolute instability and the TE_{11} ($s = 1$) gyro-BWO interaction by the use of frequency measurements and gas breakdown diagnostics. Clearly, the TE_{21} absolute instability is the dominant mode at high cavity magnetic fields ($B \geq 6.9$ kG) and the TE_{11} gyro-BWO becomes dominant at low magnetic fields ($B \leq 5.2$ kG). It was also shown that a mode transition occurred from a hollow pattern (TE_{21}) to a solid pattern (TE_{11}) by lowering the cavity magnetic field.

The present work provides important experimental evidence on the TE_{11} and TE_{21} absolute instabilities in operating a high order CARM mode in a high-Q Bragg resonator. No matter how high the external feedback provided by the Bragg reflector, the backward wave growth rate is sufficient to suppress all other modes. Another important finding is that harmonic gyrotron and gyro-BWO interactions are strongly excited in Bragg resonators and these may suppress the desired CARM oscillations (Barnett et al. 1989).

Acknowledgements

We would like to acknowledge valuable discussions with Dr. Y. Y. Lau and Dr. B. Danly. This work is supported by the Air Force Office of Scientific Research and the Air Force Phillips Weapons Laboratory. T. A. Spencer acknowledges an Air Force Laboratory Graduate Fellowship.

References

- Barnett, L. R., Chang, L. H., Chen, H. Y., Chu, K. R., Lau, W. K., and Tu, C. C., 1989, Absolute instability competition and suppression in a millimeter-wave gyrotron traveling-wave tube, *Phys. Rev. Lett.*, 63(10), 1062-1065.
- Bekefi, G., DiRienzo, A., Leibovitch, C., and Danly, B. G., 1989, 35 GHz cyclotron autoresonance maser amplifier, *Appl. Phys. Lett.*, 54(14), 1302-1304.
- Botvinnik, I. E., Bratman, V. L., Volkov, A. B., Ginzburg, N. S., Denisov, G. G., Kol'chugin, B. D., Ofitserov, M. N., and Petelin, M. I., 1982 a, Free-electron masers with Bragg resonators, *JETP Lett.*, 35(10), 516-519.
- Botvinnik, I. E., Bratman, V. L., Volkov, A. B., Denisov, G. G., Kol'chugin, B. D., and Ofitserov, M. N., 1982 b, Cyclotron-autoresonance maser with a wavelength of 2.4 mm, *Sov. Tech. Phys. Lett.*, 8(11), 596-597.
- Bratman, V. L., Ginzburg, N. S., Nusinovich, G. S., Petelin, M. I., and Strelkov, P. S., 1981, Relativistic gyrotrons and cyclotron autoresonance masers, *Int. J. Electronics*, 51(4), 541-567.
- Choi, J. J., 1991 a, Bragg resonator cyclotron resonance maser experiments driven by a microsecond, intense electron beam accelerator, Doctoral Thesis, University of Michigan, Dept. of Nuclear Engineering.
- Choi, J. J., Gilgenbach, R. M., Spencer, T. A., Menge, P., and Ching, H., 1991 b, Measurement of long-pulse relativistic electron beam perpendicular to parallel

- velocity ratio by Cerenkov emission and radiation darkening on a glass plate, *Rev. Sci. Instru.* Accepted for publication.
- Chong, C. K., Razeghi, M. M., McDermott, D. B., Luhmann, N. C., Jr., Thumm, M., and Pretterebner, J., 1991, Bragg reflectors; tapered and untapered, *SPIE conf. on beams and high power microwaves* (Los Angeles, California).
- Danly, B. G., 1990, High power CARM experiments, *Proc. of 15th Int. Conf. on Infrared & MM Waves* (Orlando, Florida), 664-668.
- Davies, J. A., Davidson, R. C., and Johnson, G. L., 1990, Pulse shapes for absolute and convective cyclotron-resonance-maser instabilities, *I.E.E.E. Trans. Plasma Science*, 18(3), 286-300.
- Denisov, G. G., and Reznikov, M. G., 1983, Corrugated cylindrical resonators for short-wavelength relativistic microwave oscillators, *Radiophys. and Quant. Electron.*, 407-413.
- Fliflet, A. W., and Read, M. E., 1981, Use of weakly irregular waveguide theory to calculate eigenfrequencies, Q values, and RF field functions for gyrotron oscillators, *Int. J. Electronics*, 51(4), 475-484.
- Fliflet, A. W., 1986, Linear and nonlinear theory of the Doppler-shifted cyclotron resonance maser based on TE and TM waveguide modes, *Int. J. Electronics*, 61(6), 1049-1080.
- Gilgenbach, R. M., Read, M. E., Hackett, K. E., Lucey, R. F., Jr., Hui, B., Granatstein, V. L., and Chu, K. R., 1980, Heating at the electron cyclotron frequency in the ISX-B Tokamak, *Phys. Rev. Lett.*, 44(10), 647-650.
- Gilgenbach, R. M., Horton, L. D., Lucey, R. F., Jr., Bidwell, S., Cuneo, M. E., Miller, J., and Smutek, L., 1985, Microsecond electron beam diode closure experiments, Invited paper in *Proc. 5th I.E.E.E. Pulsed Power Conf.* (Arlington, Virginia), 126-132.

- Gold, S. H., Fliflet, A. W., Manheimer, W. M., Black, W. M., Granatstein, V. L., Kinkead, A. K., Hardesty, D. L., and Sucky, M., 1985, High-voltage Ka-band gyrotron experiment, *I.E.E.E. Trans. on Plasma Science*, 13(6), 374-382.
- Granatstein, V. L., 1987, Gyrotron experimental studies, *High power microwave generation* (Artech House), Edited by Granatstein, V. L., and Alexeff, I., 185-205.
- McCowan, R. B., Fliflet, A. W., Gold, S. H., Granatstein, V. L., and Wang, M. C., 1988, Design of a waveguide resonator with ripples wall reflectors for a 100 GHz CARM oscillator experiment, *Int. J. Electronics*, 65(3), 463-475.
- Palmer, A. J., 1987, Coupled mode theory of overmoded cylindrical metal Bragg reflectors, *I.E.E.E. J. Quantum Electron.*, QE-23(1), 65-70.
- Park, S. Y., Kyser, R. H., Armstrong, C. M., Parker, R. K., and Granatstein, V. L., 1990, Experimental study of a Ka-band gyrotron backward-wave oscillator, *I.E.E.E. Trans. Plasma Science*, 18(3), 321-325.
- Sucher, M., 1963, Measurement of Q, *Handbook of microwave measurements*, edited by Sucher, M., and Fox, J. (Polytechnic press), Vol. 2, 417-493.
- Wang, J. G., Gilgenbach, R. M., Choi, J. J., Outten, C. A., and Spencer, T. A., 1989, Frequency tunable, high power microwave emission from cyclotron maser oscillation and gyrotron interaction, *I.E.E.E. Trans. Plasma Science*, 17(6), 906-908.

Table 1. Summary of CRM and Bragg resonator parameters

- upstream Bragg resonator:
 - one period = 0.95 cm
 - corrugation amplitude = ± 0.16 cm
 - number of periods = 15
 - average radius = 1.93 cm
 - reflectivity = 0.99 for TE₃₁ mode at 18.9 GHz
- downstream Bragg resonator: same as the upstream
- straight section cavity:
 - length = 29.4 cm
 - radius = 1.93 cm or 1.64 cm
- design mode = TE₃₁ CARM
- MELBA beam voltage = 0.7 MV
- beam current = 20 - 80 amps
- cavity magnetic field = 4 - 7 kG
- measured beam velocity ratio = 0.4 - 0.74 (adjustable)
- total Q of TE₃₁ = 4600 (measured)
- CARM starting current of TE₃₁ mode = ~ 2 amps at ~ 5 kG.

Table 2. Cold test results vs. calculations (calculated values from uncoupled single mode theory are shown in parentheses)

mode	Bragg resonant frequency (GHz)	reflectivity of a single Bragg reflector(%)
-----	-----	-----
TE ₁₁	16.44 (16.42)	92±5 (83)
TM ₀₁	16.88 (16.85)	95±5 (99)
TE ₂₁	(17.5)	(98)
TE ₀₁	(18.42)	(40)
TM ₁₁	(18.42)	(99)
TE ₃₁	18.93 (18.98)	95±5 (99)
TM ₂₁	(20.28)	(99)
TE ₄₁	(20.56)	(99)
TM ₃₁	(22.33)	(99)
TM ₄₁	(24.55)	(99)

Figure captions

Figure 1. Experimental configuration of Bragg resonator CRM experiments.

Figure 2. Apertured mask-anode (a) 80 hole apertured mask-anode used for the high-Q Bragg resonator CRM experiments with high quality electron beam, (b) 24 hole apertured mask-anode used for the high-Q Bragg resonator gyrotron experiments with high current electron beam.

Figure 3. Configuration of measuring (a) reflectivity and frequency of a Bragg reflector, and (b) Bragg resonator Q and frequency.

Figure 4. Two configurations of Bragg resonator.

Figure 5. Data of electron beam characterization:

(a) MCP photograph of Cerenkov emission (contrast enhanced photographically), (b) radiation darkening on glass plate ($\alpha \sim 0.56$), (c) MELBA e-beam voltage (310 kV/div), (d) gate pulse of MCP camera, (e) cathode stalk current (4.5 kA/div), (f) apertured beam current (40 amps/div), and (g) anode current (3.5 kA/div). The magnetic fields are $B_1 = 0.5$ kG and $B_2 = 5$ kG. Oscilloscope sweep time is 200 ns/div.

Figure 6. Uncoupled dispersion relations of TE modes and harmonic beam modes where cavity radius = 1.93 cm, cavity magnetic field = 5 kG, $\alpha = 0.5$, and beam voltage = 680 kV.

Figure 7. A scan of peak microwave power measured in the 2.1 - 6.6 GHz band versus cavity magnetic fields where the diode magnetic field was 0.7 kG.

Figure 8. Typical waveforms : (a) Bragg resonator with ripples half-inward (top: voltage (310 kV/div), middle: bandpass filtered microwaves ($18.9 < f < 19.2$ GHz), bottom: high frequency ($f > 14.05$ GHz) microwaves, (b) smooth tube without Bragg reflectors (the signal channels are the same as (a)). The diode magnetic field is 0.4 kG and the cavity magnetic field is 6.4 kG for both cases. Sweep time on the oscilloscope is 200 ns/div.

Figure 9. Coupling strength of TE waveguide modes in a corrugation surface versus the resonant frequencies of Bragg modes.

Figure 10. Beam-wave coupling strength in a straight section cavity where the CRM instability occurs.

Figure 11. Typical waveforms for the case of Bragg resonator with ripples fully-outward (top: voltage (310 kV/div), middle: bandpass filtered microwaves ($19.2 < f < 19.7$ GHz), bottom: high frequency ($f > 14.05$ GHz) microwaves). Sweep time on the oscilloscope is 200 ns/div.

Figure 12. A scan of microwave peak power in the 2.1 - 6.6 GHz band versus cavity magnetic field for the Bragg resonator with ripples fully-outward (BRFO) and the smooth tube. The diode magnetic field is kept at 0.4 kG.

Figure 13. Experimental data (M2431) on fluorescent light tube diagnostic: (a) light emission from fluorescent light tubes (open shutter camera photo), (b) model of microwave breakdown on fluorescent light tubes. Diode magnetic field is 0.4 kG and cavity magnetic field is 6.25 kG. Note that the photo shown here was reproduced with a higher contrast in order for the breakdown pattern to be easily visible.

Figure 14. Experimental data on TE₂₁ absolute instability. Microwave breakdown in fluorescent light tubes was observed at $B \geq 5.92$ kG.

Figure 15. Predicted e-beam current for TE₂₁ absolute instability versus cavity magnetic field for $\alpha = 0.5, 0.6$ and 0.7 . High power microwave emission and microwave break-down were observed from beam current of $20 \sim 30$ amps at $B \geq 5.92$ kG.

Figure 16. (a) Peak power in the 6.6 - 14.1 GHz band versus cavity magnetic field for the diode magnetic fields of 0.7 kG, (b) peak power in the 2.1 - 6.6 GHz band versus cavity magnetic field (diode magnetic field = 0.7 kG).

Figure 17. Open shutter camera photos of gas breakdown pattern obtained from fluorescent light tubes as a function of cavity magnetic field (f-stop = 11). Diode magnetic field is kept at 0.7 kG. Note that photo (a), (b), and (c) show hollow patterns with the ring radius of half of the output horn radius, indicating a TE₂₁ mode, whereas photo (d) shows a mixed pattern of TE₂₁ and TE₁₁ mode, and (e) shows solid patterns on the center, indicating a TE₁₁ mode. The breakdown pattern disappeared at $B \leq 2.7$ kG (photo (f)).

Figure 18. Uncoupled dispersion relations of TE₁₁ and TE₂₁ modes with the fundamental beam mode of six different cavity magnetic fields, showing good agreement with the observed breakdown patterns in Figure 17. The diamond black dots denote the CRM interaction points.

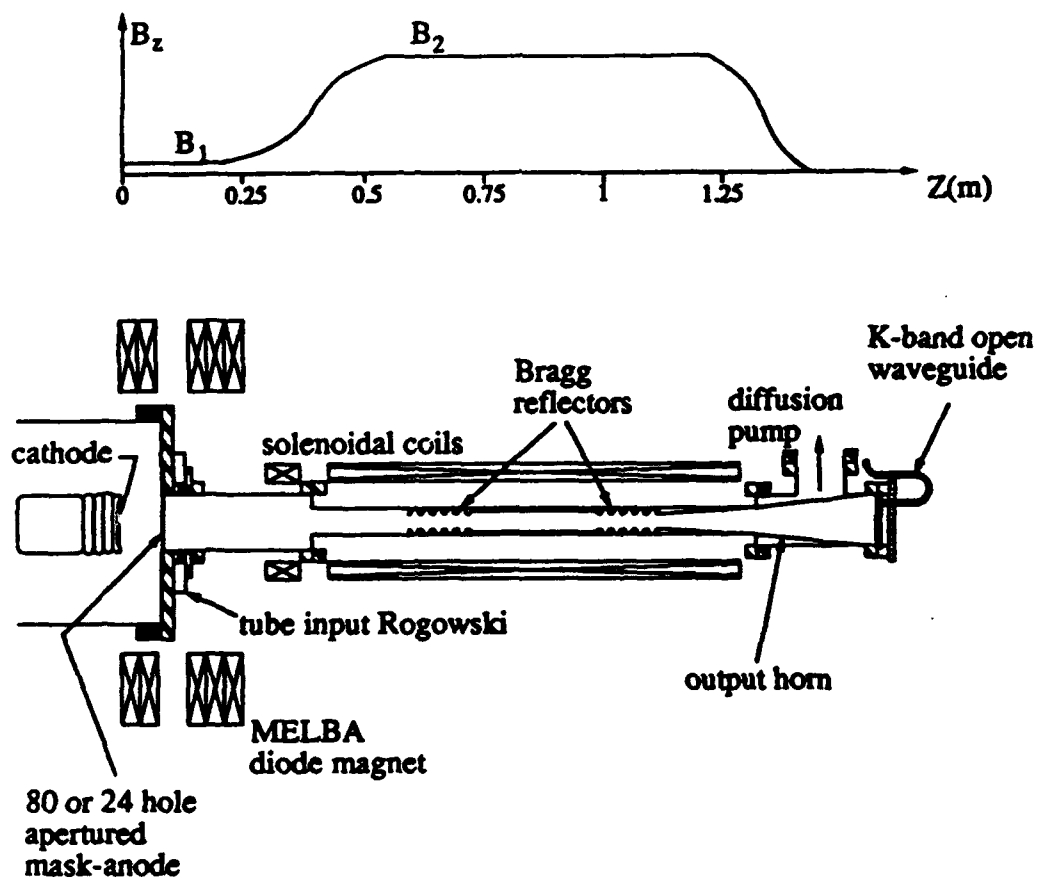


Figure 1. Experimental configuration of Bragg resonator CRM experiments.

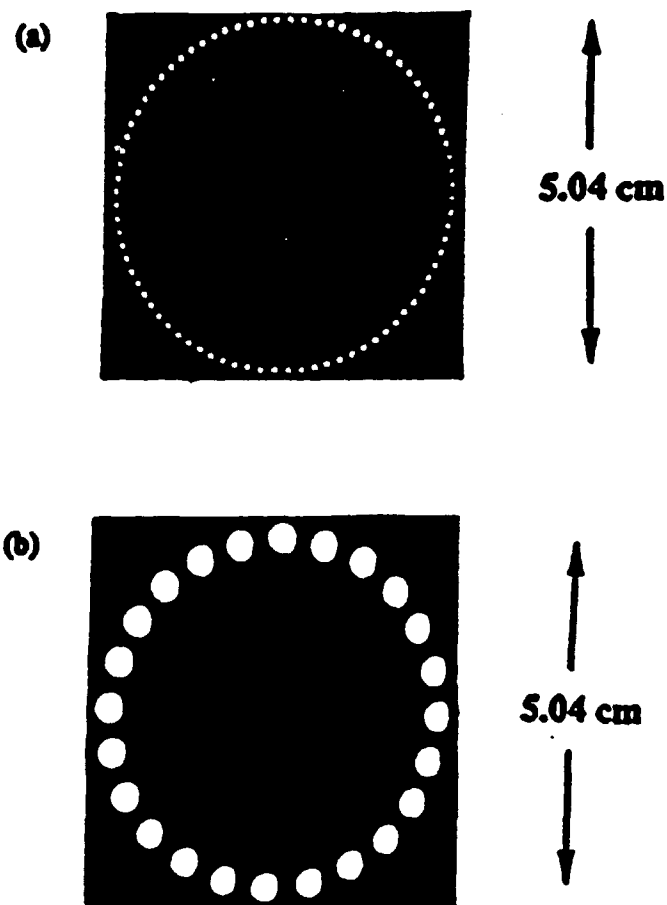


Figure 2. Apertured mask-anode (a) 80 hole apertured mask-anode used for the high-Q Bragg resonator CRM experiments with high quality electron beam, (b) 24 hole apertured mask-anode used for the high-Q Bragg resonator gyrotron experiments with high current electron beam.

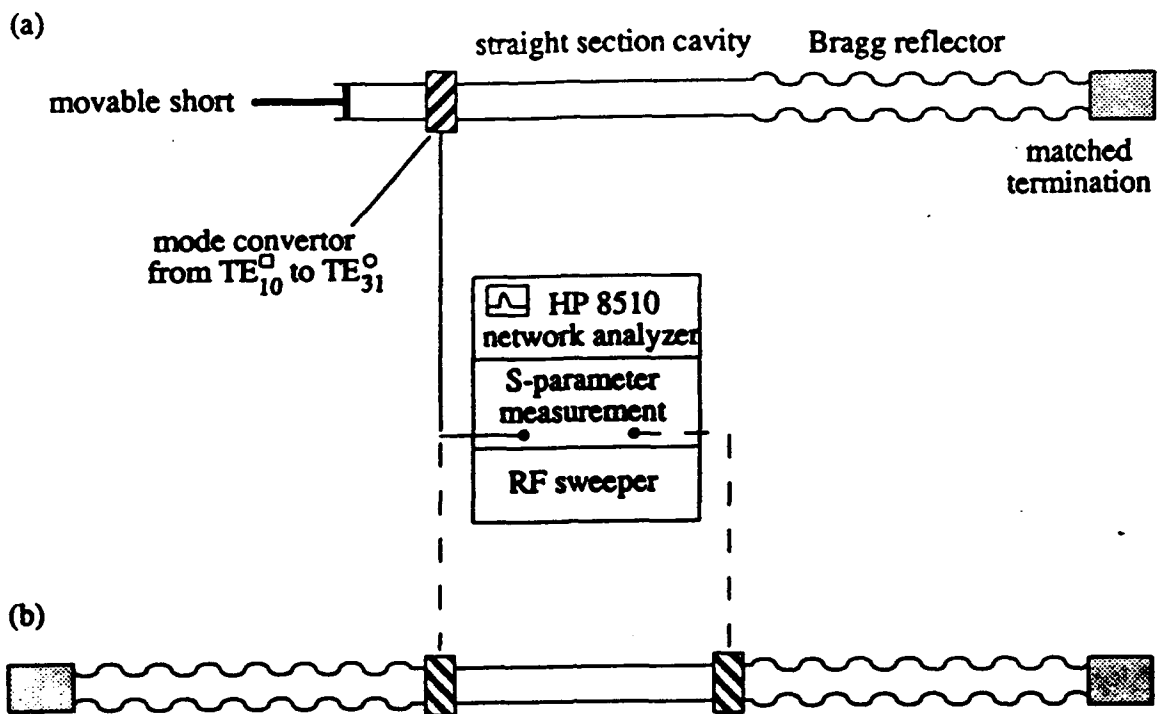


Figure 3. Configuration of measuring (a) reflectivity and frequency of a Bragg reflector, and (b) Bragg resonator Q and frequency.

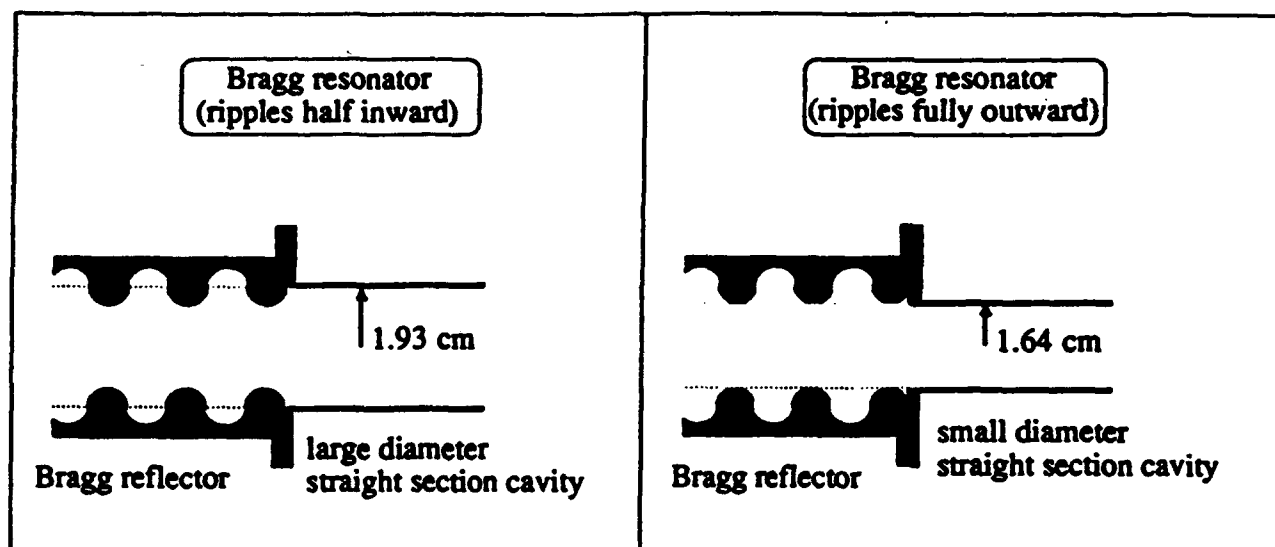


Figure 4. Two configurations of Bragg resonator.

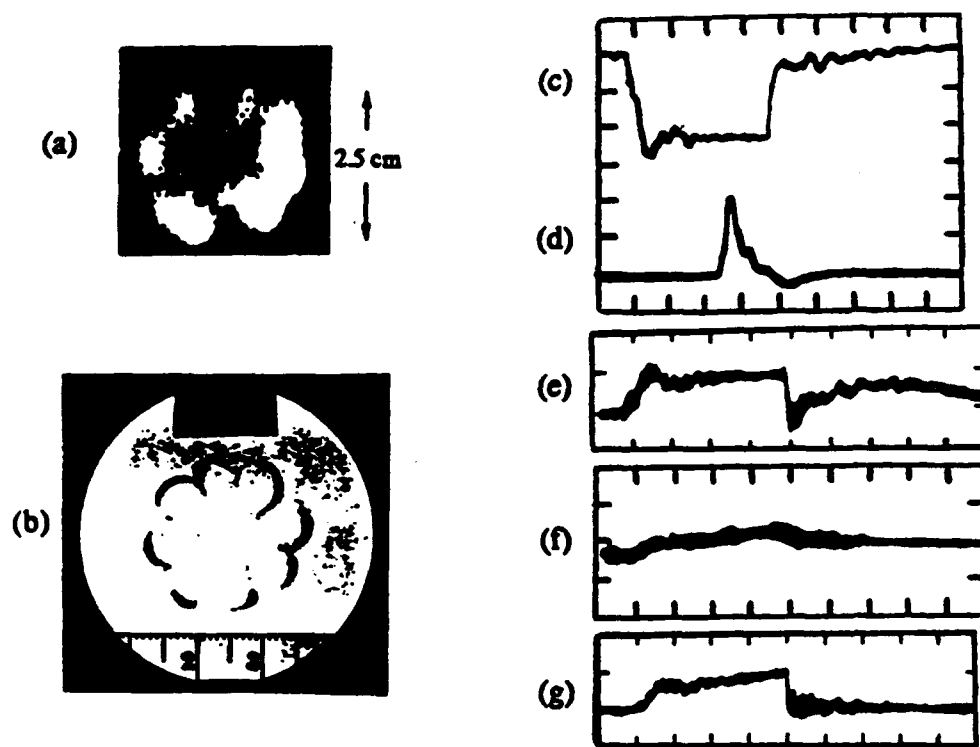


Figure 5. Data of electron beam characterization:
 (a) MCP photograph of Cerenkov emission (contrast enhanced photographically), (b) radiation darkening on glass plate ($\alpha \sim 0.56$), (c) MELBA e-beam voltage (310 kV/div), (d) gate pulse of MCP camera, (e) cathode stalk current (4.5 kA/div), (f) apertured beam current (40 amps/div), and (g) anode current (3.5 kA/div). The magnetic fields are $B_1 = 0.5$ kG and $B_2 = 5$ kG. Oscilloscope sweep time is 200 ns/div.

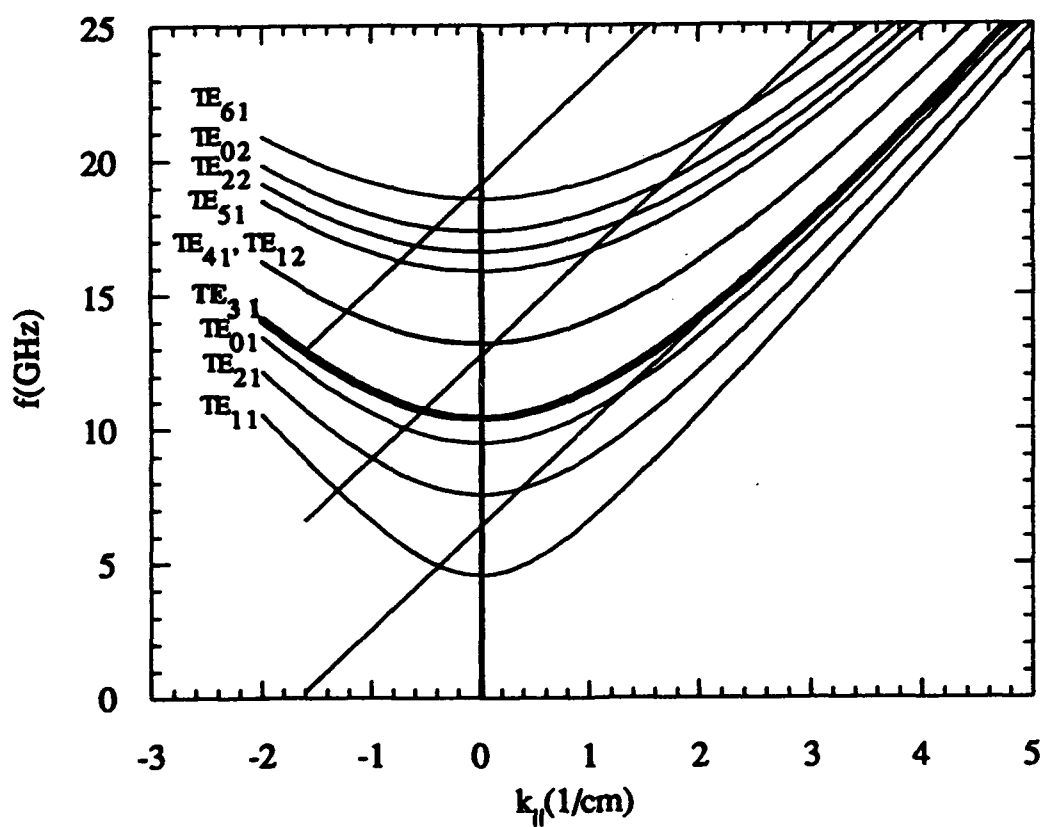


Figure 6. Uncoupled dispersion relations of TE modes and harmonic beam modes where cavity radius = 1.93 cm, cavity magnetic field = 5 kG, $\alpha = 0.5$, and beam voltage = 680 kV.

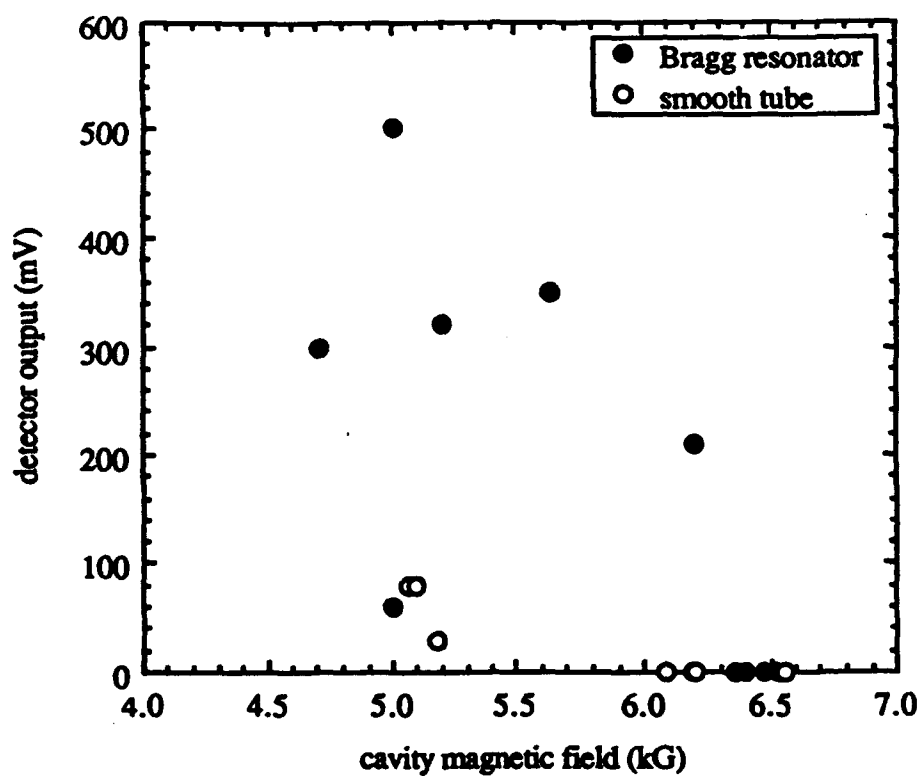


Figure 7. A scan of peak microwave power measured in the 2.1 - 6.6 GHz band versus cavity magnetic fields where the diode magnetic field was 0.7 kG.

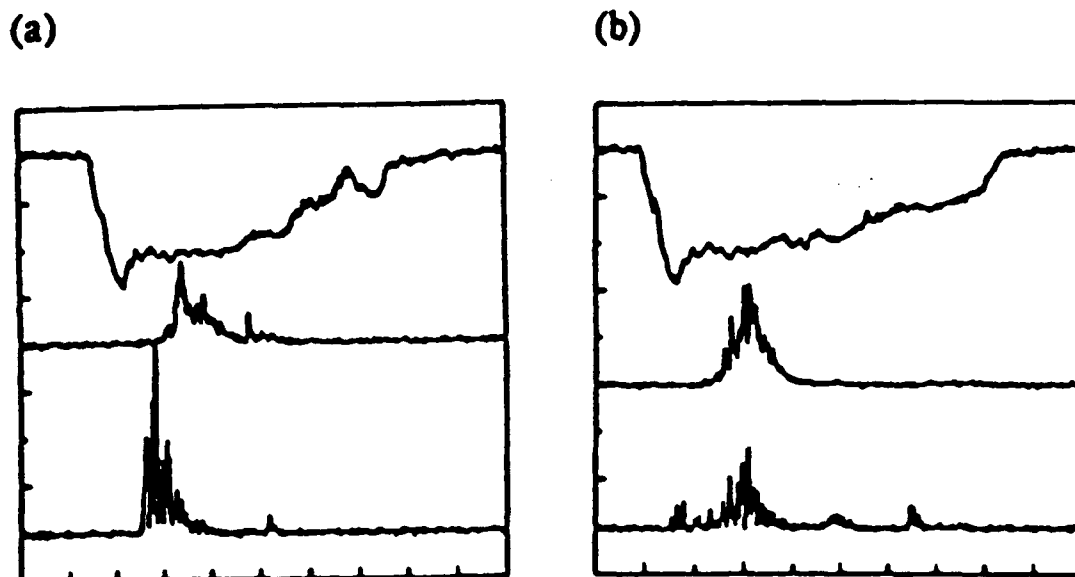


Figure 8. Typical waveforms : (a) Bragg resonator with ripples half-inward (top: voltage (310 kV/div), middle: bandpass filtered microwaves ($18.9 < f < 19.2$ GHz), bottom: high frequency ($f > 14.05$ GHz) microwaves, (b) smooth tube without Bragg reflectors (the signal channels are the same as (a)). The diode magnetic field is 0.4 kG and the cavity magnetic field is 6.4 kG for both cases. Sweep time on the oscilloscope is 200 ns/div.

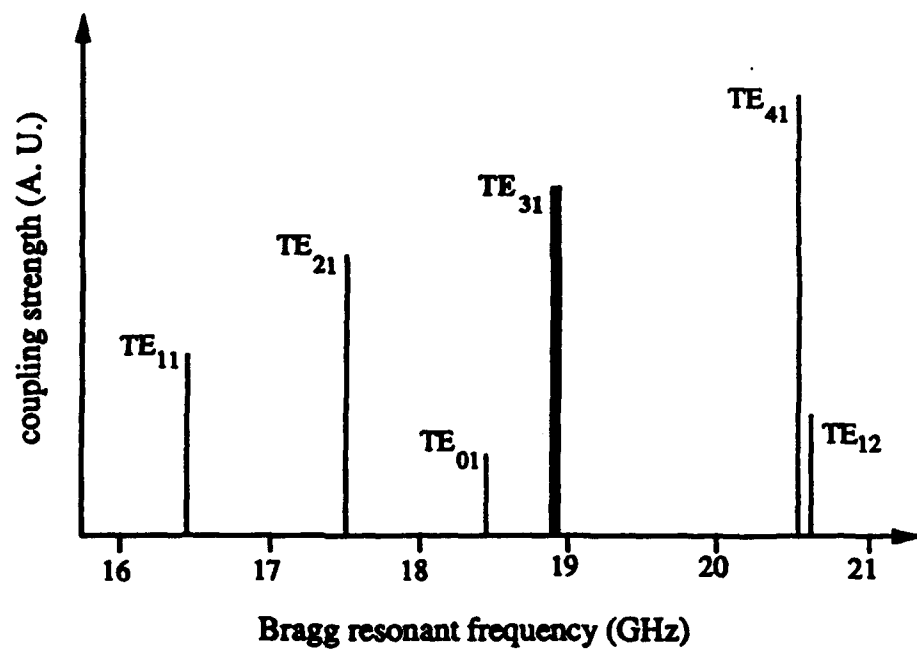


Figure 9. Coupling strength of TE waveguide modes in a corrugation surface versus the resonant frequencies of Bragg modes.

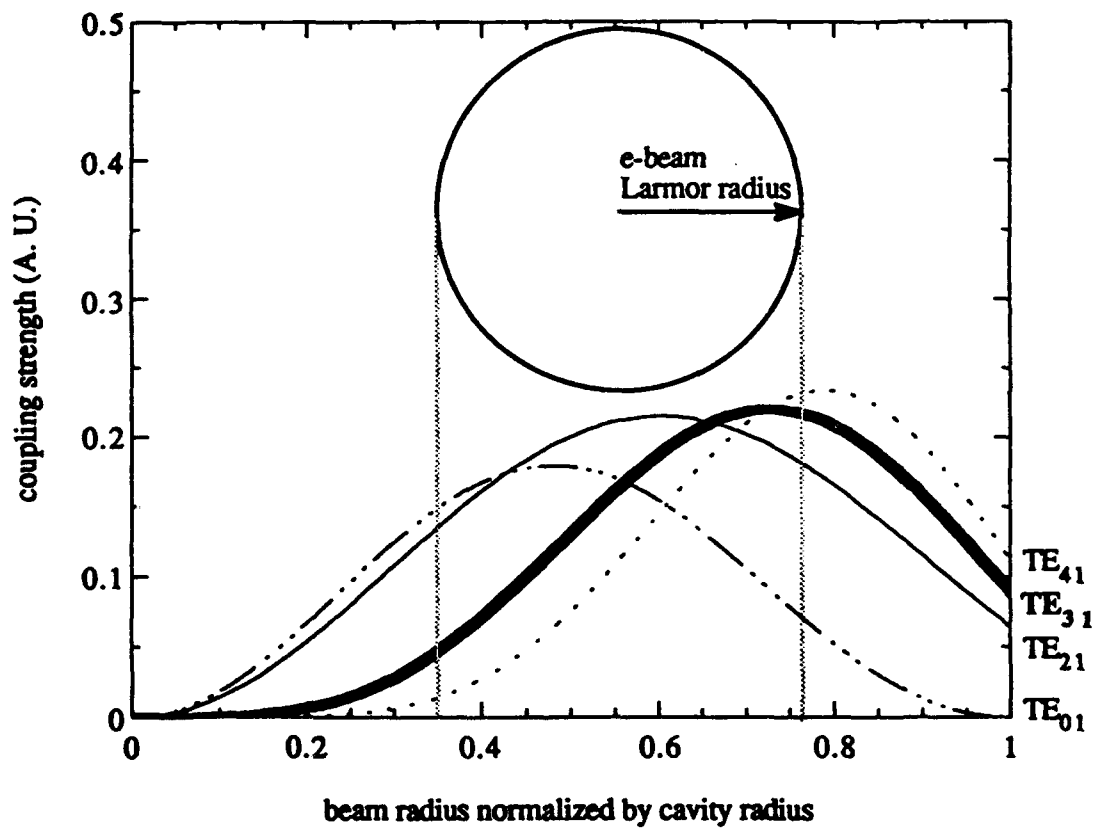


Figure 10. Beam-wave coupling strength in a straight section cavity where the CRM instability occurs.

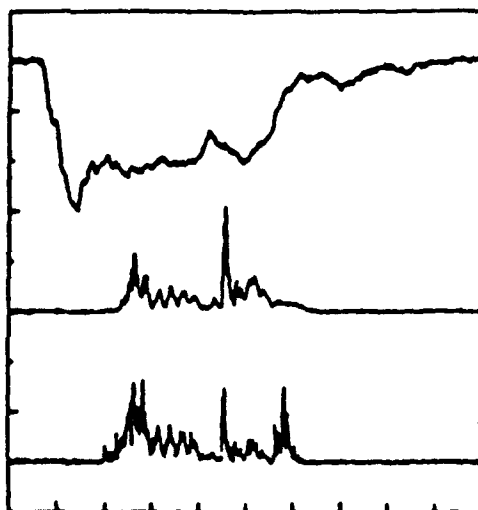


Figure 11. Typical waveforms for the case of Bragg resonator with ripples fully-outward (top: voltage (310 kV/div), middle: bandpass filtered microwaves ($19.2 < f < 19.7$ GHz), bottom: high frequency ($f > 14.05$ GHz) microwaves). Sweep time on the oscilloscope is 200 ns/div.

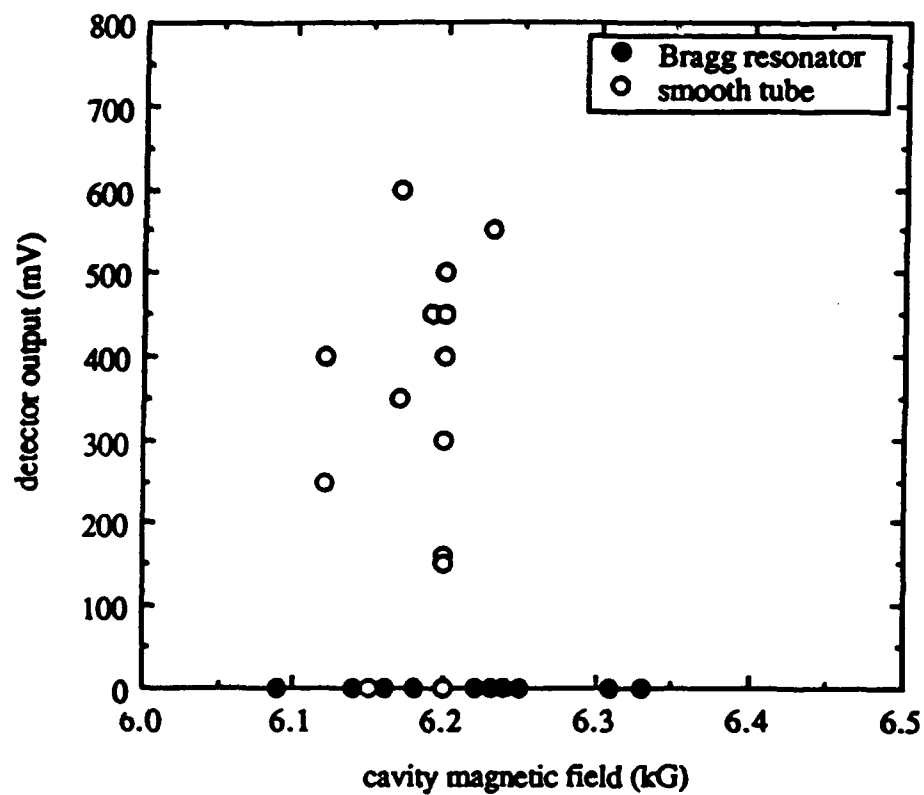


Figure 12. A scan of microwave peak power in the 2.1 - 6.6 GHz band versus cavity magnetic field for the Bragg resonator with ripples fully-outward (BRFO) and the smooth tube. The diode magnetic field is kept at 0.4 kG.

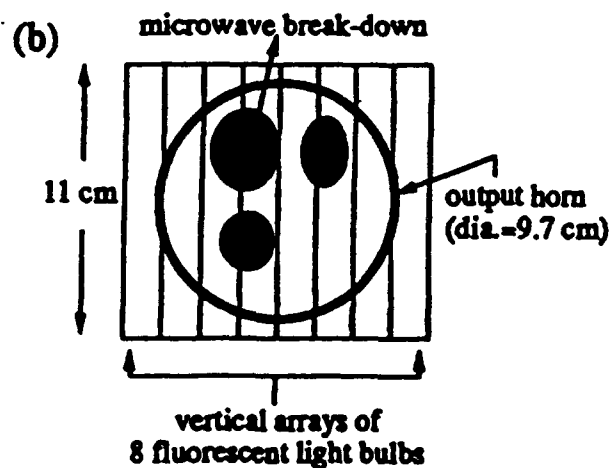
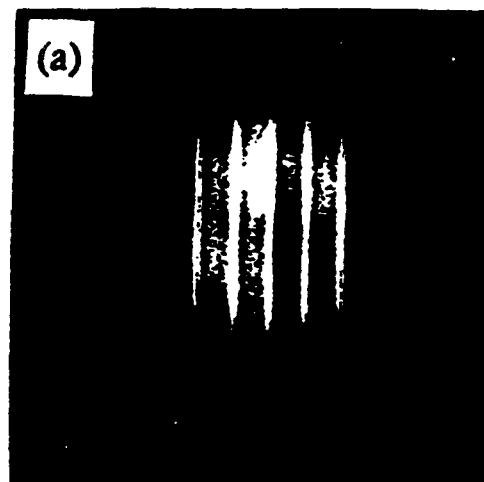


Figure 13. Experimental data (M2431) on fluorescent light tube diagnostic: (a) light emission from fluorescent light tubes (open shutter camera photo), (b) model of microwave breakdown on fluorescent light tubes. Diode magnetic field is 0.4 kG and cavity magnetic field is 6.25 kG. Note that the photo shown here was reproduced with a higher contrast in order for the breakdown pattern to be easily visible.

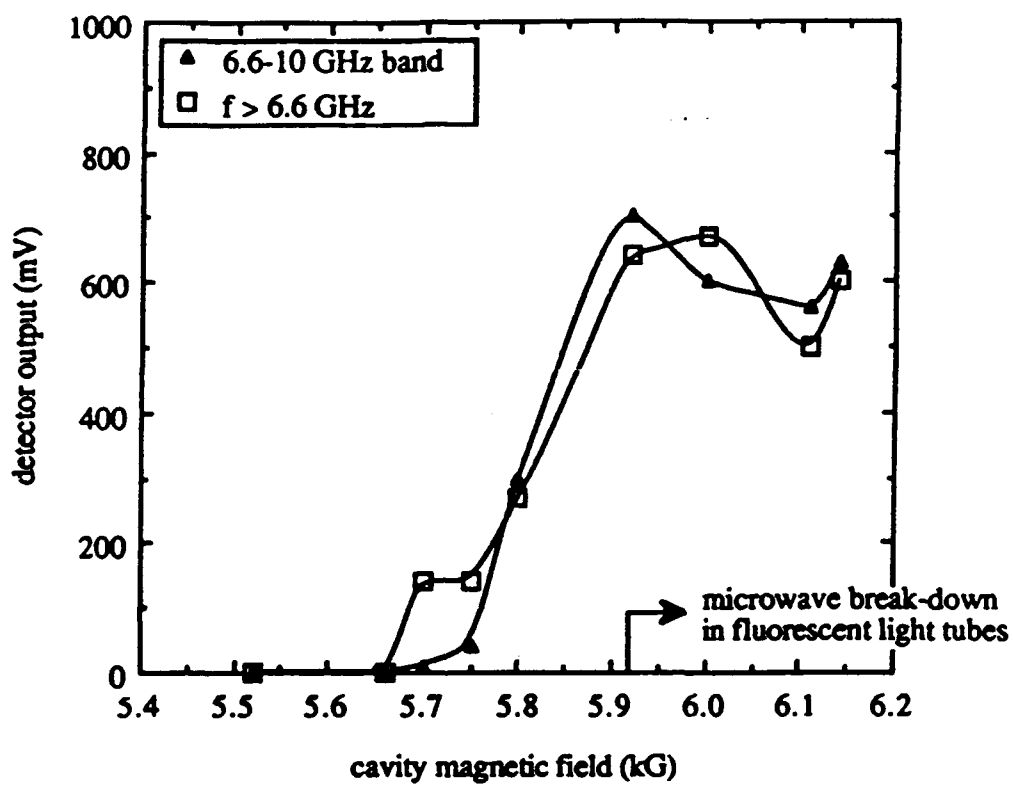


Figure 14. Experimental data on TE₂₁ absolute instability. Microwave breakdown in fluorescent light tubes was observed at $B \geq 5.92$ kG.

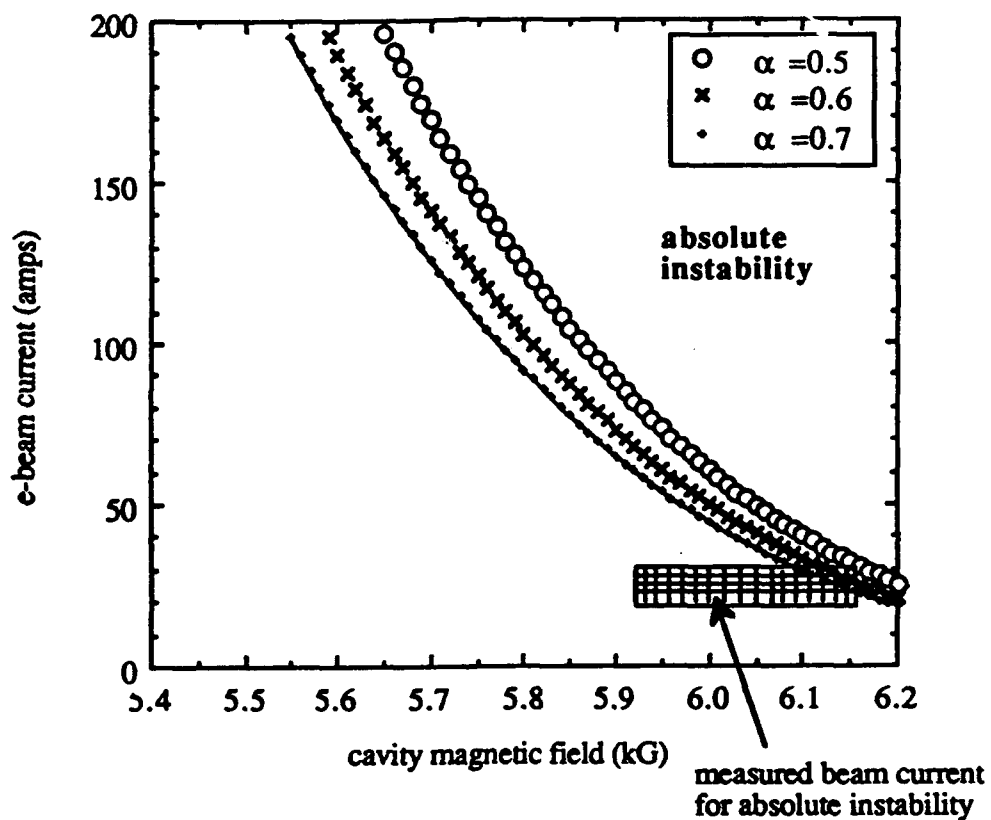


Figure 15. Predicted e-beam current for TE₂₁ absolute instability versus cavity magnetic field for $\alpha = 0.5, 0.6$ and 0.7 . High power microwave emission and microwave break-down were observed from beam current of $20 \sim 30$ amps at $B \geq 5.92$ kG.

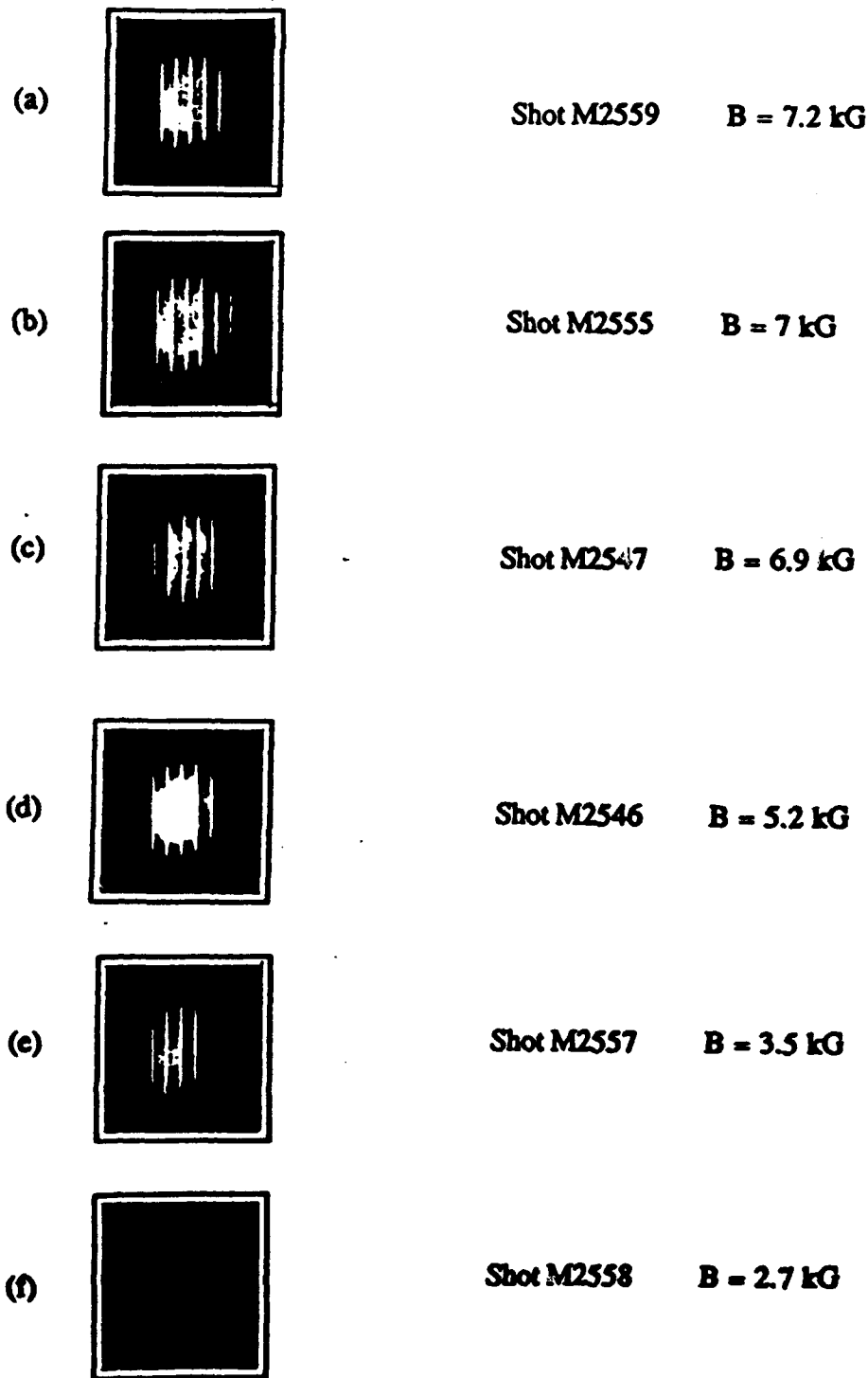


Figure 17. Open shutter camera photos of gas breakdown pattern obtained from fluorescent light tubes as a function of cavity magnetic field (f-stop = 11). Diode magnetic field is kept at 0.7 kG. Note that photo (a), (b), and (c) show hollow patterns with the ring radius of half of the output horn radius, indicating a TE_{21} mode, whereas photo (d) shows a mixed pattern of TE_{21} and TE_{11} mode, and (e) shows solid patterns on the center, indicating a TE_{11} mode. The breakdown pattern disappeared at $B \leq 2.7 \text{ kG}$ (photo (f))

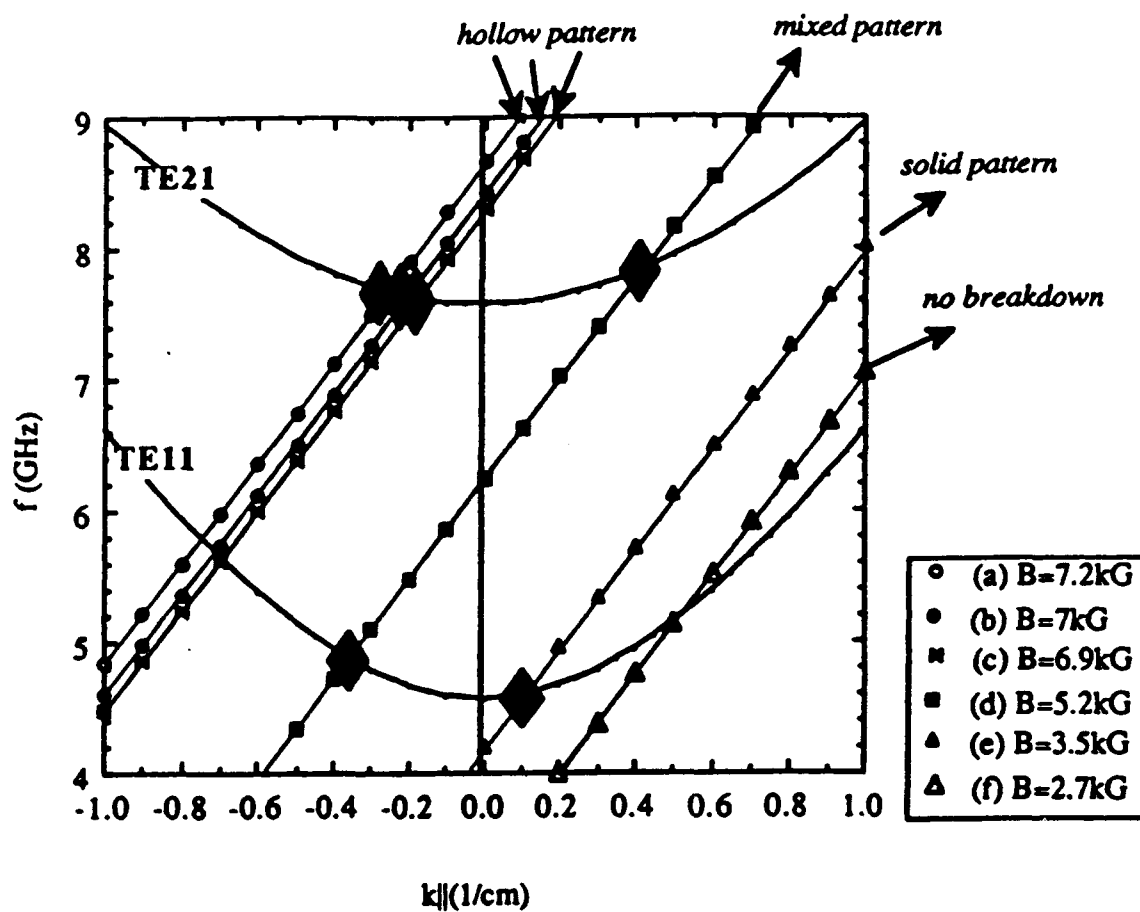


Figure 18. Uncoupled dispersion relations of TE_{11} and TE_{21} modes with the fundamental beam mode of six different cavity magnetic fields, showing good agreement with the observed breakdown patterns in Figure 17. The diamond black dots denote the CRM interaction points

Technical Notes

Frequency-Tunable, High-Power Microwave Emission From Cyclotron Autoresonance Maser Oscillation and Gyrotron Interactions

J. G. WANG, R. M. GILGENBACH, MEMBER, IEEE, J. J. CHOI, C. A. OUTTEN, AND T. A. SPENCER

Abstract—We report experimental observations of high-power microwave emission from both the high-frequency cyclotron autoresonance maser (CARM) oscillation and the low-frequency gyrotron interaction. High-power (3–10 MW) microwave emission is attributed to the CARM mechanism, which is magnetically tunable through discrete axial cavity modes from 15 through 16.7 GHz. For the same experimental parameters, megawatt level microwave emission is observed, which is magnetically tunable from 10 through 14 GHz, indicating low-frequency gyrotron oscillation. High-frequency microwave pulse-lengths of up to 0.2 μ s have been generated, which is a factor of five greater than previous CARM experiments.

Free electron sources [1] of high-power microwave radiation have significant applications in fusion plasma heating [2], communications [3], high gradient accelerators, and high-resolution radar. The gyrotron is typically referred to as the electron-cyclotron maser interaction, which occurs near the cavity cutoff frequency when the phase velocity is much greater than the velocity of light ($v_p \gg c$). Significant progress has been made in relativistic gyrotrons [4], [5] ($V \sim 1$ MV, $I = 1$ –10 kA), which have achieved 275-MW power levels at wavelengths of 8.5 mm and pulse-lengths of 20 ns. Gyrotrons driven by hard-tube modulators ($V < 100$ kV, $I < 100$ A) have achieved MW power levels of over μ s pulse-lengths. One limitation of conventional gyrotrons is that the output frequency is close to the relativistic cyclotron frequency $\Omega_e = eB/\gamma m$ or its harmonic. The cyclotron autoresonance maser (CARM) [5]–[9] has an advantage in this regard, since the wave frequency has a large, relativistic Doppler upshift, as shown by the upper intersection of the uncoupled dispersion relations in Fig. 1. In the limit as the phase velocity approaches c , this CARM mechanism is denoted the cyclotron autoresonance maser (CARM) [5]–[9]. Thus, very high-frequency microwaves can be obtained from the CARM for a relativistic electron beam in moderate magnetic fields. Another attractive feature of the CARM is the magnetic-tunability of the output frequency. Recent CARM amplifier experiments [8] have been reported in the United States, and CARM oscillator experiments [6], [7] have been performed in the Soviet Union. All of these previous CARM experiments have been performed with short-pulses (40–100 ns) electron beams. Several im-

Manuscript received July 3, 1989; revised September 14, 1989. This research was sponsored in part by the Air Force Office of Scientific Research (Dolling AFB), by the Air Force Weapons Laboratory, and (RMG) by a Presidential Young Investigator Award from the National Science Foundation. TAJ was supported by an Air Force Laboratory Graduate Fellowship. CAO received a Department of Energy Magnetic Fusion Technology Fellowship, and JGW was supported by the University of Michigan.

The authors are with the Intense Energy Beam Interaction Laboratory, Department of Nuclear Engineering, University of Michigan, Ann Arbor, MI 48109.

IEEE Log Number 8931983.

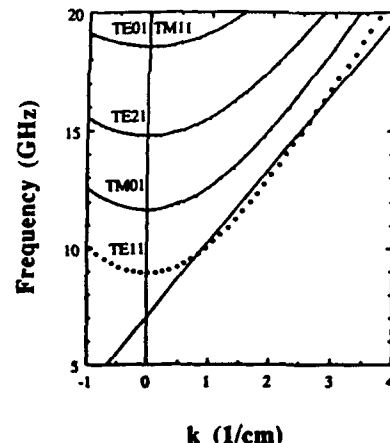


Fig. 1. Uncoupled dispersion relations of electron-beam cyclotron wave and cavity-waveguide modes for experiments; parameters are: $B_0 = 4.34$ kG, $V_b = 370$ kV, and $\alpha = v_z/v_b = 0.72$.

portant CARM research issues remain, which concern: 1) The frequency-tunability of CARM oscillators, 2) maximum e -beam voltage fluctuations for long-pulse (> 100 ns) oscillation, 3) low-frequency gyrotron interactions, and 4) the absolute instability, which is predicted to occur when the electron beam current exceeds a threshold value [10], [11].

In this technical note, we present cyclotron maser oscillator experiments which demonstrate frequency-tunable, high-power microwave emission from both the high-frequency CARM interaction (3–10 MW) and the low-frequency competing gyrotron mode (~ 1 MW). The phase velocity of the wave in the high-frequency operation of our experiment (16.7–15 GHz) was in the range (1.18–1.24 c) expected for the cyclotron autoresonance maser. The present experiments were performed by utilizing electron beam pulse-lengths (0.3–0.4 μ s), which are a factor of 4–10 longer than previous CARM experiments. These experiments were designed to investigate the basic physical mechanisms of the CARM and have not yet optimized the efficiency of the device nor attempted to suppress the low-frequency gyrotron interaction.

The experimental configuration is depicted in Fig. 2. The electron beam generator is a Febetron¹, operated with peak parameters: Voltage = –400 kV; current = 1.2 kA; and full pulse-length = 0.4 μ s. The electron beam is emitted from a field emission cathode consisting of a velvet ring with inner and outer radii of 0.6 and 1.3 cm, respectively. Cathode plasma diode closure caused a triangular voltage pulse, although the generator current was almost constant (Fig. 3). Pulsed magnetic field coils in the diode region were connected in series, with the solenoid wound on the 2.84-cm ID beam tube; this gave a factor of three increase in the axial magnetic field from the cathode to the interaction region. A cylindrical stainless steel microwave cavity was employed with dimensions of 1.97-cm ID and 26.32-cm length; the cavity vacuum cutoff frequency was 8.90 GHz. The electron-beam current transported through the cavity ranged from 400 A at a 3-kG magnetic field to 650 A at 4.5 kG. A transverse field from a large permanent magnet deflected the beam to the tube wall after the end-of the cavity section. (In some experiments, a linear, permanent magnet wiggler, with a period of

Hewlett-Packard Corp., McMinville, OR.

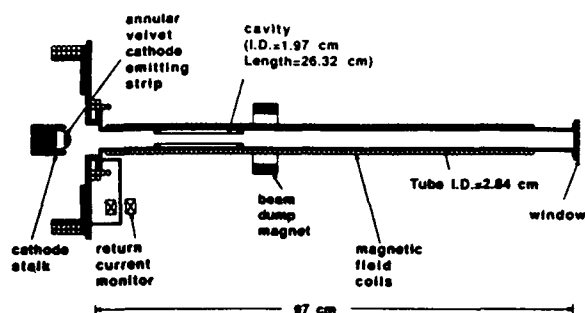


Fig. 2. Experimental configuration.

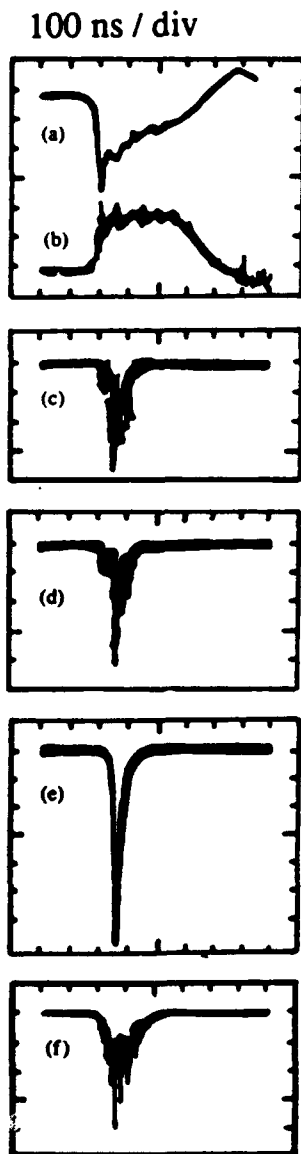


Fig. 3. Experimental data. (a) e -beam voltage 160 kV/div. (b) cathode current 0.6 kA/div. (c) Microwave signal from 10.0 GHz filter. (d) K -band microwave signal ($f > 14.3$ GHz). (e) Microwave signal from 15.0-GHz filter. Data in (a) through (e) taken at 4.34 kG. (f) K -band microwave signal taken at 4.52 kG.

4.4 cm, was utilized; those results will be reported elsewhere.) Microwave output was directed through a TE_{11} circular waveguide to a TE_{10} rectangular waveguide transducer and directional coupler, terminated in a matched load. The microwave output from the maser

was diagnosed by a series of directional couplers and cutoff filters in the X -band (6.6–14.1 GHz) and K -band (14.3–21.1 GHz). The frequency spectrum of the emitted radiation was measured by an array of narrowband (± 0.1 GHz at -10 dB) cavity filters at the following frequencies: 10.0, 11.0, 11.5, 12.0, 13.0, 13.5, 14.0, 14.5, 15.0, 15.225, 15.5, 15.725, 16.0, 16.725, 17.0, 18.5, and 19.4 GHz. Microwave power levels were determined from calibrated directional couplers, attenuators, and diode detectors.

Experimental data are presented in Fig. 3(a) through (e) at a magnetic field of 4.34 kG. High-power microwave emission was measured at 4.34 kG in frequency filters at both 15.0 and 10.0 GHz; no microwave emission was measured on detectors at 12.0 and 17.0 GHz. It should be noted that these measured frequencies agree quite well with those predicted by the upper (15 GHz) CARM intersection and the lower (10 GHz) gyrotron intersection of the uncoupled dispersion relations shown in Fig. 1. The K -band microwave pulselengths in these experiments ranged up to a maximum of $0.2 \mu s$ (Fig. 3(f) at 4.52 kG), which is a factor of five greater than previous CARM results. Oscillation from the high-frequency interaction was maintained over e -beam voltage fluctuations of up to 40 percent in multiple axial modes.

By varying the magnetic field, it was possible to discretely tune axial cavity mode frequencies of both the high-frequency CARM (15–16.7 GHz) and low-frequency gyrotron emissions (10–14 GHz). Frequency data is summarized in Fig. 4, with theoretical plots of the upper and lower intersections of the uncoupled dispersion relations. Note that we attribute only the high-frequency radiation to CARM in the regime where v_p approaches c ; between 15–16.7 GHz, v_p ranges from 1.24 to 1.18 c . The phase velocities were calculated from the known cavity dispersion relation at a given frequency. The phase velocity for the 10-GHz gyrotron mode is about 2.2 c . It should also be noted that the high-frequency CARM and the low-frequency gyrotron modes coalesce at about 14 GHz, corresponding to the grazing intersection of the dispersion relations. At a fixed magnetic field, the CARM gain-bandwidth was comparable to the axial mode spacings; thus, the CARM microwave emission peaked at one or two axial cavity modes ($q = 20$ –24). Low-frequency gyrotron modes were observed simultaneously. At the peak of the CARM interaction (near 4.5 kG), the CARM power was nearly a factor of ten higher than the gyrotron power. Details of the microwave emission from high-order CARM axial modes will be presented in a future paper. The comparison of the data to theory in Fig. 4 suggests that $\alpha = v_{\perp}/v_{\parallel}$ is increasing with the magnetic field, a result which is consistent with other experiments. Fig. 1 shows that the fundamental cyclotron wave interaction is cut off for all but the TE_{11n} cavity modes. In the CARM regime (4.2–4.7 kG), interaction of the second cyclotron harmonic with the TE_{21} modes has been excluded because: (a) A TE_{11} mode transducer was utilized, (b) the TE_{21} growth rate is lower, (c) the high-frequency power exceeded the low-frequency power, and (d) the gyrotron frequency scaling is different than the CARM.

Experimental scaling of the microwave emission power with the solenoidal magnetic field is presented in Fig. 5. In the absence of the wiggler, peak microwave power levels were generated at up to 10 MW for the K -band frequency range and about 1 MW for the X -band frequency range. Since the CARM extracts wave energy from both the parallel and perpendicular components of e -beam velocity, an e -beam with a low $\alpha = v_{\perp}/v_{\parallel}$ can exhibit higher CARM power than gyrotron power. The CARM regime of operation corresponds to the microwave emission power in the K -band which peaks between 4.2 and 4.7 kG. The decrease of the CARM K -band microwave power at high magnetic fields and frequencies may be due to the effects of e -beam velocity spread at large values of the wavenumber and high α . Data indicates that pulses with the highest K -band power had reduced levels of X -band emission, suggesting mode competition between the CARM and the low-frequency gyrotron. (The wiggler increased the X -band power to about 2 MW, but increased the K -band power only slightly.)

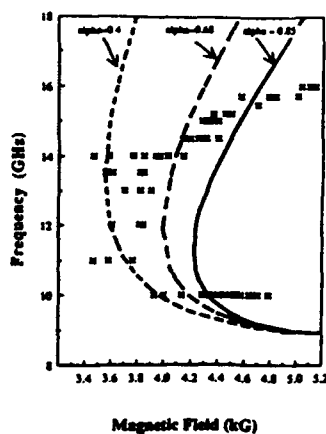


Fig. 4. Summary of measured microwave emission frequencies (X). Lines show theoretical intersections of the uncoupled dispersion relations for three different values of $\alpha = v_{\perp}/v_{\parallel}$.

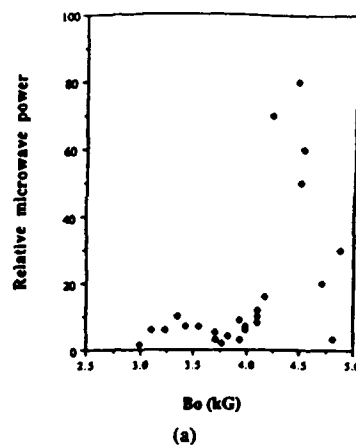
Theoretical calculations of the threshold current predicted for absolute instability [10], [11] yield values of about 60 A for our experimental parameters of Figs. 1 and 3(a)–(c). Even though our experimental current is a factor of 6 to 10 times higher than this predicted threshold current, we do not observe high-power radiation close to the cutoff frequency (~ 9 GHz) as expected for absolute instability. Furthermore, the reasonable electronic efficiency (2–4 percent) in these experiments indicates that absolute instability may not be as serious a problem in CARM oscillators as in amplifiers for the following reasons [10]:

- 1) In the oscillator, the cavity is usually too short to accommodate the long-wavelength mode at the onset of absolute instability.
- 2) In the amplifier, the growth of absolute instability would more easily overwhelm the convective growth of the externally injected signal. These properties apparently agree with previous experience on gyrotron oscillators [2].

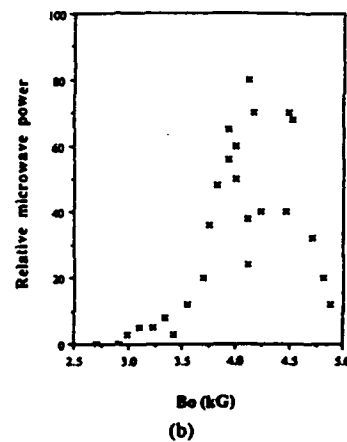
The electronic efficiency of this CARM oscillator was in the range of 2–4 percent (neglecting cavity losses), similar to recent CARM amplifier [8] and oscillator [6], [7] experiments. The present experiments suggest that it may be possible to increase the CARM oscillator efficiency by suppressing the low-frequency gyrotron interaction. Cyclotron maser experiments at higher power and longer pulse length are now underway on the Michigan Electron Long Beam Accelerator (MELBA), at the peak electron-beam parameters of $V = -0.7$ to -1 MV, $I = 1$ –15 kA, and pulse length = 1–2 μ s.

REFERENCES

- [1] T. C. Marshall, *Free Electron Lasers*. New York: Macmillan, 1985.
- [2] C. W. Roberson and P. Sprangle, *Phys. Fluids B*, vol. 1, no. 3, 1989.
- [3] R. M. Gilgenbach *et al.*, *Phys. Rev. Lett.*, vol. 44, p. 647, 1980.
- [4] R. M. Gilgenbach *et al.*, *Nucl. Fusion*, vol. 21, p. 319, 1981.
- [5] L. Barnett, Y. Y. Lau, K. R. Chu, and V. L. Granatstein, *IEEE Trans. Electron Devices*, vol. ED-28, p. 872, 1981.
- [6] S. Gold *et al.*, *Phys. Fluids*, vol. 30, p. 2226, 1987.
- [7] V. L. Bratman, N. S. Ginsburg, G. S. Nusinovich, M. I. Petelin, and P. S. Strelkov, *Int. J. Electron.*, vol. 51, p. 541, 1981.
- [8] I. E. Botvinnik *et al.*, *Sov. Phys.—Tech. Phys. Lett.*, vol. 8, p. 596, 1982. (*Pis'ma Zh. Tekh. Fiz.*, vol. 8, p. 1386, 1982.)
- [9] I. E. Botvinnik *et al.*, *JETP Lett.*, vol. 35, p. 516, 1982. (*Pis'ma Zh. Eksp. Teor. Fiz.*, vol. 35, p. 418, 1982.)
- [10] G. Bekefi, A. DiRienzo, C. Leibovitch, and B. G. Danly, *Appl. Phys. Lett.*, vol. 54, p. 1302, 1989.
- [11] R. M. Gilgenbach *et al.*, in *Proc. 13th Int. Conf. IR and MM Waves* (Honolulu, HI), Dec. 5–9, 1988, SPIE vol. 1039, p. 362.
- [12] Y. Y. Lau, K. R. Chu, L. R. Barnett, and V. L. Granatstein, *Int. J. Infrared Millimeter Waves*, vol. 2, p. 373, 1981.
- [13] J. A. Davies, *Phys. Fluids B*, vol. 1, p. 663, 1989.



(a)



(b)

Fig. 5. Microwave output power detected as a function of the cavity magnetic field. (a) K-band (14.3–21.1 GHz), peak power corresponds to about 10 MW. (b) X-band (6.6–14.1 GHz), peak power corresponds to about 1 MW.